Washington University in St. Louis
Washington University Open Scholarship

Engineering and Applied Science Theses & Dissertations | McKelvey School of Engineering

Winter 12-15-2016

High-throughput Exploration of Glass Formation via Laser Deposition and the Study of Heterogeneous Microstructure in a Bulk Metallic Glass Alloy

Peter Te-Chuan Tsai
Washington University in St. Louis

Follow this and additional works at: https://openscholarship.wustl.edu/eng_etds

 Part of the Engineering Commons

Recommended Citation

Tsai, Peter Te-Chuan, "High-throughput Exploration of Glass Formation via Laser Deposition and the Study of Heterogeneous Microstructure in a Bulk Metallic Glass Alloy" (2016). *Engineering and Applied Science Theses & Dissertations*. 211.
https://openscholarship.wustl.edu/eng_etds/211

This Dissertation is brought to you for free and open access by the McKelvey School of Engineering at Washington University Open Scholarship. It has been accepted for inclusion in Engineering and Applied Science Theses & Dissertations by an authorized administrator of Washington University Open Scholarship. For more information, please contact digital@wumail.wustl.edu.

WASHINGTON UNIVERSITY IN ST. LOUIS

Institute of Materials Science & Engineering

Dissertation Examination Committee:
Katharine M. Flores, Chair
Parag Banerjee
Kenneth F. Kelton
Shankar M.L. Sastry
Srikanth Singamaneni

High-throughput Exploration of Glass Formation via Laser Deposition and the Study of Heterogeneous Microstructure in a Bulk Metallic Glass Alloy

by

Peter T. Tsai

A dissertation presented to
The Graduate School
of Washington University in
partial fulfillment of the
requirements for the degree
of Doctor of Philosophy

December 2016

St. Louis, Missouri

© 2016, Peter T. Tsai

Table of Contents

List of Figures

List of Tables

Acknowledgements

First and foremost, I am thankful to my Lord and personal Savior, Jesus Christ, who resides permanently in my heart as my lifelong companion, counselor, and source of every blessing I hold dear in this life. During the most challenging hours of my years spent in graduate school, when things did not go as they should despite my greatest efforts, His inward presence has been a constant source of strength and endurance.

I thank my advisor, Prof. Katharine Flores, for constantly working hard behind the scenes to secure funding support for my research, and also for giving me the freedom to pursue ideas that interest me. Thank you for persuading me to persevere to the finish line even when I seriously considered quitting. My formal education has been an unexpectedly long, and at times arduous journey, but in retrospect, I am infinitely glad that I did not choose to leave the degree program prematurely. Thank you also for encouraging me to frequently attend and give oral presentations at national conferences. The knowledge, connections, and presentation skills I have acquired during these times will surely help to advance my career in the years to come.

My past and current coworkers in the lab, including: Kelly Kranjc, who has been a faithful friend throughout all six and a half years in graduate school, and who taught me nearly everything I presently understand about instrumented nanoindentation and dynamic modulus mapping. Juan Wang, Mu Li, Zach Rousse, David Robinson. Although research is a "serious" matter, the many casual conversations we had in the office reminded me that matters apart from work, such as family, health, and recreation are also important aspects of human life that should never be ignored.

My instructor, adviser, and mentor at UC Berkeley, Prof. Andreas M. Glaeser. At a university where instruction in the classroom is often neglected in favor of research, your devotion

to teaching was truly refreshing and appreciated. As an instructor, you assigned far too many problem sets, but the resulting foundation of knowledge I gained in your materials thermodynamics and phase transformations courses have proven valuable throughout my tenure in graduate school.

My parents, Larry and Janny. Truly, without your love, prayers, and support throughout my life until now, I would not be where I am today. Thank you for always emphasizing the importance of education and working hard. You two were never given the opportunity to receive the quality of education and training that I have benefited from, and words cannot express my depth of gratitude for the sacrifices you made so that we, the children, could have a chance of attaining to greater success. I sincerely hope that you are as proud of me as I am of you.

Last but not least, my dear wife Jessica. I could not ask for a better companion. Thank you for always listening and being so understanding. You are the primary reason I look forward to returning home at the end of every workday.

Peter T. Tsai

Washington University in St. Louis

December 2016

Abstract of the Dissertation

High-throughput Exploration of Glass Formation via Laser Deposition and the Study of Heterogeneous Microstructure in a Bulk Metallic Glass Alloy

by

Peter T. Tsai

Doctor of Philosophy in Materials Science and Engineering

Washington University in St. Louis, December 2016

Professor Katharine M. Flores, Chairperson

Bulk metallic glasses are a relatively novel class of engineering alloys characterized by a "disordered" atomic structure devoid of long-range translational symmetry. Compared to crystalline alloys, the confluence of metallic bonding and amorphous structure imbues bulk metallic glasses with a unique set of properties that makes them particularly attractive for a wide variety of structural applications. Such properties include exceptional yield strengths, high elastic resilience, resistance to corrosion, and in particular, the unparalleled ability among metals to be thermoplastically formed across a wide range of length scales when heated above the glass transition temperature. Formation of metallic glass from a molten liquid depends on whether cooling is sufficiently rapid to bypass crystallization and vitrify into an amorphous solid; for a given alloy composition, the ease with which full vitrification can occur upon cooling from the liquid state is termed the alloy's "glass forming ability". Unfortunately, relatively few excellent glass formers have been reported in the vast, multicomponent composition space in which they reside. The apparent slowness of progress may be attributed largely to the inefficiency of the one-at-a-time experimental approach to discovery and design. In this thesis work, a high-

throughput combinatorial methodology was developed to expedite the discovery process of new bulk metallic glasses. Laser deposition was used to fabricate continuously-graded composition libraries of Cu-Zr and Cu-Zr-Ti alloys. By processing the libraries with a range of laser heat input, the best glass formers in each alloy system could be efficiently and systematically deduced. Furthermore, instrumented nanoindentation performed on the libraries enabled rapid evaluation of mechanical property trends.

Despite boasting high strengths, monolithic bulk metallic glasses generally suffer from an intrinsic lack of damage tolerance compared to other high performance alloys. Recent studies indicate that the macroscopic deformation behavior of the material may be controlled by structural heterogeneities, although the exact nature and origin of the heterogeneities remain ambiguous. To further the present knowledge, the heterogeneous microstructure of a zirconium-based bulk metallic glass was investigated with instrumented nanoindentation and dynamic modulus mapping. Significant spatial variations in the mechanical properties measured by both techniques suggests a hierarchical arrangement of structural/mechanical heterogeneities in bulk metallic glasses. Moreover, a previously unobserved elastic microstructure, comprising an interconnected network of elastic features, was revealed by dynamic modulus mapping. Despite the absence of visible contrast when imaged with electron microscopy, the aligned morphology of the elastic features and their sensitivity to thermal processing conditions imply the occurrence of spinodal decomposition in the supercooled liquid prior to glass formation. Finally, based on analysis of load-displacement data from nanoindentation experiments performed throughout the thesis work, a new parameter, the plastic work ratio, was proposed as a figure of merit for quantifying the intrinsic plasticity of monolithic metallic glass alloys.

Chapter 1

Introduction

1.1 Bulk Metallic Glasses

On a fundamental level, a liquid becomes a glass when it is quenched sufficiently rapidly from its molten state to bypass crystallization and solidify into a rigid, metastable structure devoid of long-range atomic periodicity. While glass formation is commonplace among synthetic polymers and oxide glasses, the lack of bond directionality in metallic alloys places little constraint on the orientation of the atoms, causing difficulty avoiding crystallization. For example, extreme cooling rates on the order of 10^5 – 10^6 K/s are required to synthesize Au-Si metallic glass (MG) alloys, the first reported vitreous alloys produced from the liquid state[1].

Beginning from 1989, a series of multicomponent (3 or more constituent elements) bulk metallic glasses (BMGs) with critical (minimum required) cooling rates on the order of 1 – 100 K/s were discovered, triggering a global interest in MGs as viable engineering materials[2–4]. Prior to the discovery of BMGs, metallic glasses were mainly a laboratory curiosity, with thickness dimensions limited by the extremely high quench rates required to avoid crystal nucleation in the undercooled liquid and retain amorphous structure. To date, the best reported glass-forming alloy is $Pd_{40}Cu_{30}Ni_{10}P_{20}$, which boasts an amorphous casting diameter of 72 mm [4].

The combination of metallic bonding and amorphous structure imbues BMGs with a unique set of attractive properties that is unattainable in even the most advanced crystalline alloys. Notable properties include exceptionally high strength (> 1 GPa), high elastic strain limits (~2 %), and the unparalleled ability among metallic materials to be thermoplastically processed over many orders of magnitude in length[5,6].

1.2 Glass Forming Ability

Glass forming ability (GFA) is a measure of the ease with which a molten alloy vitrifies into an amorphous solid upon cooling. Below the liquidus temperature, the liquid is no longer energetically the most stable phase and will experience a thermodynamic driving force for crystallization, which increases with deeper undercooling. But the rate of crystallization is controlled not only by the thermodynamic driving force but also the kinetic ability of the atomic species to rearrange into periodic configurations, which diminishes with decreasing temperature. It follows that an alloy's GFA depends strongly on the interplay between the thermodynamic and kinetic characteristics of the undercooled liquid. The competing influence of the two factors produces the so-called "C-shaped" time-temperature-transformation (TTT) curve[6,7] (Fig. 1.1), constructed from plotting the time it takes for the onset of crystallization to occur as a function of temperature. To illustrate, the two straight lines in the schematic TTT diagram of Figure 1.1 represent critical cooling paths for two hypothetical alloys, where the value of the slopes are corresponding critical, or minimum, cooling rates (r_c) for avoiding crystallization events. It can be clearly seen that one alloy has the nose of its transformation curve shifted to a longer time, resulting in a lower r_c, and equivalently, better GFA.

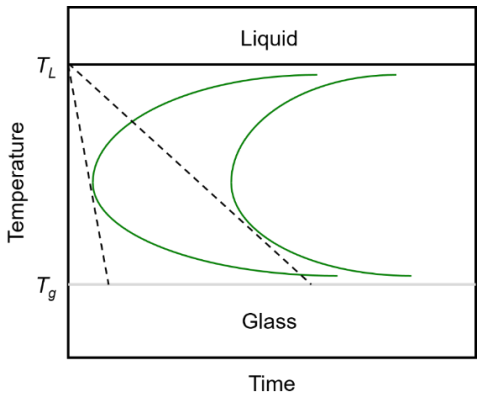

Figure 1.1 Schematic TTT diagram containing transformation curves for two hypothetical alloys. The curve shifted to the right corresponds to the superior glass former.

1.3 Predicting Glass Forming Ability

Despite steady reports of newly discovered BMGs over the past two decades, relatively few BMGs with centimeter-scale casting dimensions have been identified within the vast composition space occupied by multicomponent alloys. This limited progress largely reflects the lack of reliable criteria for predicting the GFA of arbitrary multicomponent alloys. For example, in the relatively brief history of BMGs, arguably the two most prevalent indicators of GFA are the reduced glass transition temperature T_{rg}, defined as the ratio of the glass transition temperature (T_g) to the liquidus temperature (T_L), and ΔT_x, the difference between the crystallization onset temperature (T_x) and T_g[8–10]. In his seminal work published in 1969, Turnbull reasoned that a sufficiently high T_{rg} could kinetically stabilize an undercooled liquid against crystallization during cooling[8]. However, although large T_{rg} has been shown to correlate with high GFA in many alloy systems, its reliability as an indicator of GFA is not universal[11] and neither is it truly predictive of glass formation *a priori*, since experimental pre-knowledge of T_g is required. ΔT_x is a measure of the thermal stability of the glass upon heating. While it is expected that the best glass formers are also the most thermally-stable glasses, ΔT_x does not address the stability of the undercooled liquid between T_x and T_L. It is also measured by heating, whereas ease of vitrification is determined strictly from cooling. Hence, like T_{rg}, ΔT_x is not an absolute figure of merit for GFA, although a weak, general correlation does exist[12,13]. Similar shortcomings apply for all other temperature-based predictive parameters that have been proposed[10,12–15].

Besides temperature-based figures of merit, empirical rules have been developed to guide the discovery of new bulk glass-forming alloys. According to the widely accepted rules proposed by Inoue, the best metallic glass formers should be multicomponent, exhibit a large, negative enthalpy of mixing between the elemental pairs, and feature atomic species with at least a 12 %

mismatch in their respective atomic radii[16]. While valuable in narrowing the search field for new BMGs, these rules do not contain adequate quantitative specificity to actually predict GFA. It is therefore more fitting to consider the above criteria as general guidelines for alloy development rather than predictive rules, as alloys that fit the criteria are not guaranteed to possess the expected GFA. The reverse holds true as well; certain alloys violate the empirical guidelines but are exceptionally good glass formers. A notable example is the aforementioned $Pd_{40}Ni_{10}Cu_{30}P_{20}$ alloy, with critical casting thickness exceeding 7 cm. The heat of mixing for both Pd-Cu and Pd-Ni is nearly zero and the difference in size among the atomic species is less than 10%[17].

1.4 Metallic Glass Structure and the Structural Origin(s) of GFA

Since the discovery of BMGs, a major challenge has been to describe the details of atomic structure of metallic glasses and the structural origin of glass forming ability[18]. Relative to their crystalline counterparts, metallic glasses can be considered "disordered" materials, but short to medium range ordering (SRO and MRO) still persists[18–20]. Experimentally measured densities of MGs have been shown to generally be very close to their devitrified (crystallized) state, indicating a topological short-range clustering of the atomic species that is more efficient than can be accomplished by dense random packing[21]. Pair distribution functions derived from diffraction experiments (Fig. 1.2), useful for determining the average nearest neighbor distance between atoms, typically contain a strong first peak that is characteristic of the SRO, followed by additional weaker peaks within a range of 0.5-1.5 nm that have been ascribed to MRO[19,22]. The negative enthalpies of mixing between solvent and solute atoms in metallic glasses also suggest that chemical ordering, resulting from the preferential attraction between solute and solvent atomic species, may coexist with topological ordering[23–26].

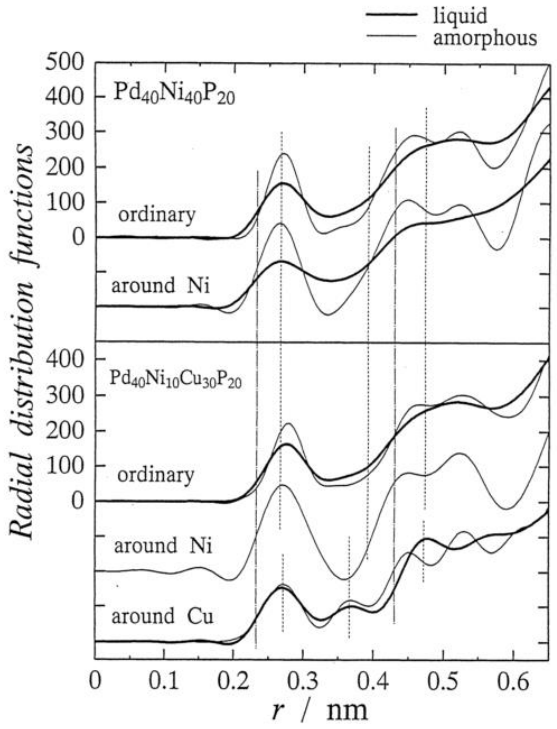

Figure 1.2 Radial distribution functions for two Pd-based BMGs, revealing the SRO and MRO in the glass and liquid states. Image taken from ref. 16.

In crystalline alloys, the long-range translational symmetry arises from periodic tiling of a common structural motif (i.e. the unit cell); the local atomic environment in a crystalline alloy is identical at every lattice position and constitutes the entire structural description of the alloy. In contrast, metallic glasses are populated with a diverse range of SRO motifs in the form of nearest-neighbor atomic clusters that are statistically distributed throughout the volume of the glass in random orientations (Fig. 1.3). Therefore, in terms of short-range structural variety, MGs are arguably more complex than their crystalline counterparts. It follows that while diffraction techniques are often adequate to resolve a crystalline alloy's structural symmetry, diffraction performed on MGs can only provide an average representation of the material's complicated atomic-level structure. Recently, in a breakthrough study, diffraction patterns revealing the symmetry of individual atomic clusters in MGs was achieved by using a highly convergent

electron beam with sub-nanometer beam diameter[20]. Nevertheless, the method was confined to visualize only a single cluster at a time and could not be used to reconstruct the 3-dimensional spatial arrangement of individual clusters.

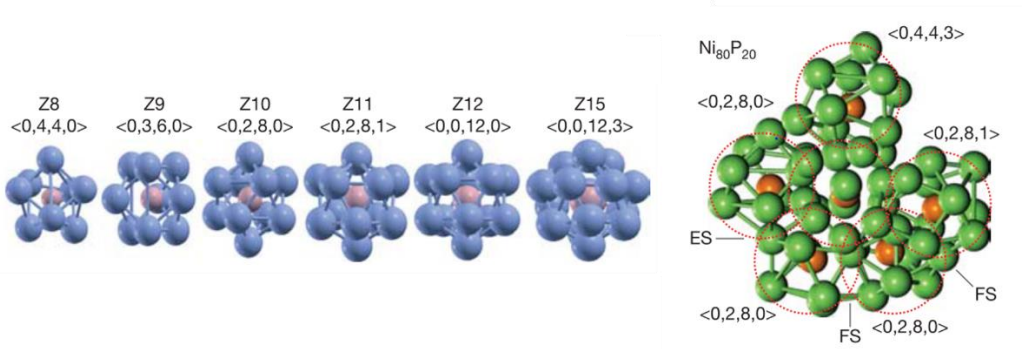

Figure 1.3 Examples of various SRO atomic clusters and their MRO coordination structure in a simulated metallic glass. Images adapted from ref. 19.

Without the ability to experimentally resolve atomic-level structural details, researchers have relied on computational methods such as molecular dynamics (MD) or reverse Monte Carlo simulations to artificially reproduce the atomic structures of MGs[18]. In classical MD, potential energy functions that describe the interatomic forces in an alloy are applied to simultaneously track the atomic positions of the atoms over time via Newton's equations of motion. For accurate results, extremely small time steps on the order of 1-10 femtoseconds are generally required[27]. Model MGs are produced by heating a simulated crystalline precursor (e.g. BCC structure) of the composition of interest to a stable, disordered liquid state, followed by rapidly quenching the liquid to a temperature below T_g.[27,28] Owing to the miniscule time steps and limited computational ability, the quench rates used in creating simulated glass structures are typically several orders of magnitude (10^{10} – 10^{12} K/s) above the upper limit of experimentally accessible cooling rates, producing amorphous structures that are potentially very different from bulk specimens. To

confirm structural accuracy, pair distribution functions or structure factors calculated from simulated MGs (SMGs) are often compared with experimental diffraction results.

Because metallic glass is a metastable material that could occupy many possible configurational potential energy states, the structure of two glass specimens of the same composition could never be identical in terms of the exact positions of the atoms. SMGs are therefore characterized in terms of the statistical makeup of short-range topological features such as nearest-neighbor coordination number, bond angles, common-neighbor indices, etc. that may be unique to a particular alloy composition and thermal processing history[18]. The Voronoi tessellation algorithm is a particularly useful analysis tool for describing the topological nature of SRO in SMGs by representing each atomic cluster in the glass with an associated polyhedron[18,29,30]. The clusters are visualized as interpenetrating; every atom is a central atom within a cluster, surrounded by a shell of nearest-neighbor atoms. Using planes to bisect the lines connecting an atom to its nearest neighbors results in polyhedral cells that reflect the symmetry of individual clusters (Fig. 1.4).

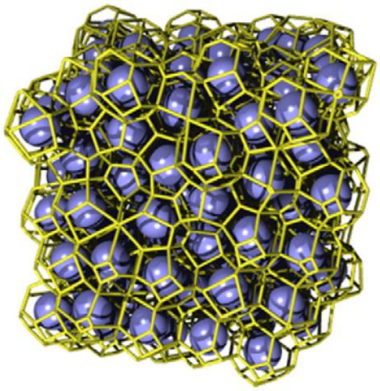

Figure 1.4 Voronoi cells, reflecting the symmetry of individual clusters contained within a model glass. Image taken from ref. 18.

The clusters are labeled by their Voronoi index $<i_3,i_4,i_5,i_6>$, where the subscripts refer to the number of triangles, quadrangles, pentagons, and hexagons that comprise the cell. For example,

an index of <0,0,12,0> describes an icosahedral cluster of a central atom surrounded by 12 nearest neighbors, with each nearest neighbor bond exhibiting five-fold rotational symmetry (Fig. 1.3).

Of the many types of clusters observed in simulated metallic glasses and liquids, efficiently-packed, topologically-stable clusters have been shown to play an important role in the transition across T_g from viscous liquid to rigid glass. The transition in metallic systems is invariably manifested as a non-Arrhenius dynamical slowdown of the liquid near T_g (Fig. 1.5), the severity of which can be quantified by the kinetic fragility of the supercooled liquid $m = \left|\frac{\partial \ln(\eta)}{\partial(T_g/T)}\right|_{T=T_g}$ [31,32], where η denotes viscosity. Strong glasses with low m exhibit a more gradual loss of atomic mobility with decreasing temperature.

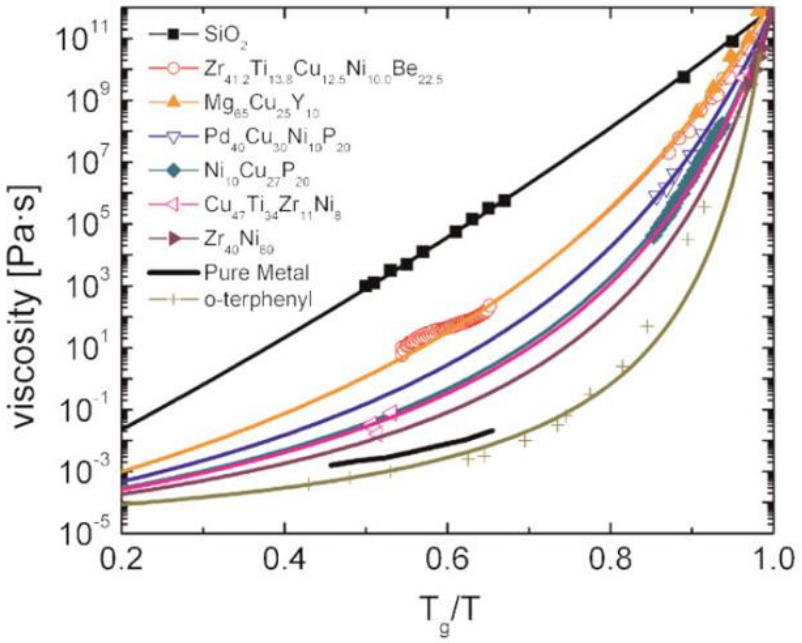

Figure 1.5 Angell plot showing the dynamic slowdown of undercooled liquids for a variety of materials, including several BMGs. Image taken from ref. 6.

With regards to GFA, low fragility is generally favored; fragile alloys are more liquid-like at temperatures above T_g and offer less kinetic resistance against crystallization within the super-cooled liquid region[33,34]. Studies of simulated Cu-Zr alloys have shown that atoms embedded in

efficiently-packed <0,0,12,0> icosahedral clusters represent the slowest species in the alloy, and their population increases rapidly upon cooling through the glass transition, correlating with the steep rise in viscosity[35,36]. Interestingly, icosahedral SRO is also particularly dominant in $Cu_{64}Zr_{36}$,[37] widely recognized as the best glass former in the binary system. Kelton *et al*. measured the temperature-evolution of the structure factor of supercooled liquids in the vicinity of the glass transition and demonstrated that the steep rise in viscosity (dynamic slow-down) is indeed associated with an enhancement of structural ordering in the liquid[38]. The agreement between simulation and experimental results indicates that efficiently-packed clusters are favorable for GFA by imparting kinetic resistance to a cooling liquid against crystallization; the best glass formers should maximize the population of these stable clusters within the liquid as well as the glassy, vitrified state.

Structural modeling affords an alternative approach for investigating the structural origins of GFA. Among the numerous structural models that have been proposed over the years, including notably Bernal's dense randomly-packed hard sphere model[39,40] and Gaskell's stereochemical model[41], it is arguable that Miracle's efficient cluster packing (ECP) model[42–44] has most successfully captured the universal structural characteristics of BMGs, namely SRO, MRO, and overall dense atomic packing without compromising amorphous structure. The basic structural units in the ECP model are efficiently-packed, solute-centered atomic clusters; these clusters are themselves efficiently packed into crystal-like configurations (i.e. FCC, BCC, simple cubic), giving rise to the MRO (Fig. 1.6). Adjacent clusters are face-, edge-, or vertex-sharing in the respective nearest-neighbor coordination shells, and interstitial sites between the clusters are either vacant or filled with topologically appropriate solute species to achieve overall dense packing. Preferred clusters species with the highest packing efficiency are determined by the atomic radius

ratios between the solvent and solute atoms, and there are no orientational constraints among neighboring clusters.

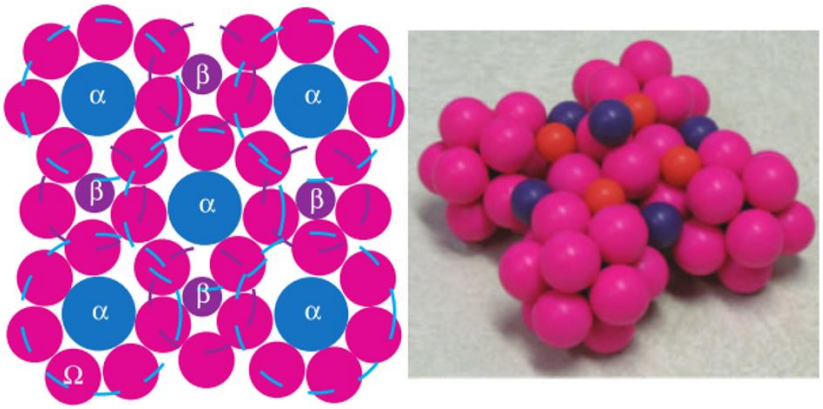

Figure 1.6 2-dimensional schematic and 3-dimensional physical representation of Miracle's efficient cluster packing model. Images taken from ref. 42.

The ECP model has demonstrated success in describing the structure of known glass-forming alloys, but cannot be used to predict GFA of an arbitrary composition *a priori*. Within a given alloy system, multiple compositions may exist that optimizes packing efficiency of the modeled structures, but it is unknown which structures are the superior glass formers. A critical weakness of the ECP model is the absence of chemical influences on GFA. According to the model, two chemically distinct but topologically identical alloy systems would contain equally favorable glass formers at the same compositions. But a survey of known glass-formers clearly reveals that chemical effects on GFA cannot be neglected. For example, Ni and Cu are topologically identical species, having approximately the same atomic radius; however, BMGs do not exist in the Ni-Zr system while the Cu-Zr system contains multiple bulk amorphous compositions[45]. The ECP model also does not provide reasons for why FCC, BCC, or simple cubic arrangements of the clusters are the preferred schemes for MRO. An ab-initio molecular

dynamics study of various binary glasses indicated that icosahedral or string-like network arrangements of solute-centered clusters may be equally valid MRO configurations[19].

In a recent update to the ECP model, Laws *et al.* introduced the additional constraint that the optimum glass-forming compositions within a given alloy system are those where efficient packing is simultaneously achieved in all atoms, not only the solute-centered clusters[44]; that is, each atom in the alloy is a central atom of an efficiently-packed cluster. The authors proposed that compositions deviating from simultaneous efficient packing would result in less-than-optimal GFA. Under the new criteria, compositional regions could be identified as definite non-starters, and comparison with known binary and ternary glasses verified that none of the reported glass-forming compositions resided in these excluded regions, lending compelling support for efficient topological packing as a legitimate universal criterion of GFA. Furthermore, it was demonstrated that for a number of chemically-distinct multicomponent systems, the best reported glass formers within the system nearly always fulfilled conditions required for simultaneous efficient packing. The updated ECP model offers a certain degree of predictive capability that was missing in the original model, but the influence of chemistry on GFA remains unaddressed. It is also unclear how global efficient packing of the glass is correlated with other determining factors of GFA such as the viscosity of the supercooled liquid and its dynamic fragility. Despite their incompleteness, the ECP models still represent immense progress towards reliable predictability of glass formation and provides a useful aid for narrowing the search field for potential bulk glass formers within unexplored alloy systems.

1.5 Experimental Exploration of Metallic Glass Formation – Status Quo

Because reliable prediction of GFA *a priori* is still unrealized, the development of novel BMGs is carried out primarily through experimental trial and error, guided by the aforementioned

predictive models and empirical rules. Experimental strategies for exploring glass formation in metallic systems conventionally involves the synthesis of one alloy at a time within a compositional region suspected to contain candidate glass-formers, followed by the application of various diffraction techniques to confirm amorphous structure in the specimen. If not amorphous, the chemical composition is modified iteratively until a glass-forming alloy is discovered. Once a BMG is identified, wedges with a tapered thickness profile or samples of varying diameters can be cast in order to determine the critical, or maximum attainable, casting thickness of a particular BMG composition, beyond which crystallization becomes unavoidable. Although the critical casting thickness provides an estimate of an alloy's GFA, it is more accurate to quantitatively describe GFA by an alloy's critical cooling rate (r_c), the minimum cooling rate from T_l to T_g that is required for the undercooled liquid to bypass crystallization and completely vitrify. Measurement of r_c however, is difficult in practice and GFA has mostly been reported in terms of critical casting thickness[46,47].

Unfortunately, due to differences in experimental conditions during synthesis, reported critical casting thicknesses in the literature could vary significantly for the same alloy composition[48–52], making it unreliable to rank GFA by comparing values of critical casting thickness reported from different sources, in particular for alloys that possess similar GFA. An accurate comparative assessment of GFA within the composition space of a particular alloy system could only be realized by synthesizing all compositions under identical experimental conditions.

Besides the inherent unreliability of critical casting thickness as an accurate quantifier of GFA, the main limitation of conventional casting methods is the inefficiency of investigating one alloy composition at a time. Owing to the acute sensitivity of GFA to changes in composition[53], a thorough investigation of a multicomponent alloy system would necessitate an impractically

large number of specimens to be carefully cast and characterized, each separated by no more than 1 at. % from neighboring compositions.

1.5.1 Combinatorial synthesis methods

Such fundamental shortcomings of conventional fabrication and GFA evaluation methods has motivated the development of more efficient experimental strategies for exploring glass formation in multicomponent systems. To date, reported efforts aimed towards a combinatorial synthesis approach for studying MG alloys, and engineering alloys in general, have mainly involved vapor deposition techniques such as magnetron co-sputtering[20,48,54–59]. In a notable paper from 2008, Li *et al.* attempted to study GFA by designing a clever method involving the fabrication of thin-film amorphous Cu-Zr microcantilevers[48]. A row of silicon nitride microcantilevers were synthesized by photolithography and chemical etching. Cu and Zr were then co-sputtered onto the row of cantilevers. The targets were positioned relative to the wafer in a way such that the resulting amorphous cantilevers varied in composition from Cu-rich on one end of the array to Zr-rich on the opposite end. The entire assembly was then annealed to fully devitrify the Cu-Zr thin films. Resulting upward deflection of each cantilever upon devitrification was attributed to an increase in density, and the magnitude of the increase was computed by observing the amount of deflection. When the density change was plotted versus composition, the peaks corresponding to the minima found near exact agreement with the critical thicknesses obtained from casting a series of wedges with discrete compositions. The authors suggested that the apparent relationship between the relative density of the glass and GFA could facilitate the discovery of new BMGs.

While the combinatorial methodology of the study was creative and the results contributed towards a deeper understanding with respect to the structural origins of glass forming ability, the reported correlation between relative density and GFA has not been verified to be true in other

alloy systems. Furthermore, $Cu_{46}Zr_{54}$, reported to be an excellent glass former in the binary system[52], was not identified in the study.

Ding *et al.* reported using magnetron sputtering to fabricate Au-Cu-Si composition libraries containing hundreds of discrete compositions[57]. By heating the entire library to a molten state and then cooling at a controlled rate, the authors used a digital camera to track nucleation and growth of the primary crystalline phase(s) within each composition by detecting a distinct change in surface contrast of the film upon crystallization (Fig. 1.7). Their method allowed high-throughput measurement of the nucleation temperature (T_n) of all 800 compositions and based on the findings, T_g/T_n was suggested as a new indicator of GFA. The ability to rapidly evaluate T_n of an entire composition library is a promising contribution towards the development of combinatorial techniques for metallic glass design, but T_g/T_n, like T_{rg}, still relies on knowledge of characteristic temperatures. It is noteworthy that the glass transition could not be determined in a high-throughput manner for each composition in the library; constant T_g across the ternary composition space was assumed, which would not necessarily apply for an arbitrary alloy system. The new predictive parameter also has not been demonstrated as a reliable indicator of GFA in other alloy systems.

In a follow-up paper, Ding *et al.* adapted a blow molding technique to a co-sputtered Mg-Cu-Y thin film library for identifying compositions with the highest thermoplastic formability

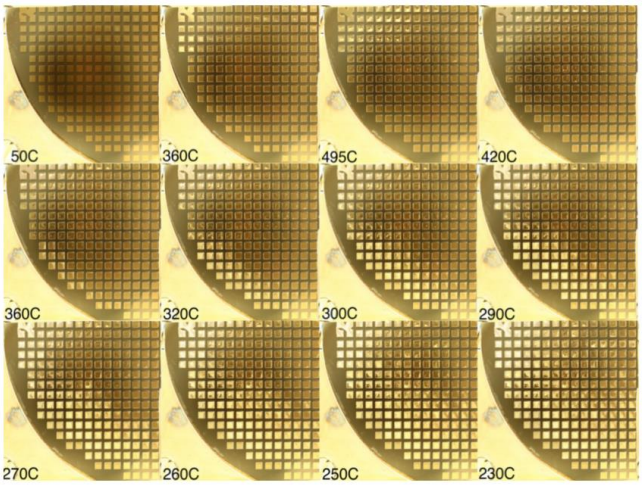

Figure 1.7 Thin film composition library of Au-Cu-Si alloys synthesized by magnetron co-sputtering, reported in ref. 58. By melting the entire library and cooling at a controlled rate, the authors of the study were able to measure nucleation temperatures in a high-throughput manner.

(TPF)[58]. Among metallic engineering materials, MG alloys possess the unique ability to be formed and molded into complex geometries when heated above T_g in the supercooled liquid region[6]. Although TPF is irrelevant with respect to the load-bearing properties of BMG alloys, from a processing and manufacturing standpoint, thermoplastic formability is a major technological advantage of BMGs over conventional crystalline alloys. The authors' work successfully demonstrated that the composition libraries fabricated via a combinatorial approach could serve as a template for the high-throughput assessment of important composition-dependent properties.

Admittedly powerful in their capability to fabricate continuously-graded composition libraries, a major limitation of vapor deposition techniques is the exceptionally high quench rates the atoms undergo, resulting in glass formation over a wide composition range and precluding the direct comparison of a composition from another neighboring composition with respect to GFA. For example, Li *et al.*'s thin film Cu-Zr microcantilevers were each fully amorphous in their as-fabricated state, even though the critical casting thickness varied significantly within the range of compositions that were explored[48]. It is also arguable that the atomic structure of vapor-deposited

MGs may be significantly different from liquid-quenched glasses[59,60]. As a result, composition-property trends obtained from characterizing vapor-deposited MG libraries may not accurately reflect the compositional dependence of properties obtained from testing bulk specimens.

1.5.2 Laser deposition as a combinatorial BMG design tool

Laser additive manufacturing, or laser deposition (LD), is a solid freeform fabrication technology for manufacturing 3-dimensional metallic parts via an additive building process[61]. The basic principle of the process directly resembles that of 3d printing, albeit using metallic feedstock rather than polymers as the "printing" medium. In LD, a CAD file of the part is first converted into a series of parallel two-dimensional slices. The slices are then deposited consecutively in a layer-by-layer fashion to build the part. Deposition involves the simultaneous operation of three machine components: a powder delivery system, a moving stage upon which the work piece is fixed, and a laser beam as the consolidating tool. During the deposition of a single layer, the laser beam is focused onto the work piece to create a localized melt pool, metal feedstock powder is incorporated directly into the molten pool, and the stage follows a tool path to raster the laser across the substrate according to the geometry of the layer. After the layer is complete, the process is repeated for subsequent layers of the build. In this way, near net-shape parts with complex geometries can be fabricated.

Owing to the high local cooling rates (10^3 – 10^4 K/s) that could be achieved in the melt pool during laser processing[62], a number of studies have investigated the application of laser technologies for fabricating freeform BMG parts[63–65]. Yang *et al.* used laser solid forming, a process similar to LD, to deposit up to seven layers of a pre-alloyed Zr-based BMG powder onto an amorphous substrate[63]. Zheng *et al*. reported using LD to fabricate Fe-based BMG shells, solid cubes, and multi-layered coatings[64]. Pauly and co-workers reported fabricating complex three-

dimensional scaffolds with a Fe-based BMG feedstock powder[65]. Despite the cooling rates being significantly higher than in casting conditions, the attempts from all three groups were unsuccessful in fabricating fully amorphous freeform parts, suggesting that the repeated rapid heating and cooling cycles inherent in the LD manufacturing process could be responsible for the nucleation and growth of undesirable crystalline phases. Until now, the fabrication of dense, monolithic BMG parts by LD remains unfulfilled.

While unresolved challenges preclude additive manufacturing of fully amorphous freeform BMG specimens, laser surface treatments and single layer deposits have been successfully demonstrated as viable options for fabricating amorphous BMG coatings for anti-wear applications. Chen *et al*. conducted laser surface treatments with crystalline substrates of various BMG compositions and empirically determined the appropriate processing parameters for achieving fully amorphous coatings[66]. In LD experiments with a pre-alloyed Zr-based BMG powder on both crystalline and amorphous substrates of the same composition, Sun and Flores reported amorphous single-layer deposits nearly void of detectable crystalline features[67].

LD could also be used to fabricate compositionally graded specimens by gradually varying the relative powder delivery rates of chemically distinct powders during the deposition process. Several groups have reported building compositionally graded specimens with LD[68–74]. Hofmann and co-workers recently reported the deposition of 304L-Invar 36 rods graded in the radial direction[73]. Instrumented nanoindentation of the rods showed graded elastic modulus and hardness that accompanied the graded composition profile. Collins *et al*. fabricated 25 mm long cylinders of Ti-V and Ti-Mo alloys featuring pure titanium on one end with vanadium or molybdenum content increasing along the long axis of the cylinder[69]. They further investigated the trend of microhardness with varying composition, demonstrating the capabilities of LD as a combinatorial

alloy design tool. A follow-up paper detailed the fabrication of compositionally graded beta titanium specimens for designing biocompatible orthopedic implants[74].

The ability to create amorphous single layers of MG alloy on both crystalline and vitreous substrates, combined with the option to vary chemical composition "on the fly", renders LD as a promising high-throughput tool alongside vapor deposition methods for developing novel BMGs with desirable properties. In comparison to vapor deposition techniques, LD also has the added advantage that glass formation transpires through quenching from the liquid state to produce atomic structures more representative of bulk cast specimens.

1.6 Mechanical deformation behavior of BMGs

Next to glass forming ability, perhaps no other subject matter has captured the attention of the metallic glass community more than the mechanical behavior and performance of BMGs. The combination of high strength, high elastic resilience, low energy loss coefficient, large elastic strain limits, and high hardness forms a unique suite of attractive properties suitable for a wide variety of potential applications. An early application incorporated a Zr-based BMG onto the striking surface of golf clubs, taking advantage of the material's spring-like resilience to achieve longer driving distances[75]. Unfortunately, the application was premature, as the fatigue and fracture properties of the BMG were poorly understood at the time, resulting in shattering of the clubs after repeated use. Other examples of structural applications include casing material for electronic devices, high-precision parts for luxury timepieces, and high-end knives.

While a number of external factors, including the high cost of elemental feedstock, have hindered more widespread use of BMGs in structural applications, the main limitation of most current BMG alloys is their intrinsic lack of tensile ductility and low damage tolerance compared to high-performance steel, aluminum, and titanium alloys. Without dislocation defects to facilitate

homogeneous plastic flow in metallic glasses, plastic deformation upon yielding is decidedly inhomogeneous, with the plastic strain concentrated into thin planar regions of deformed material called shear bands that are approximately aligned to the plane of maximum shear stress. Under uniaxial tensile loading conditions, irreversible plastic flow is typically carried by a dominant shear band that propagates towards catastrophic brittle failure, resulting in virtually zero observable plasticity in the global stress-strain response. On the other hand, limited macroscopic plasticity is attainable in uniaxial compression or bending tests due to the compressive stresses constraining the unstable propagation of a dominant shear band and allowing the opportunity for multiple shear bands to distribute plastic strain more homogeneously throughout the material.

1.6.1 Structural origins of deformation behavior

Similar to the study of glass forming ability, intense research efforts have been devoted to understanding the structural origins of deformation behavior in metallic glasses. The exact nature of the atomic-level deformation remains unsolved, but it is generally agreed that plastic deformation is initiated by local groups of atoms acting as flow defects in response to an applied shear stress. Spaepen and Argon introduced the first quantitative models to describe plastic flow behavior in metallic glasses as mediated by local flow defects[76,77]. Published nearly four decades ago, many physical concepts from the models continue to be relevant in up-to-date discussions of plastic deformation behavior.

Spaepen envisioned the fundamental unit of irreversible plastic flow as a diffusive jump of an atom into neighboring sites of relatively higher free volume, analogous to vacancy diffusion mechanisms in crystalline materials[76] (Fig. 1.8a). When no stress is applied, forward and reverse jumps are thermally activated and equally likely to occur. Under an applied stress, the jumps become directionally biased, the accumulated effect of which results in net plastic strain. The

mechanistic validity of the diffusive-jump model is debatable, but perhaps the most compelling concept inherent to the model is the assumption that free volume is non-uniformly distributed throughout the glass and that the ability of an alloy to accommodate plastic flow hinges fundamentally on the availability of free volume sites. The importance of free volume to metallic glass plasticity is corroborated by the well-known embrittlement of BMGs when the material is isothermally annealed below T_g.[78,79] Sub-T_g annealing removes free volume through structural relaxation processes, reducing the availability of loosely-packed, fertile regions that are more susceptible to plastic rearrangement, and resulting in embrittlement of the glass.

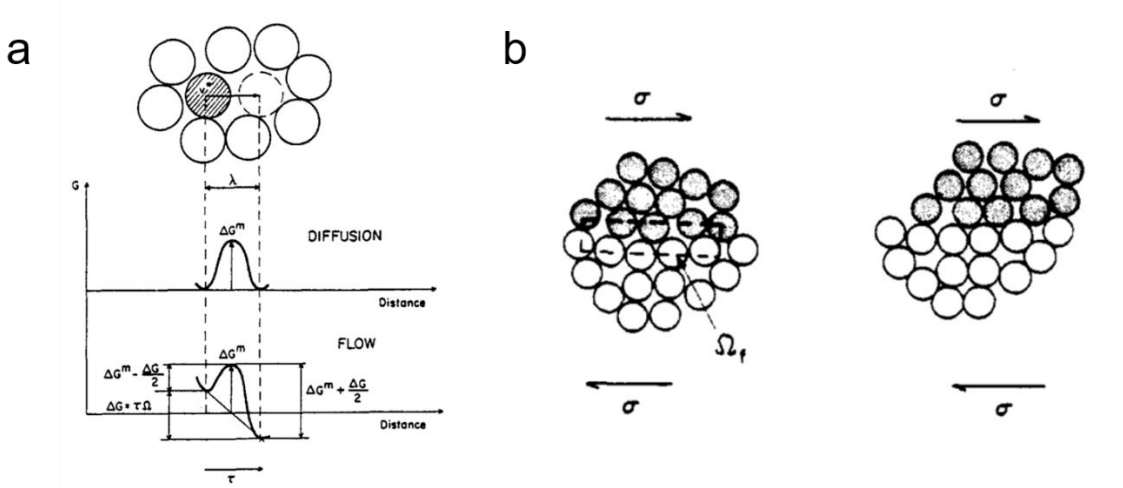

Figure 1.8 Mechanistic models for plastic flow in metallic glasses. **(a)** Spaepen's free volume diffusive jump model. **(b)** Argon's shear transformation model, based on 2-dimensional bubble raft simulations. Images in (a) and (b) taken from refs. 76 and 77, respectively.

Alternatively, in Argon's model, the basic unit of plastic flow are isolated groups of atoms that can reconfigure collectively to accommodate shear strain[77,80]. Argon termed the local plastic deformation events as shear transformations; the associated defect or site of the event is now more commonly referred to as a shear transformation zone (STZ). The mechanistic basis of STZs originated from the seminal shearing experiments performed on a disordered 2-d bubble raft comprising bubbles of different sizes[81]. Upon shearing, equiaxed groups of bubbles approximately

5 bubble diameters across were observed to undergo collective transformation into non-equiaxed (sheared) configurations. Argon argued that an analogous deformation mechanism involving a small group of atoms should occur in metallic glasses (Fig. 1.8b). In Falk and Langer's updated STZ model[82], molecular dynamics shearing experiments were performed on a 2-d Lennard-Jones glass, and once again, localized shear transformations involving a small group of atoms were observed. Johnson and Samwer's cooperative shearing model predicted that the energy barrier for activating the flow defects is minimized for STZs with sizes on the order of 100 atoms[83]. Global yielding transpires when these low-energy STZs become simultaneously unstable. In a follow-up molecular dynamics study of STZ events in a Cu-Ti glass, the authors applied a correlation function to the atomic displacement field at the onset of global yielding and estimated the size of individual STZs to be 15 angstroms in diameter[84], or equivalently consisting of approximately 120 atoms, in excellent agreement with the size predicted by the model.

1.6.2 The role of heterogeneous structure

Recent results from atomistic modeling suggest STZs as pre-existing structural defects, arising from the heterogeneous distribution of SRO motifs. Ma *et al.* demonstrated in simulated Cu-Zr binary glasses strong correlations between local shear modulus, topological stability of atomic clusters, and the tendency for non-affine (plastic) atomic displacements[85–87]. In simulated shearing tests, nanoscale regions populated by topologically-unstable clusters, and hence lower shear modulus, were observed to overlap with sites of largest non-affine displacements (Fig. 1.9a). These findings mirror the longstanding recognition of free volume, or loose atomic packing, as the physical basis for achieving plasticity, but also advances the understanding of flow defects beyond the generalized argument of free volume to consider specific short-range structural motifs that promote plastic behavior.

Ma *et al.*'s computational work highlights the increasing recognition within the metallic glass community that structural heterogeneities contribute a critical role to the deformation behavior of BMGs. As discussed earlier, metallic glass is intrinsically heterogeneous on the atomic level, comprising a broad distribution of topologically and chemically distinct SRO clusters. Beyond the SRO length scale, heterogeneous microstructure is less intuitive, especially considering the structural resemblance of BMGs to their "disordered" liquid state. There is, however, increasing experimental evidence of spatially-coordinated heterogeneities with characteristic feature lengths that extend well past the size of individual atomic clusters. For clarity, the terms "heterogeneous" or "heterogeneity" from here onward will be used mainly to denote these larger spatial fluctuations.

It has long been known that the shear modulus G of BMGs is significantly lower (10 – 30%) than their crystalline counterparts despite having similar densities, while bulk modulus K usually differ by only a few percent[18]. The unexpectedly low G of metallic glasses implies that within the global elastic regime, a substantial fraction of the bonds do not participate in providing resistance to shear strain. Due to the amorphous structure, some regions in the glass may relieve the applied stress by undergoing non-affine (plastic) strains, even though the macroscopic behavior resembles fully elastic deformation. Dmowski *et al.* conducted in situ x-ray diffraction experiments on a Zr-based BMG loaded in tension to a stress below the yield point was non-affine[88], in accord with the comparatively low G values. The existence of liquid-like regions that deform plastically within the global elastic regime provides insight into the spatial arrangement of the elastic heterogeneities. Specifically, the results demonstrate that the elastic, load-bearing regions in a metallic glass are not randomly distributed but rather form an interconnected backbone that surrounds pockets of residual liquidity. This description of heterogeneous structure is consistent with molecular

dynamics studies of Cu-Zr and Cu-Nb binary alloys[89–91], where icosahedral clusters were observed to form a stiff, interconnected network enclosing regions populated with less efficiently packed clusters.

The notion of heterogeneous structure derived from quenched-in liquidity is further corroborated by anelastic deformation behavior seen in BMGs. Anelasticity has been observed in metallic glasses even shortly following the discovery of the material[92,93]. Argon and Shi argued that isolated STZs could reverse their transformation when the load is removed, driven by the back stress from the elastic matrix and resulting in anelastic strain recovery[80]. In a notable study, Atzmon *et al*. wrapped melt-spun ribbons of an Al-based metallic glass around a mandrel for an extended period of time[94]. Upon release from the mandrel, the curvature of the ribbon gradually returned to its preloaded state after an initial recovery of elastic strain. In their theoretical analysis, a series of viscoelastic Voigt elements, which consist of a viscous (liquid) component in parallel with an elastic (solid) component, were used to model the anelastic behavior. The usage of the Voigt model implicitly requires the liquid-like regions to be constrained by an interconnected elastic backbone or matrix. If the reverse were true, anelastic strain recovery would be unattainable, as no driving force for strain recovery can be exerted by a disconnected spatial arrangement of the elastic regions.

More recent attempts have been made to directly image heterogeneous structure in various metallic glasses. Wagner *et al.* used an atomic force acoustic microscopy method to measure contact resonance frequencies of a melt-spun Pd-based BMG with a cantilever atomic force microscopy (AFM) tip[95]. The resonance frequency is directly related to the contact stiffness, from which the indentation modulus can be derived by applying equations from Hertzian contact theory. Significant spatial variation of modulus was observed within 200 x 200 nm probed areas (Fig.

1.9b). In comparison with experiments conducted on the crystallized alloy as well as single-crystal $SrTiO_3$, the statistical distributions of the measured contact frequencies in the BMG were approximately two orders of magnitude broader, confirming the real existence of nanoscale heterogeneous structure. Based on the images shown in the study, the size of the elastic fluctuations appeared to be on the order of tens of nanometers. This length scale of elastic heterogeneity exceeded the expected size of individual STZs by at least an order of magnitude, suggesting that while the elastically compliant regions were not themselves STZs, it is plausible that they contained a denser population of low-energy flow defects compared to the stiff regions.

Chen *et al.* employed a dynamic AFM technique to map the local viscoelastic phase shift of a thin film Zr-based BMG[96] (Fig. 1.9c). The authors interpreted regions of higher phase shift as more liquid-like, or displaying a stronger tendency to dissipate energy by atomic reconfiguration mechanisms versus storing it elastically. The characteristic size of the heterogeneities (~2 nm) were also similar to the proposed size of individual STZs, leading to the conclusion that the regions of high energy dissipation may represent actual flow defects. In subsequent work, the temporal evolution of the heterogeneous nanostructure at various sub-T_g annealing temperatures was explored[97]. The characteristic size of the heterogeneities were found to diminish with annealing time, in parallel with the loss of enthalpy due to β-relaxation. Characteristic "relaxation" times were extracted from both the structure and enthalpy evolution curves, and activation energies calculated via the Arrhenius relationship between relaxation time and temperature. The associated activation energies for the evolution of heterogeneous structure and enthalpy were very similar, leading the authors to conclude that the changes observed in the energy dissipation (phase shift) maps were the direct result of annealing-induced structural relaxation.

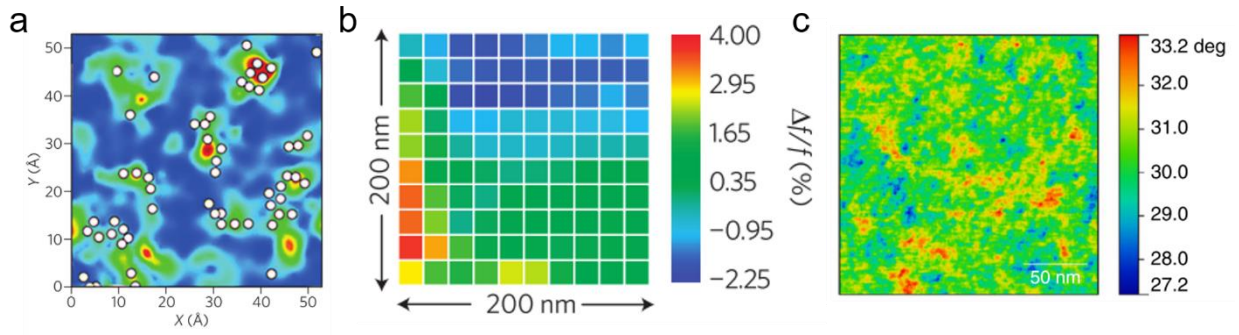

Figure 1.9 Visual evidence of heterogeneous structure in metallic glasses. **(a)** Nanoscale heterogeneous distribution of soft spots in a simulated $Cu_{64}Zr_{36}$ alloy. **(b)** Local variation of indentation modulus in a melt-spun Pd-based BMG, measured by acoustic AFM. **(c)** Nanoscale fluctuations of viscoelastic phase shift (energy dissipation) observed in a thin film Zr-based BMG. Images (a), (b), and (c) taken from refs. 86, 95, and 97, respectively.

In another dynamic AFM study by a different group, sub-T_g thermal annealing was carried out with a thin film Zr-Ni binary metallic glass[98,99]. Again, the heterogeneous nanoscale structure was observed to evolve with annealing time, displaying gradual annihilation of the liquid-like (high-dissipation) features in favor of more solid-like (low-dissipation) features. These results from the annealing study offered visual evidence for the well-established phenomenon of relaxation-induced embrittlement of BMG alloys, and also highlighted the important role of "soft" heterogeneities on macroscopic plasticity. In a follow-up study, a flat punch indenter tip was used to indent a thin film Zr-Ni alloy of the same composition with different maximum applied loads[100]. The central region of each indent was then mapped with dynamic AFM. Histograms of energy dissipation showed that indentation increased the fraction of liquidity in the glass, opposite from the previously reported trend caused by structural relaxation.

The studies described above illustrates some of the prominent examples of current efforts to delineate the details of heterogeneous structure in amorphous alloys, but the direct influence of heterogeneities on macroscopic deformation behavior is still unknown. Specifically, although STZs and flow defects have formed the main focus of research in the community with regards to

plasticity in BMGs, they represent only the initial stages of plastic deformation. Beyond the onset of global yielding, the carriers of plastic flow at ambient temperatures are shear bands. Increasing the fraction of liquid-like heterogeneous regions in the glass would likely improve plasticity by encouraging the formation of multiple shear bands, but it is also imperative to determine the effect of heterogeneous features on the growth and development of the shear bands once they are formed. Furthermore, all of the AFM studies of heterogeneous structure have been performed on vapor-deposited thin film or melt-spun metallic glass specimens. It remains to be investigated whether the same heterogeneous nanostructures that have been reported in vapor-deposited thin film specimens are also present in bulk samples, where the involved quench rates are significantly lower.

1.7 Dissertation Outline

With the overview in this chapter serving as a background for this thesis work, the remaining chapters are divided into two major sections. Following Chapter 2, which provides a detailed review of the various methods employed, Chapter 3 and 4 covers the development of a laser-assisted, high-throughput experimental methodology to systematically explore glass formation and mechanical properties in a more efficient manner than the traditional serial approach. In Chapter 3, the focus is proof of concept, using the well-studied Cu-Zr binary system to validate the experimental methodology. The work detailed in Chapter 4 makes advancements by adapting the high-throughput methodology to interrogate glass formation in the much larger composition space of a ternary system and identifying within that space the optimum glass former. The second major section, comprising Chapters 5 – 7, describes the investigation of heterogeneous structure in BMGs using two methods, instrumented nanoindentation and dynamic modulus mapping. Chapter 5 discusses heterogeneous structure of a Zr-based BMG when processed by

conventional drop casting. Chapter 6 describes the observation of evolving heterogeneous structure within the same BMG when processed with a range of different laser heat inputs, or equivalently, different effective cooling rates. Based on analysis of the accumulated nanoindentation results, Chapter 7 introduces a new parameter, the plastic work ratio, for determining the intrinsic plasticity of BMG alloys through nanoindentation. Chapter 8 concludes the dissertation with summary and outlook.

1.8 References

1. Klement, W., Willens, R. & Duwez, P. Non-crystalline Structure in Solidified Gold-Silicon Alloys. *Nature* **187,** 869–870 (1960).
2. Inoue, A., Zhang, T. & Masumoto, T. Al-La-Ni Amorphous Alloys with a Wide Supercooled Liquid Region.pdf. *Mater. Trans. JIM* **30,** 965–972 (1989).
3. Peker, A. & Johnson, W. L. A highly processable metallic glass: Zr41.2Ti13.8Cu12.5Ni10.0Be22.5. *Appl. Phys. Lett.* **63,** 2342–2344 (1993).
4. Inoue, A., Nishiyama, N. & Kimura, H. Preparation and Thermal Stability of Bulk Amorphous Pd40Cu30Ni10P20 Alloy Cylinder of 72 mm in Diameter. *Mater. Trans. JIM* **38,** 179–183 (1997).
5. Schuh, C., Hufnagel, T. & Ramamurty, U. Mechanical behavior of amorphous alloys. *Acta Mater.* **55,** 4067–4109 (2007).
6. Schroers, J. Processing of bulk metallic glass. *Adv. Mater.* **22,** 1566–97 (2010).
7. Hays, C. C. *et al.* Vitrification and determination of the crystallization time scales of the bulk-metallic-glass-forming liquid Zr58.5Nb2.8Cu15.6Ni12.8Al10.3. *Appl. Phys. Lett.* **79,** 1605–1607 (2001).
8. Turnbull, D. Under what conditions can a glass be formed ? *Contemp. Phys.* **10,** 473–488 (1969).
9. Inoue, A., Zhang, W., Zhang, T. & Kurosaka, K. High-strength Cu-based bulk glassy alloys in Cu–Zr–Ti and Cu–Hf–Ti ternary systems. *Acta Mater.* **49,** 2645–2652 (2001).
10. Inoue, A., Zhang, T. & Masumoto, T. Glass-forming ability of alloys. *J. Non. Cryst. Solids* **156–158,** 473–480 (1993).
11. Shen, T. D., He, Y. & Schwarz, R. B. Bulk amorphous Pd–Ni–Fe–P alloys: Preparation and characterization. *J. Mater. Res.* **14,** 2107–2115 (2011).

12. Long, Z. *et al.* On the new criterion to assess the glass-forming ability of metallic alloys. *Mater. Sci. Eng. A* **509,** 23–30 (2009).

13. Waniuk, T. A., Schroers, J. & Johnson, W. L. Critical cooling rate and thermal stability of Zr–Ti–Cu–Ni–Be alloys. *Appl. Phys. Lett.* **78,** 1213–1215 (2001).

14. Lu, Z. P. & Liu, C. T. A new glass-forming ability criterion for bulk metallic glasses. *Acta Mater.* **50,** 3501–3512 (2002).

15. Li, Y. Formation, Structure and Properties of Bulk Metallic Glasses.pdf. *J. Mater. Sci. Technol.* **15,** 97–110 (1999).

16. Inoue, A. STABILIZATION OF METALLIC SUPERCOOLED LIQUID. *Acta Mater.* **48,** 279–306 (2000).

17. Inoue, A. Stabilization of metallic supercooled liquid and bulk amorphous alloys. *Acta Mater.* **48,** 279–306 (2000).

18. Cheng, Y. Q. & Ma, E. Atomic-level structure and structure–property relationship in metallic glasses. *Prog. Mater. Sci.* **56,** 379–473 (2011).

19. Sheng, H. W., Luo, W. K., Alamgir, F. M., Bai, J. M. & Ma, E. Atomic packing and short-to-medium-range order in metallic glasses. *Nature* **439,** 419–25 (2006).

20. Hirata, A. *et al.* Direct observation of local atomic order in a metallic glass. *Nat. Mater.* **10,** 28–33 (2011).

21. Shen, T. D., Harms, U. & Schwarz, R. B. Correlation between the volume change during crystallization and the thermal stability of supercooled liquids. *Appl. Phys. Lett.* **83,** 4512–4514 (2003).

22. Gaskell, P. H. Medium-range structure in glasses and low-Q structure in neutron and X-ray scattering data. *J. Non. Cryst. Solids* **351,** 1003–1013 (2005).

23. Cargill, G. S. & Spaepen, F. Description of chemical ordering in amorphous alloys. *J. Non. Cryst. Solids* **43,** 91–97 (1981).

24. Ruppersberg, H. *et al.* Observation of chemical short-range order in an amorphous Ni40Ti60 alloy. *J. Phys. F-metal Phys.* **10**, 1645-1652 (1980).

25. Gardner, P. P. *et al.* Chemical short-range order in liquid and amorphous Cu66Ti34 alloys. *J. Phys. F-metal Phys.* **11**, L157–62 (1981).

26. Manh, D. N., Mayou, D., Cyrotlackmann, F. & Pasturel, A. Electronic-structure and Chemical Short-range Order In Amorphous CuZr and NiZr Alloys. *J. Phys. F-metal Phys.* **17,** 1309–1321 (1987).

27. Riegner, D. C. Molecular Dynamics Simulations of Metallic Glass Formation and Structure. (The Ohio State University, 2016).

28. Agrawal, A. Computational Study of Vanadate and Bulk Metallic Glasses. (The Ohio

State University, 2012).

29. Finney, J. L. Modelling the structures of amorphous metals and alloys. *Nature* **266,** 309–314 (1977).

30. Fukunaga, T. *et al.* Voronoi analysis of the structure of Cu-Zr and Ni-Zr metallic glasses. *Intermetallics* **14,** 893–897 (2006).

31. Böhmer, R. & Angell, C. A. Correlations of the nonexponentiality and state dependence of mechanical relaxations with bond connectivity in Ge-As-Se supercooled liquids. *Phys. Rev. B* **45,** 10091–10094 (1992).

32. Angell, C. A. Perspectives on the Glass Transition. *J. Phys. Chem. Solids* **49,** 863–871 (1988).

33. Senkov, O. N. Correlation between fragility and glass-forming ability of metallic alloys. *Phys. Rev. B* **76,** 104202:1–6 (2007).

34. Tanaka, H. Relationship among glass-forming ability, fragility, and short-range bond ordering of liquids. *J. Non. Cryst. Solids* **351,** 678–690 (2005).

35. Ding, J., Cheng, Y. Q., Sheng, H. & Ma, E. Short-range structural signature of excess specific heat and fragility of metallic-glass-forming supercooled liquids. *Phys. Rev. B* **85,** 060201:1–5 (2012).

36. Cheng, Y. Q., Sheng, H. W. & Ma, E. Relationship between structure, dynamics, and mechanical properties in metallic glass-forming alloys. *Phys. Rev. B* **78,** 014207:1–7 (2008).

37. Ding, J., Cheng, Y. Q. & Ma, E. Full icosahedra dominate local order in Cu64Zr34 metallic glass and supercooled liquid. *Acta Mater.* **69,** 343–354 (2014).

38. Mauro, N. A., Blodgett, M., Johnson, M. L., Vogt, A. J. & Kelton, K. F. A structural signature of liquid fragility. *Nat. Commun.* **5,** 4616 (2014).

39. Bernal, J. D. Packing of Spheres: Co-ordination of Randomly Packed Spheres. *Nature* **188,** 910–911 (1960).

40. Bernal, J. D. Geometry of the Structure of Monatomic Liquids. *Nature* **185,** 68–70 (1960).

41. Gaskell, P. H. A new structural model for amorphous transition metal silicides, borides, phosphides and carbides. *J. Non. Cryst. Solids* **32,** 207–224 (1979).

42. Miracle, D. B. A structural model for metallic glasses. *Nat. Mater.* **3,** 697–702 (2004).

43. Miracle, D. B. The efficient cluster packing model – An atomic structural model for metallic glasses. *Acta Mater.* **54,** 4317–4336 (2006).

44. Laws, K. J., Miracle, D. B. & Ferry, M. A predictive structural model for bulk metallic glasses. *Nat. Commun.* **6,** 8123 (2015).

45. Kaban, I. *et al.* Local atomic arrangements and their topology in Ni–Zr and Cu–Zr glassy and crystalline alloys. *Acta Mater.* **61,** 2509–2520 (2013).

46. Guo, S., Lu, Z. P. & Liu, C. T. Identify the best glass forming ability criterion. *Intermetallics* **18,** 883–888 (2010).

47. Guo, S. & Liu, C. T. New glass forming ability criterion derived from cooling consideration. *Intermetallics* **18,** 2065–2068 (2010).

48. Li, A. Y., Guo, Q., Kalb, J. A., Thompson, C. V & Li, Y. Matching Glass-Forming Ability with the Density of the Amorphous Phase. *Science* **322,** 1816–1819 (2008).

49. Xu, D., Lohwongwatana, B., Duan, G., Johnson, W. L. & Garland, C. Bulk metallic glass formation in binary Cu-rich alloy series – Cu100−xZrx (x=34, 36, 38.2, 40 at.%) and mechanical properties of bulk Cu64Zr36 glass. *Acta Mater.* **52,** 2621–2624 (2004).

50. Wang, W. H., Lewandowski, J. J. & Greer, a. L. Understanding the glass-forming ability of Cu50Zr50 alloys in terms of a metastable eutectic. *J. Mater. Res.* **20,** 2307–2313 (2005).

51. Duan, G. *et al.* Molecular dynamics study of the binary Cu46Zr54 metallic glass motivated by experiments: Glass formation and atomic-level structure. *Phys. Rev. B* **71,** 224208:1–9 (2005).

52. Hofmann, D. C., Duan, G. & Johnson, W. L. TEM study of structural evolution in a copper mold cast Cu46Zr54 BMG. *Scr. Mater.* **54,** 1117–1122 (2005).

53. Choi-Yim, H., Xu, D. & Johnson, W. L. Ni-based bulk metallic glass formation in the Ni–Nb–Sn and Ni–Nb–Sn–X (X=B,Fe,Cu) alloy systems. *Appl. Phys. Lett.* **82,** 1030–1032 (2003).

54. Deng, Y. P. *et al.* A combinatorial thin film sputtering approach for synthesizing and chracterizing ternary ZrCuAl metallic glasses. *Intermetallics* **15,** 1208–1216 (2007).

55. Chen, C. J. *et al.* On the amorphous and nanocrystalline Zr-Cu and Zr-Ti co-sputtered thin films. *J. Alloys Compd.* **483,** 337–340 (2009).

56. Chou, H. S. *et al.* Amorphous and nanocrystalline sputtered Mg-Cu thin films. *J. Alloys Compd.* **483,** 341–345 (2009).

57. Ding, S., Gregoire, J., Vlassak, J. J. & Schroers, J. Solidification of Au-Cu-Si alloys investigated by a combinatorial approach. *J. Appl. Phys.* **111,** 114901:1–6 (2012).

58. Ding, S. *et al.* Combinatorial development of bulk metallic glasses. *Nat. Mater.* **13,** 1–7 (2014).

59. Evertz, S. *et al.* Revealing the relationships between chemistry , topology and stiffness of ultrastrong Co-based metallic glass thin films: A combinatorial approach. *Acta Mater.* **107,** 213–219 (2016).

60. Yu, H. Bin, Luo, Y. & Samwer, K. Ultrastable metallic glass. *Adv. Mater.* **25,** 5904–5908

(2013).

61. Gu, D. D., Meiners, W., Wissenbach, K. & Poprawe, R. Laser additive manufacturing of metallic components: materials, processes and mechanisms. *Int. Mater. Rev.* **57,** 133–164 (2012).

62. Bontha, S., Klingbeil, N. W., Kobryn, P. A. & Fraser, H. L. Thermal processing maps for predicting solidification microstructure in laser-fabrication of thin-wall structures. *J. Mater. Process. Technol.* **178,** 135–142 (2006).

63. Yang, G. L. *et al.* Laser solid forming Zr-based bulk metallic glass. *Intermetallics* **22,** 110–115 (2012).

64. Zheng, B., Zhou, Y., Smugeresky, J. E. & Lavernia, E. J. Processing and Behavior of Fe-Based Metallic Glass Components via Laser-Engineered Net Shaping. *Metall. Mater. Trans. A* **40,** 1235–1245 (2009).

65. Petters, R., Stoica, M., Scudino, S., Pauly, S. & Lo, L. Processing metallic glasses by selective laser melting. *Mater. Today* **16,** 37–41 (2013).

66. Chen, B. Q. *et al.* Surface vitrification of alloys by laser surface treatment. *J. Alloys Compd.* **511,** 215–220 (2012).

67. Sun, H. & Flores, K. M. Microstructural Analysis of a Laser-Processed Zr-Based Bulk Metallic Glass. *Metall. Mater. Trans. A* **41,** 1752–1757 (2010).

68. Banerjee, R., Collins, P. C., Bhattacharyya, D., Banerjee, S. & Fraser, H. L. Microstructural evolution in laser deposited compositionally graded titanium-vanadium alloys. *Acta Mater.* **51,** 3277–3292 (2003).

69. Collins, P. C., Banerjee, R., Banerjee, S. & Fraser, H. L. Laser deposition of compositionally graded titanium-vanadium and titanium-molybdenum alloys. *Mater. Sci. Eng. A* **352,** 118–128 (2003).

70. Carvalho, P. M. *et al.* Automated workstation for variable composition laser cladding - its use for rapid alloy scanning. *Surf. Coatings Technol.* **72,** 62–70 (1995).

71. Vilar, R. & Colaco, R. Laser-assisted combinatorial methods for rapid design of wear resistant iron alloys. *Surf. Coatings Technol.* **203,** 2878–2885 (2009).

72. Zhang, Y. Z., Meacock, C. & Vilar, R. Laser powder microdeposition of compositional gradient Ti-Cr alloy. *Mater. Des.* **31,** 3891–3895 (2010).

73. Hofmann, D. C. *et al.* Developing Gradient Metal Alloys through Radial Deposition Additive Manufacturing. *Sci. Rep.* **4,** 5357 (2014).

74. Banerjee, R., Nag, S. & Fraser, H. L. A novel combinatorial approach to the development of beta titanium alloys for orthopaedic implants. *Mater. Sci. Eng. C* **25,** 282–289 (2005).

75. Johnson, W. L. Is metallic glass poised to come of age? *Nat. Mater.* **14,** 553–555 (2015).

76. Spaepen, F. A microscopic mechanism for steady state inhomogeneous flow in metallic glasses. *Acta Metall.* **25,** 407–415 (1977).

77. Argon, A. . Plastic deformation in metallic glasses. *Acta Metall.* **27,** 47–58 (1979).

78. Murali, P. & Ramamurty, U. Embrittlement of a bulk metallic glass due to sub-Tg annealing. *Acta Mater.* **53,** 1467–1478 (2005).

79. Launey, M. E., Busch, R. & Kruzic, J. J. Effects of free volume changes and residual stresses on the fatigue and fracture behavior of a Zr-Ti-Ni-Cu-Be bulk metallic glass. *Acta Mater.* **56,** 500–510 (2008).

80. Argon, A. S. & Shi, L. T. Development of visco-plastic deformation in metallic glasses. *Acta Metall.* **31,** 499–507 (1983).

81. Argon, A. S. & Kuo, H. Y. Plastic flow in a disordered bubble raft (an analog of a metallic glass). *Mater. Sci. Eng.* **39,** 101–109 (1979).

82. Falk, M. L. & Langer, J. S. Dynamics of viscoplastic deformation in amorphous solids. *Phys. Rev. E* **57,** 7192–7205 (1998).

83. Johnson, W. L. & Samwer, K. A universal criterion for plastic yielding of metallic glasses with a (T/Tg)2/3 temperature dependence. *Phys. Rev. Lett.* **95,** 2–5 (2005).

84. Zink, M., Samwer, K., Johnson, W. L. & Mayr, S. G. Plastic deformation of metallic glasses: Size of shear transformation zones from molecular dynamics simulations. *Phys. Rev. B* **73,** 172203:1–3 (2006).

85. Ding, J., Patinet, S., Falk, M. L., Cheng, Y. & Ma, E. Soft spots and their structural signature in a metallic glass. *Proc. Natl. Acad. Sci.* **111,** 14052–14056 (2014).

86. Ma, E. Tuning order in disorder. *Nat. Mater.* **14,** 547–552 (2015).

87. Ma, E. & Ding, J. Tailoring structural inhomogeneities in metallic glasses to enable tensile ductility at room temperature. *Mater. Today*, in press (2016).

88. Dmowski, W., Iwashita, T., Chuang, C. P., Almer, J. & Egami, T. Elastic Heterogeneity in Metallic Glasses. *Phys. Rev. Lett.* **105,** 205502:1–4 (2010).

89. Baumer, R. E. & Demkowicz, M. J. Glass Transition by Gelation in a Phase Separating Binary Alloy. *Phys. Rev. Lett.* **110,** 145502:1– 5 (2013).

90. Lee, M., Lee, C. M., Lee, K. R., Ma, E. & Lee, J. C. Networked interpenetrating connections of icosahedra: Effects on shear transformations in metallic glass. *Acta Mater.* **59,** 159–170 (2011).

91. Shi, Y. & Falk, M. L. Does metallic glass have a backbone? The role of percolating short range order in strength and failure. *Scr. Mater.* **54,** 381–386 (2006).

92. Chen, H. S., Leamy, H. J. & Barmatz, M. The elastic and anelastic behavior of a metallic glass. *J. Non. Cryst. Solids* **5,** 444–448 (1971).

93. Taub, A. I. & Spaepen, F. Ideal Elastic, Anelastic, and Viscoelastic Flow in a Metallic Glass. *J. Mater. Sci.* **16,** 3087–3092 (1981).

94. Ju, J. D., Jang, D., Nwankpa, A. & Atzmon, M. An atomically quantized hierarchy of shear transformation zones in a metallic glass. *J. Appl. Phys.* **109,** 053522:1–8 (2011).

95. Wagner, H. *et al.* Local elastic properties of a metallic glass. *Nat. Mater.* **10,** 439–42 (2011).

96. Liu, Y. H. *et al.* Characterization of nanoscale mechanical heterogeneity in a metallic glass by dynamic force microscopy. *Phys. Rev. Lett.* **106,** 125504:1–4 (2011).

97. Zhu, F. *et al.* Intrinsic correlation between β-relaxation and spatial heterogeneity in a metallic glass. *Nat. Commun.* **7,** 11516 (2016).

98. Yang, Y. *et al.* Fractal growth of the dense-packing phase in annealed metallic glass imaged by high-resolution atomic force microscopy. *Acta Mater.* **60,** 5260–5272 (2012).

99. Ke, H. B., Zeng, J. F., Liu, C. T. & Yang, Y. Structure Heterogeneity in Metallic Glass: Modeling and Experiment. *J. Mater. Sci. Technol.* **30,** 560–565 (2014).

100. Lu, Y. M. *et al.* Structural Signature of Plasticity Unveiled by Nano-Scale Viscoelastic Contact in a Metallic Glass. *Sci. Rep.* **6,** 29357 (2016).

Chapter 2

Methods – Sample Preparation, Characterization, and Analysis

The purpose of this chapter is to provide an encompassing description of select experimental and analytical methods employed in this thesis work, in more detail than could be necessarily found in subsequent chapters. Some methods, such as the operating principles of scanning and transmission electron microscopy, are commonplace in the field of materials science and are thus excluded from discussion. Special attention is devoted towards details that may be considered peripheral to the main thrust and story of the work, but are necessary if the work is to be reproduced or continued in future studies.

2.1 Sample Preparation

2.1.1 Laser-Engineered Net Shaping (LENS^{TM})

All samples in the combinatorial, high-throughput studies were fabricated with an Optomec MR-7 LENS system. As briefly described in Chapter 1, the LENS process, also referred to in this thesis as laser deposition or laser additive manufacturing, is a 3-d printing technique involving metallic powders as the printing medium. The main components of the instrument is a continuous fiber-optic laser with wavelength of 1.06 μm and controllable power up to 500 W, a powder delivery system with four individual hoppers, and a moving stage upon which substrates can be fixed. During operation, the laser beam is directed down a vertical column, passes through a focusing lens, and impinges on the substrate surface to create a local melt pool, the size of which depends on the applied laser power, the optical and thermal properties of the material being melted, and the power distribution of the beam; according to the manufacturer of the machine, it can be assumed that the power distribution is approximately Gaussian. To deposit material, a convergent

stream of metal powder delivered to the substrate is incorporated into the melt pool. The powder delivery rate is set by the operator in units of rpm, corresponding to the rotational speed of the delivery mechanism. Finally, x-y motors that control the in-plane motion of the stage relative to the laser enable deposition of user-defined layer geometries. The entire process occurs within an argon-filled glovebox with oxygen concentration maintained below 5 ppm. Figure 2.1 summarizes the basic principles of the operation.

In the proprietary software package included with the machine, the speed of the stage, or equivalently of the laser, as well as the powder delivery rates are fixed during the deposition of a single layer. The 2-d compositionally-graded specimens produced in this thesis work involved changing both laser travel speed and powder delivery rates across a single deposited layer. To accomplish this, individualized scripts in machine code language were prepared.

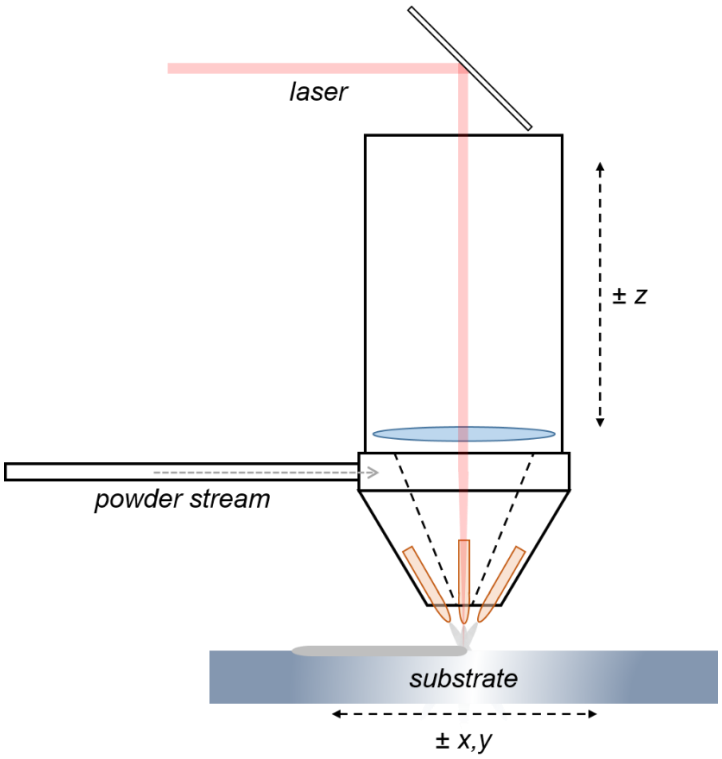

Figure 2.1 Schematic illustrating the basic operating components (laser, powder delivery mechanism, motor controlled stage) of the LENS process.

In order to control the chemical composition of the deposits in situ when multiple types of elemental powders are simultaneously delivered from different hoppers, it is necessary to know the powder delivery rates in mass per unit time rather than rpm. For each powder, a linear relationship between rpm and g/min delivery rates can be derived by weighing the mass of powder expelled through the nozzles over a period of time for a specific rpm. To collect the powder, plastic bags or containers can be held beneath the nozzles. A "conversion" plot shown in Figure 2.2 is constructed after repeating the weighing for several different rpm delivery rates. A linear fit to the data allows the mass delivery rate to be directly converted from the rpm values. Because powders purchased from different sources could potentially have very different distributions of particle size and morphology, a conversion plot must be created for each new batch of powder prior for use in deposition experiments.

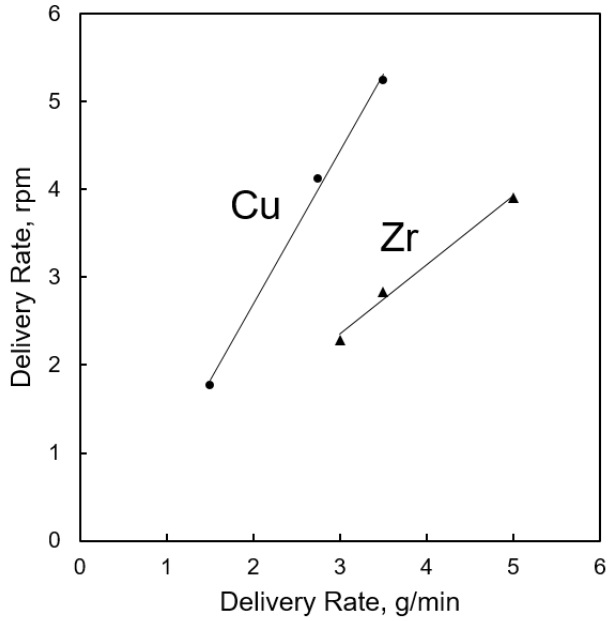

Figure 2.2 Powder delivery rate conversion plot for zirconium and copper powders.

2.1.2 Plasma arc-melting and casting

Elemental feedstock of Zr, Cu, Ni, Al, and Nb, each with purities of 99.9 at. % or higher were used to synthesize bulk metallic glass samples of $Zr_{58.5}Cu_{15.6}Ni_{12.8}Al_{10.3}Nb_{2.8}$. The pure constituents were stoichiometrically weighed to a total mass of 25 g and then cleaned in a sonicated bath of methanol. Once dried, the 25 g charges were positioned apart from each other on a water-cooled copper hearth within the chamber of the plasma arc melter. An isolated piece of titanium functioning as an oxygen getter was also placed on the hearth. Prior to melting, air in the chamber was evacuated with a turbo pump and backfilled with pure argon gas. The pump-backfill cycle was repeated three times to ensure an inert oxygen-free atmosphere within the chamber. After melting the piece of titanium with a plasma arc for a minimum of a minute to remove traces of residual oxygen from the atmosphere within the chamber, the charges were melted sequentially to combine the pure elements into pre-alloyed buttons. Each button was subsequently flipped and re-melted at least twice to ensure uniform and thorough mixing of the constituents.

To fabricate the amorphous 3 mm diameter rod samples, multiple pre-alloyed buttons were combined by arc-melting together on a copper hearth that features a lip for pouring the molten metal. Again, titanium was melted first before melting the Zr-based alloy. Once molten, the hearth was quickly tilted in a single motion to transfer the liquid into a copper mold positioned beneath the lip of the hearth. Before refilling the chamber with air to remove the cast specimen, the specimen was allowed to cool for at least 15 minutes to prevent the occurrence of severe surface oxidation.

2.1.3 Preparation of TEM foils by conventional ion milling

A combination of mechanical thinning and conventional ion milling was used to prepare TEM foils from the 3 mm diameter rod specimens. Beginning with 600 grit SiC paper and

finishing with 1200 grit SiC paper, the individual rod segments were thinned with an automated parallel-plate polisher to a final thickness of approximately 30 μm. The samples were then transferred, one at a time, to the ion mill for further thinning. Two incident ion beams, one illuminating the top of the sample, and the other the bottom, crosses each other at a 90 degree angle such that the rate of material attrition is highest at the center of the sample. During milling, the sample is also continuously rotated about the central axis. An accelerating potential of 5 kV was used and the angle of incidence for both beams was fixed at 5 degrees. Milling was performed in 30 minute intervals until a small pinhole is formed at the center of the sample. Regions surrounding the edge of the pinhole are electron transparent. To expand the area of electron transparency as well as improve the quality of the surface finish for high resolution TEM, the sample was milled for another 15 – 20 minutes with a reduced voltage of 3.5 kV and an angle of incidence between 2-3 degrees. The complete process is summarized in Figure 2.3.

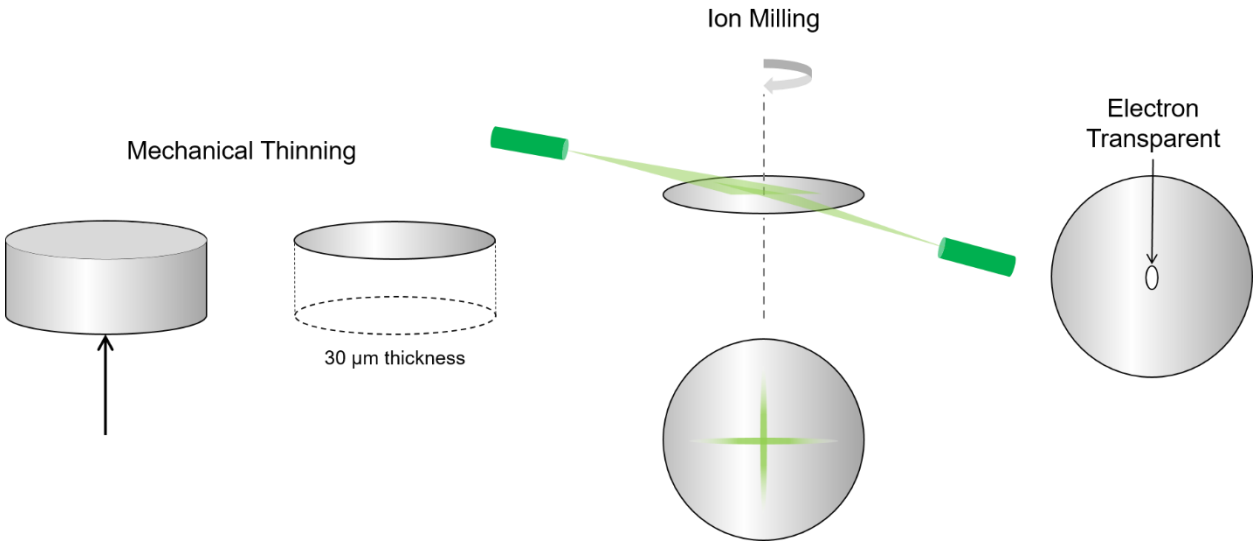

Figure 2.3 From left to right, the process flow for preparing TEM foils by mechanical thinning and conventional ion milling.

2.2 Characterization

2.2.1 Differential Interference Contrast (DIC) Microscopy

Reflected light DIC microscopy enhances the appearance of topographical features on an otherwise smooth specimen surface. We employed this technique to rapidly screen for potentially amorphous material in the laser processed specimens. Enhanced topographical contrast is made possible by the combined effect of polarized light passing through a Nomarski or Wollaston prism, illustrated in Figure 2.4. The prisms are constructed by gluing together two optically transparent calcite crystals with perpendicular optic axes. An incident wave of polarized light is sheared into

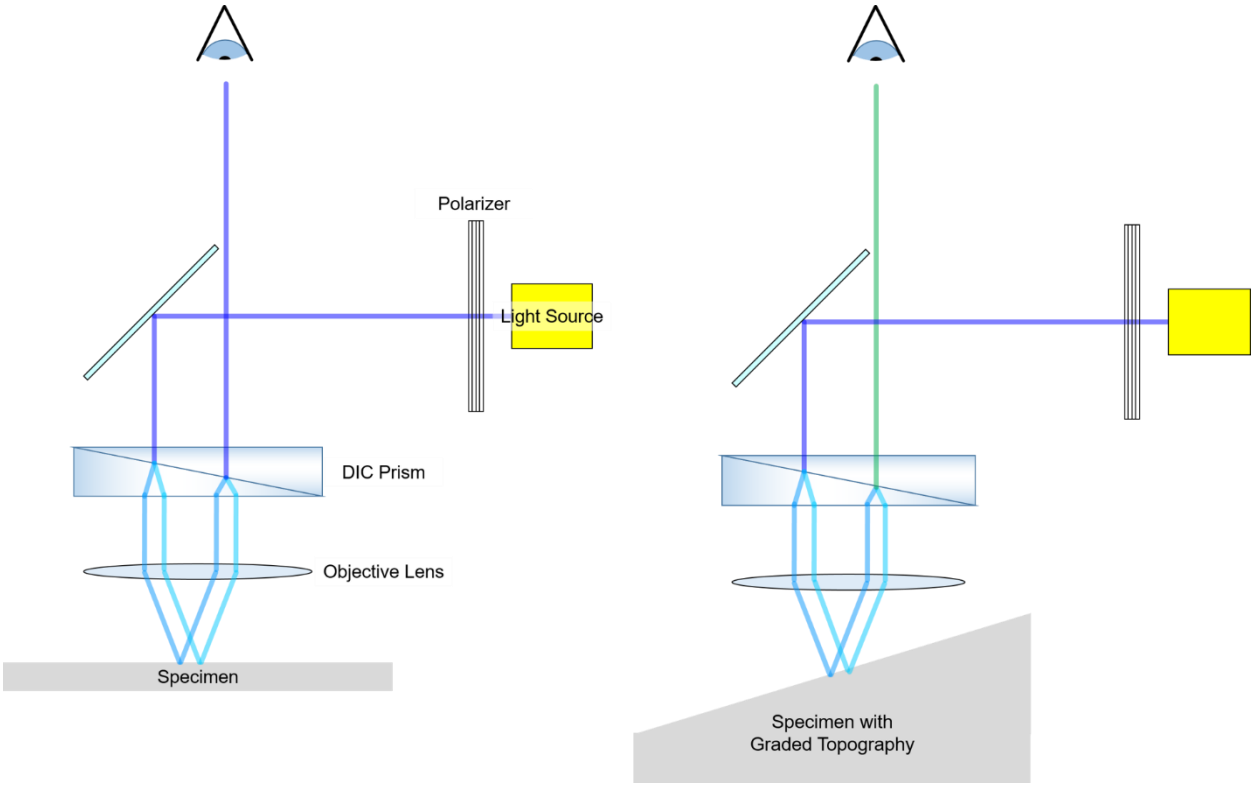

Figure 2.4 Schematic of reflected light DIC microscopy. The prism splits a polarized wave from the light source into two orthogonal components. Graded topography causes a difference in the path length of the reflected component waves. When recombined by the prism, the resulting wave is of a different color than the incident wave.

two orthogonal components that are offset from one another in position when passing through the interface of the prism. If the sample surface is perfectly flat, the reflected components recombine at the prism interface to form a reflected wave with wavelength identical to the incident polarized light (Fig. 2.4a). However, if a gradient exists in the topography of the surface, it will induce a path difference between the reflected component waves, which upon recombining produces a reflected wave of a different color than the incident wave (Fig. 2.4b). The steeper the gradient is, the greater will be the enhanced contrast.

2.2.2 Thermal Imaging by Hybrid Algorithm Pyrometry

A built-in two-color pyrometer housed within the LENS MR-7 enabled in situ acquisition of the surface temperature profile during laser processing (Fig. 2.5).

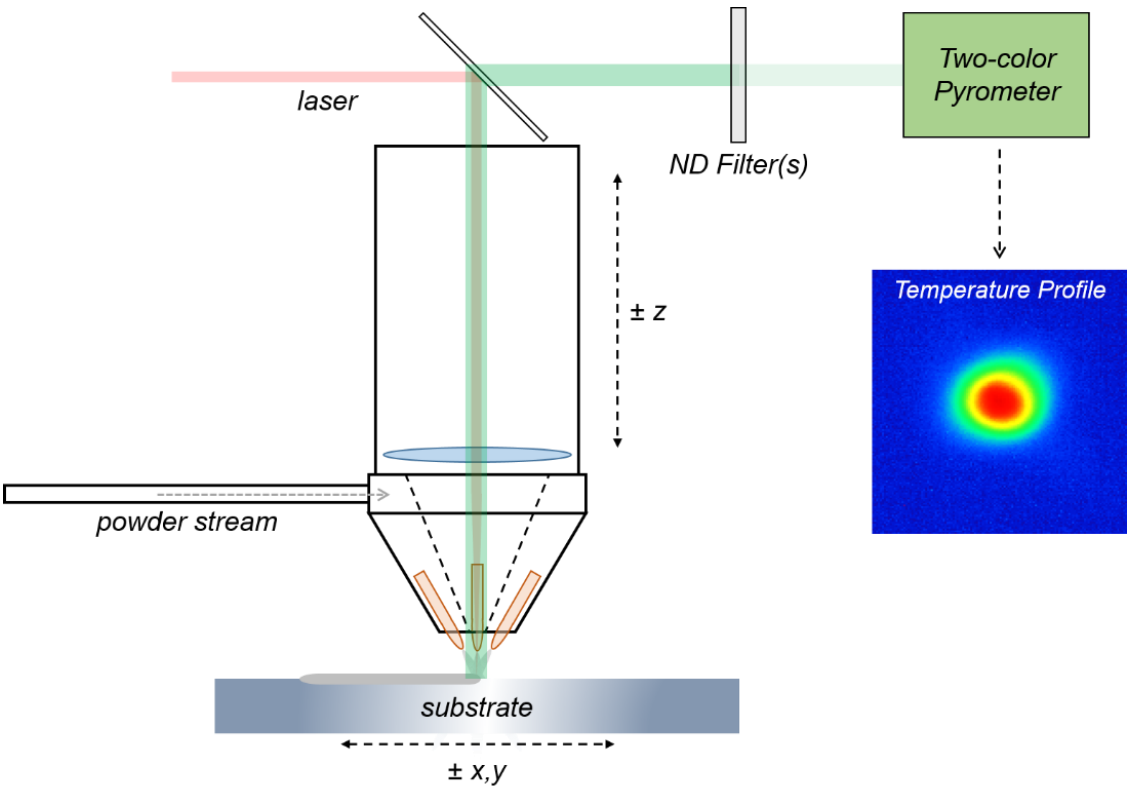

Figure 2.5 Schematic of the thermal imaging setup integrated into the LENS MR-7.

Two wavelengths (λ_1 and λ_2) of the infrared signal emitted by the melt pool travel through the vertical deposition column and are detected by the pyrometer after being reflected from a set of mirrors. The spectral radiance of the target material is assumed to be some fraction ε of that of a blackbody emitter (B_ν) according to Planck's law:

$$B_\nu(\nu,T) = \frac{2h\nu^3}{c^2}\frac{1}{e^{\frac{h\nu}{k_BT}}-1} \qquad (2.1)$$

where h is Planck's constant, ν is the frequency of the light, c is the speed of light in vacuum, and k_B is Boltzmann's constant. The theoretical intensity of an emitted wavelength λ_0 (or frequency ν_0) is then given by the following differential equation:

$$I(\nu_0,T) = \varepsilon B_\nu(\nu_0,T)d\nu \qquad (2.2)$$

In general, the measured intensity differs from the theoretical quantity by a linear scaling factor that is unique to the experimental setup. In single color pyrometry, the temperature is directly calculated from the measured intensity of a detected wavelength if the scaling factor is known. To this end, a thermocouple is often employed to measure a reference temperature for a given measured intensity, from which the scaling factor is obtained. The obvious disadvantage of one-color pyrometry is that each time a new target material is used, the scaling factor changes.

On the other hand, in two-color pyrometry, the temperature is calculated from the ratio of the respective measured intensities of the two detected wavelengths:

$$R(\nu_1,\nu_2,T) = \left(\frac{\nu_1}{\nu_2}\right)^3 \frac{e^{\frac{h\nu_2}{k_BT}}-1}{e^{\frac{h\nu_1}{k_BT}}-1} \approx \left(\frac{\nu_1}{\nu_2}\right)^3 e^{\frac{h}{k_BT}(\nu_2-\nu_1)} \qquad (2.3)$$

Taking the natural logarithm of both sides of Equation 2.3, we have

$$\ln(R) = 3\ln\left(\frac{\nu_1}{\nu_2}\right) + \frac{h(\nu_2 - \nu_1)}{k_B}\left(\frac{1}{T}\right) \qquad (2.4)$$

Notice that Equation 2.4 does not include the emissivity of the target material and is of the general form $y = mx + b$. Knowing the slope and y-intercept permits direct calculation of temperature from R, irrespective of the target material. In practice, the camera is initially calibrated with a tungsten filament lightbulb that can be set to specific temperatures by tuning the current passing through the filament. A linear fit to a plot of ln(R) versus $1/T$ yields the slope and intercept values.

In order for the emitted infrared signals to reach the detector, they must pass through the focusing lens of the laser, causing minor spherical aberration of the intensity images. The extent of distortion in the images of the two wavelengths are slightly unbalanced, leading to misaligned overlap of the images and significant errors in the computed temperature profile. To remedy these issues, a hybrid algorithm is used that combines both one-color and two-color pyrometry to calculate the complete temperature profile. First, the two-color algorithm measures the temperature at the center of the melt pool, where there is virtually no distortion of the intensity images. With the measured temperature serving as a reference for each collected frame, the one-color algorithm is then used to calculate the remaining temperature distribution.

Cooling rate at a given temperature is obtained from the product of the temperature gradient with the laser travel velocity:

$$\frac{dT}{dt} = \frac{dT}{dx}\frac{dx}{dt} \qquad (2.5)$$

In Equation 2.5, x denotes the laser's direction of travel relative to the fixed substrate. Note that the lateral dimensions of the measured thermal images are in units of pixels. For the present setup,

the conversion factor is 42.1 μm per pixel. A script written in Matlab® (see Appendix) was used to obtain average cooling rate between 1600 ˚C and 2200 ˚C, and for a laser travel speed of 16.9 mm/s.

To achieve greatest accuracy of temperature measurement, the measured intensities of both wavelengths should be approximately within the range of 2000 – 3500 counts. Depending on how brightly the melt pool is glowing for a given material, the number of counts measured for each frame will depend on the exposure time set by the user. For the pyrometry experiments performed in the work described in Chapter 4, double-stacked neutral density filters were placed in the optical path (Fig. 5.2) to bring the measured intensities into the optimal range. Note that for future experiments on different materials or lower range of applied laser power, the number of filters may need to be appropriately reduced.

2.2.3 Instrumented Nanoindentation

Instrumented nanoindentation was used extensively throughout this thesis work, first as a high-throughput characterization tool to establish property-composition trends in a multicomponent metallic glass system, and then to map the spatial variation of properties in a specific BMG alloy. Nanoindentation differ from microindentation techniques primarily in the much smaller volumes of material that are probed. Also, whereas hardness in microindentation tests are calculated by visual measurement of the indent dimensions, hardness (H) and indentation modulus (E_r) measured by instrumented nanoindentation are extracted from the load-displacement (P-h) data according to the analytical methods set forth by Oliver and Pharr[1,2]. Figure 2.6a provides a schematic P-h curve. E_r is derived from the unloading stiffness (S) of the material, evaluated at maximum applied load:

$$E_r = \frac{\sqrt{\pi}}{2}\frac{S}{\sqrt{A_c}}, \; S = \left.\frac{dP}{dh}\right|_{P_{max}} \qquad (2.6)$$

On the other hand, H is defined at the average pressure the probed volume sustains under load:

$$H = \frac{P_{max}}{A_c} \qquad (2.7)$$

In equations 2.6 and 2.7, A_c denotes the contact area, and can be understood as the area where the indenter tip is in full contact with the material at peak load. For a given indenter tip geometry, A_c is a unique function of the associated contact depth h_c (Fig. 2.6b), which can be directly calculated from the load-displacement data:

$$h_c = h_{max} - \varepsilon\left(\frac{P_{max}}{S}\right) \qquad (2.8)$$

where ε is a constant that varies between 0.72 and 1, depending on the tip geometry. For the Berkovich tips used in the thesis work, ε is 0.75.

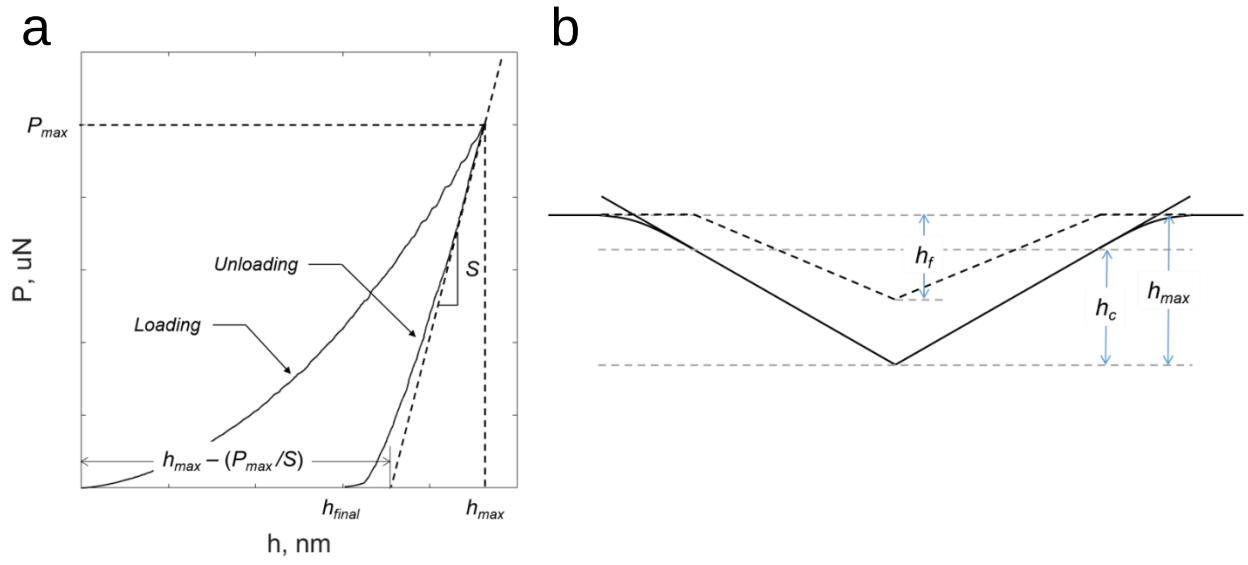

Figure 2.6 (a) Schematic of nanoindentation *P-h* curve and **(b)** representative diagram of section through an indent, showing the various quantities used for calculating *H* and Er.

When an ideal Berkovich tip is infinitely sharp, $A_c = 24.5h_c^2$. In actual practice, a certain degree of bluntness always exists, and $A_c(h_c)$ becomes a more complicated function of the following general form:

$$A_c\ h_c\ = 24.5h_c^{\ 2} + C_1h_c + C_2h_c^{\ 1/2} + C_3h_c^{\ 1/4} + C_4h_c^{\ 1/8} + C_5h_c^{\ 1/16} \qquad (2.9)$$

The coefficients (C_1, C_2, C_3, etc.) of the area function are obtained by first performing a series of indentations with different h_c on a standard specimen of known hardness and modulus (e.g. fused silica, aluminum). A subsequent fit of equation 2.9 to the plotted data points (h_c, A_c) yields the coefficients. Because tip blunting is exacerbated with extended use, new area functions must be created from time to time to maintain accurate determination of indentation properties.

2.2.4 Dynamic Modulus Mapping (DMM)

DMM is a mechanical properties characterization technique that was used to map the 2-d distribution of elastic modulus in monolithic BMGs. Compared to quasi-static nanoindentation, DMM resolves elastic property variations (e.g. in a multiphase material) with substantially higher spatial resolution due to the smaller volumes of material that are probed. During the mapping operation, a sinusoidal load function is applied to the material of interest by the indenter tip, and instead of measuring the elastic properties at predefined positions, the tip traverses a continuous raster path over a designated area on the surface of the material. All the maps collected in the thesis work had dimensions of 3 μm x 3 μm. The set point load and load amplitude, set by the operator, must be low enough to avoid permanent deformation of the material during mapping, but also sufficiently large to achieve displacement amplitudes of 1 – 2 nm for optimum accuracy. Set point loads of 9 – 11 μN, load amplitudes of 7 – 9 μN, and a load frequency of 200 Hz were used for the Zr-based BMG specimens that were investigated.

Throughout the process, the dynamic tip displacement (d_D) and phase shift (ϕ) were continuously acquired, from which the storage and loss components of the material stiffness (*k'* and *k''*) were directly calculated according to the following:

$$k' = \frac{F_D}{d_D}\cos\phi \qquad \text{and} \qquad k'' = \frac{F_D}{d_D}\sin\phi \tag{2.10}$$

where F_D denotes the dynamic applied load. Equation(s) 2.10 are simplified expressions for the ideal case of an infinitely stiff force transducer and indenter tip; in actuality, additional terms (see Chapter 5) are necessary to account for the minor contribution of machine compliance to the measured displacements. Although metallic glasses possess time-dependent viscoelastic properties, they have generally been observed at much lower probing frequencies, on the order of 0.1 Hz [3,4]. At the substantially higher applied frequency used in this work, ϕ was determined to be negligible and therefore only the *k'* values were considered in subsequent analyses of the measured data.

Due to the low loads typically used in DMM experiments, the diamond Berkovich tip can be approximated as spherical and the storage modulus (E_r') is then easily converted from *k'* on the basis of Hertzian contact theory:

$$E_r' = \sqrt{\frac{(k')^3}{6F_D r}} \tag{2.11}$$

where *r* denotes the radius of curvature of the blunted tip, typically between 100 – 300 nm. The main concepts of the DMM technique are depicted in Figure 2.7.

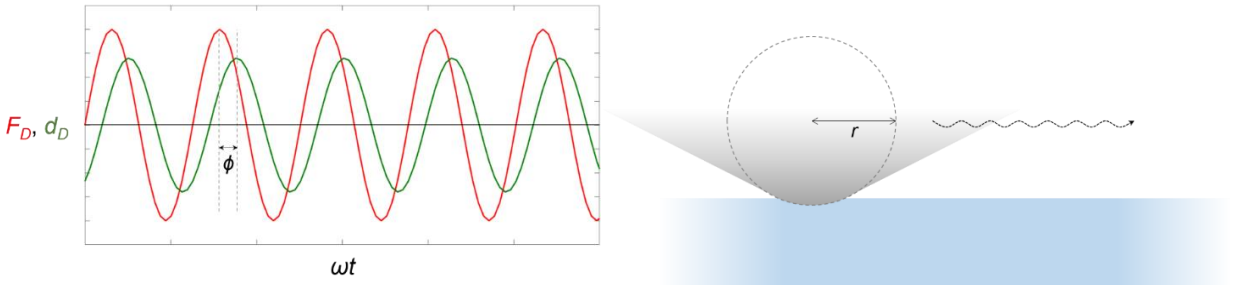

Figure 2.7 Schematic of the DMM technique. A sinusoidal load function is applied to the material of interest by the indenter tip while the tip traverses a raster pattern over the surface of the material. During mapping, the dynamic displacement (d_D) and phase shift (ϕ) are continuously measured.

Often, thermal drift may be present during modulus mapping, especially in the y-direction for horizontal raster paths, resulting in an artificial gradient of the measured properties. To minimize the undesired effect, at least 20 minutes of wait time should be allotted for the instrument motors to settle before collecting a modulus map. In the case that drift continues to persist, a function written in Matlab® (see Appendix) may be used to "clean up" the map by subtracting the artificial gradient from the raw data.

2.3 Analysis

2.3.1 Auto-Correlation Function

The spatial autocorrelation function $F_{corr}(x,y)$ was used to extract the characteristic feature dimensions from the modulus and topography images obtained by DMM. F_{corr} also highlights directional alignment of individual features and is defined mathematically as follows:

$$F_{corr}(x,y) = \iint F(x',y')F(x'+x,y'+y)\,dx'dy' \qquad (2.12)$$

Where the mapped image of either modulus or topography is denoted by the spatially-varying function $F(x',y')$. Note, however, that the actual maps are not continuous functions but 256 x 256 arrays of data, and F_{corr} takes the discretized form:

$$F_{corr}(x,y) = \sum_{y'}\sum_{x'} F(x',y')F(x'+x,y'+y) \qquad (2.13)$$

The conceptual interpretation of the autocorrelation function can be illustrated by a simple example. Consider a hypothetical property map composed of a sinusoidal distribution of values in the *x'*-direction and its corresponding autocorrelation function (Fig. 2.8a).

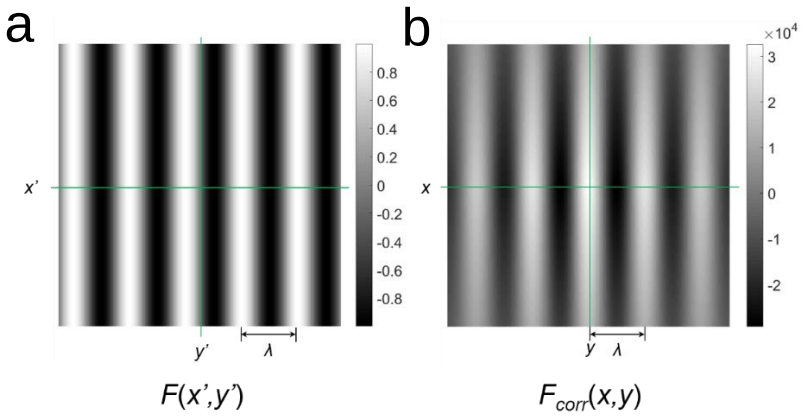

Figure 2.8 (a) A hypothetical property map with sinusoidal distribution of values. **(b)** Corresponding correlation function of the property map.

When the map is multiplied with a perfectly overlapped image of itself – $F_{corr}(0,0)$, the condition corresponds to the maximum value of the autocorrelation function. Conversely, if the overlapping image is shifted to the right or left by the characteristic feature width – $F_{corr}(\pm\lambda/2, 0)$, the images are completely out of phase and produces a minimum value of the autocorrelation function. For an arbitrary property map containing distinct features, the characteristic feature size can be approximated in the same way, by measuring the distance from the origin of the autocorrelation function to its nearest local minimum.

1. Oliver, W. & Pharr, G. An improved technique for determining hardness and elastic modulus using load and displacement sensing indentation experiments. *J. Mater. Res.* **7**, 1564–1583 (1992)
2. Oliver, W. & Pharr, G. Measurements of hardness and elastic modulus by instrumented indentation: Advances in understanding and refinements to methodology. *J. Mater. Res.* **19**, 3–20 (2004)

Chapter 3

Combinatorial Exploration of Glass Forming Ability in the Binary Cu-Zr Alloy System

This chapter is largely adapted from two papers that have been published in *Intermetallics* and *Materials and Metallurgical Transactions A*[1,2]. Both papers were written in collaboration with K.M. Flores, who edited the manuscript prior to submission and provided general guidance as the principle investigator of the work.

3.1 Introduction

Among binary alloys, bulk glass formers are rarely observed; GFA generally favors multicomponent alloys that contain three or more chemically distinct atomic species. For this reason, Cu-Zr alloys occupy a unique place among binary glass formers, having several compositions with reported critical casting thickness that exceed 1 mm. The simple composition space, combined with experimental pre-knowledge of several bulk glass formers, makes the Cu-Zr system ideal for validating the combinatorial methodology developed in this thesis work.

All previously reported efforts to fabricate compositionally-graded alloys by laser deposition (LD) utilized a multilayer, 3-dimensional fabrication procedure[3–8]. That is, the composition of the build was varied from layer to layer by changing the relative delivery rates of two different powders. However, in view of the unresolved challenges that preclude the successful manufacturing of freeform amorphous parts, the conventional "bottom-to-top" LD approach for creating compositionally-graded profiles would be unsuitable for the identification of good glass formers across a chemical gradient; alloys vitrified in one layer would likely devitrify due to repeated heating in subsequent layers. This would be especially true for the binary Cu-Zr system, where the best glass formers are marginal in comparison to many multicomponent BMGs.

Alternatively, we have developed a two-dimensional approach to fabricate single-layer specimens that feature a continuous composition gradient across the surface of the deposit.

In the first part of this work, compositionally-graded $Cu_{100-x}Zr_x$ specimens with x ranging 24 – 39 were fabricated by LD[1]. Using differential interference contrast light (DIC) microscopy, topographically featureless surface regions, which suggest the possibility of a non-crystalline structure, were observed over the range 33 – 38 at. % Cu. Electron diffraction and differential scanning calorimetry verified that these regions were primarily amorphous. By varying the laser heat input, and thereby the heating and cooling rates, we show that the most stable glass-forming composition within the explored range is $Cu_{64.7}Zr_{35.3}$, in excellent agreement with the previously reported "best" glass former that was identified from casting discrete compositions via experimental trial and error[9–11].

Building upon the success of the preliminary study, the range of exploration was extended towards Zr-rich compositions in a subsequent study[2] to identify additional GFA maxima in the binary system. Following a similar procedure as before, continuously graded specimens with composition ranging approximately 30 – 60 at. % Zr were created. Two topographically-featureless regions were identified in the extended-range specimens, corresponding to the known local maxima of GFA at $Cu_{64}Zr_{36}$ and $Cu_{50}Zr_{50}$. Incidentally, these two compositions are the most consistently reported "good" glass formers in the binary system, lending compelling validation to the combinatorial methodology.

3.2 Experimental Methods

3.2.1 Preliminary Study – Limited Composition Range (24 – 39 at. % Zr)

All LD experiments were performed with an Optomec MR-7 LENS^{TM} system. Zirconium and copper feedstock powders with respective purities of 99.2 and 99.9 at. % were simultaneously

deposited on grade 702 zirconium plates with dimensions of 3.8 cm x 3.8 cm x 0.5 cm. Prior to deposition, the substrates were surface-ground with 320 grit SiC paper and cleaned with methanol to remove surface contaminants that could adversely affect GFA. A square, single-layer deposition tool path was chosen with dimensions of 25.4 mm x 25.4 mm and containing 51 evenly-spaced parallel hatches. To achieve compositional gradation, the delivery rates of both powders were varied stepwise from hatch to hatch, 3.51 – 4.88 g/min for the copper and 3.06 - 2.36 g/min for the zirconium. The laser power and travel speed were fixed at 250 W and 8.5 mm/s, respectively. After the initial deposit, nine parallel re-melted lines spaced 2.5 mm apart were created with a 200 W laser traveling at 12.7 mm/s in the direction of the composition gradient, to facilitate thorough alloying of the two components. Finally, the alloyed lines were re-melted again with a sequence of laser powers ranging 100 – 180 W in increments of 10 W for each line. The travel speed was also increased to 16.9 mm/s. Figure 3.1 provides a schematic summary of the complete fabrication procedure.

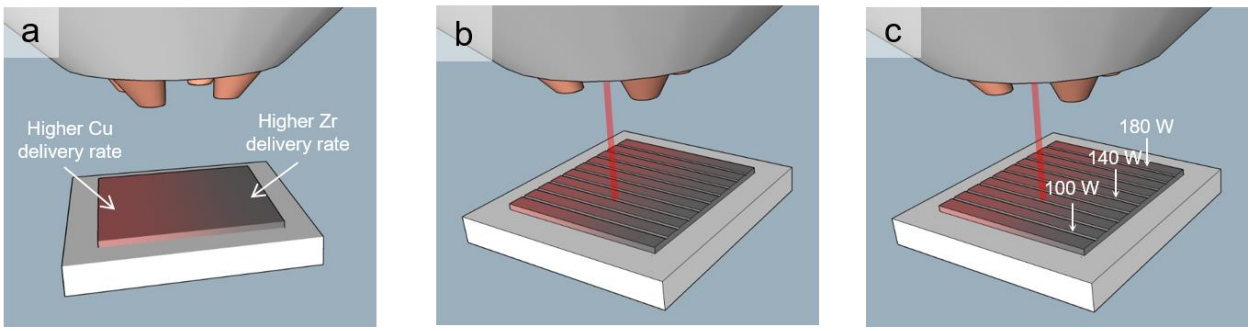

Figure 3.1 Schematic summary of fabrication procedure for compositionally-graded Cu-Zr deposits. **(a)** Initial deposition of graded layer, produced by varying the powder delivery rates gradually from one end of the deposit to the other. **(b)** Intermediate re-melting step to thoroughly mix the Cu and Zr powders across nine evenly-spaced lines. **(c)** Final re-melting step with different laser powers.

Preliminary identification of potential glass-forming compositions in the graded Cu-Zr specimens was accomplished using a Nikon light microscope equipped with a DIC prism for enhanced imaging of the specimen's surface topography[12]. This technique permits the easy differentiation between crystalline regions, which appear rough, and primarily amorphous regions, which remain smooth when left unconstrained during cooling.

Following DIC imaging, the surface of the deposit was carefully polished to a mirror finish with colloidal silica for further imaging in the scanning electron microscope (SEM), as well as compositional measurements using energy dispersive x-ray spectroscopy (EDS). To improve accuracy of measurement, the EDS results were calibrated with three Cu-Zr specimens of known composition to correct for systematic errors before further analysis of data. Electron diffraction in the transmission electron microscope (TEM) was used to confirm the amorphous structure of the material in the smooth regions previously identified by DIC microscopy. The TEM sample was prepared first by mechanically separating a segment of the topographically smooth region from the line re-melted with a 100 W laser. The isolated segment was then mechanically polished to a thickness less than 30 μm, followed by conventional ion-milling until electron transparency was achieved. An additional compositionally-graded specimen, processed in the final re-melting step with a laser power of 100 W, was prepared to investigate the glass transition and crystallization behavior of the smooth (amorphous) regions via differential scanning calorimetry (DSC); the material separated from the region of interest was heated in the DSC from room temperature through the crystallization event, at a fixed heating rate of 20 K/min.

3.2.2 Extended Composition Range (30 – 60 at. % Zr)

The powder delivery rates were adjusted to fabricate graded specimens with an extended composition range, 1.78 - 5.24 g/min for the copper and 3.91 - 2.29 g/min for the zirconium. The laser power and travel speed were unchanged from the preliminary study during both the initial

deposition and the intermediate re-melting. To encourage vitrification of weaker glass formers in the binary system, the heat input involved in the final re-melting step of the nine lines was reduced; re-melting laser power ranged from 50 to 130 W, in stepwise increments of 10 W. Repeating the same procedure, a second specimen was produced, but with the laser power in the final re-melting step ranging from 50 to 90 W in increments of 5 W for each line.

Following fabrication of the specimens, EDS was used for composition measurements on the as-deposited specimen without further polishing. Potentially amorphous regions across the composition gradient were once again visually identified by DIC microscopy. Topographically rough regions were assumed to have crystallized, resulting in the formation of surface asperities, while the smooth regions were assumed to be amorphous. The validity of these assumptions were again confirmed via electron diffraction in the TEM. Instead of conventional ion milling, a TEM foil was extracted with a focused ion beam from the line re-melted with a 75 W laser. Care was taken to minimize ion beam damage to the foil during the thinning process. To assess the stability of the amorphous region through the depth of the melt zone, the sample was sectioned through the same region and polished with colloidal silica for microstructural imaging in the SEM.

3.3 Results

3.3.1 Limited Composition Range (24 – 39 at. % Zr) Specimen

Figure 3.2 provides the EDS compositional profile of the line re-melted by a 100 W laser. The profile was continuously graded from 24 - 39 at. % Zr and is well-described by a linear trend line. The predicted compositional profile based on the powder delivery rates is also shown. The excellent agreement between the measured and predicted compositional trends confirms our ability to accurately control the compositions of graded specimens by choosing appropriate powder delivery rates.

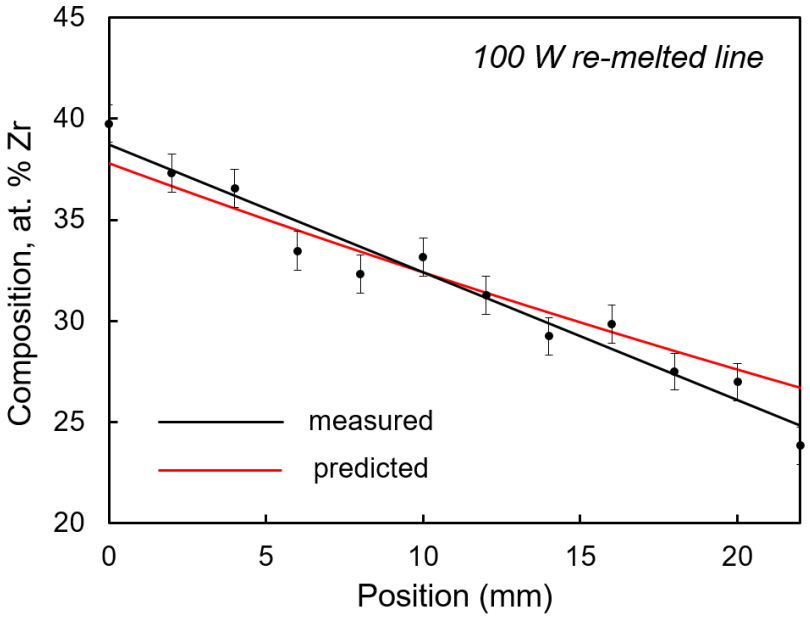

Figure 3.2 Compositional profile of a Cu-Zr deposit line re-melted using a laser power of 100 W and a travel speed of 16.9 mm/s. The measured profile is compared with the ideal profile predicted by the powder feed rates, assuming perfect deposition efficiency of both Cu and Zr powders.

Figure 3.3a shows a DIC image of a possible amorphous segment within the line re-melted by the 100 W laser. The surface of the segment is topographically smooth with very few identifiable surface features. SEM micrographs of the polished specimen obtained from the middle of the segment also appear featureless (Fig. 3.3b), as expected from the uniform microstructure of metallic glass. In contrast to the smooth segment, the uneven topography of the material to the immediate left of the segment clearly indicates the presence of crystals in this region (Figure 3.3c). A SEM micrograph obtained near the end of the smooth segment displayed crystallites of an unidentified phase embedded within a featureless matrix, suggesting a semi-amorphous transition region between fully vitrified and fully crystallized material (Figure 3.3d).

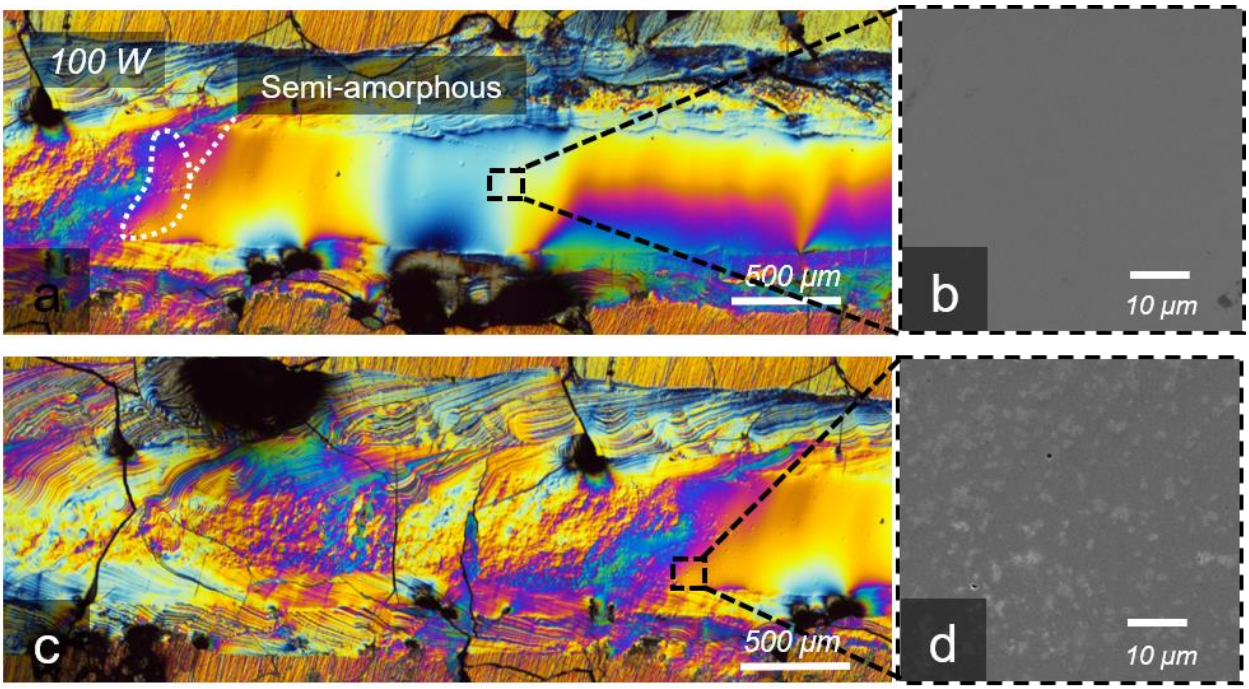

Figure 3.3 (a) DIC image of a topographically smooth segment of the compositionally graded Cu-Zr deposit and **(b)** the corresponding secondary electron SEM image of the microstructure, from a line re-melted using a laser power of 100 W and travel speed of 16.9 mm/s. The Cu content increases from left to right. **(c)** DIC image of crystalline material adjacent to the smooth segment. **(d)** The SEM micrograph recorded from the semi-amorphous region shows crystallites embedded within a featureless matrix.

Figure 3.4 is a DIC image of a complete specimen, with the re-melted lines labeled according to the laser power used in the final processing step. The topographically smooth segment observed in each line has been boxed in for clarity; interestingly, the width of the segment deceases with increasing laser power. Due to the presence of the semi-amorphous transition regions, there is a certain degree of ambiguity with regards to the boundaries of the amorphous segments; as an approximation, the endpoints are chosen as the positions where the smooth material is no longer visually detectable.

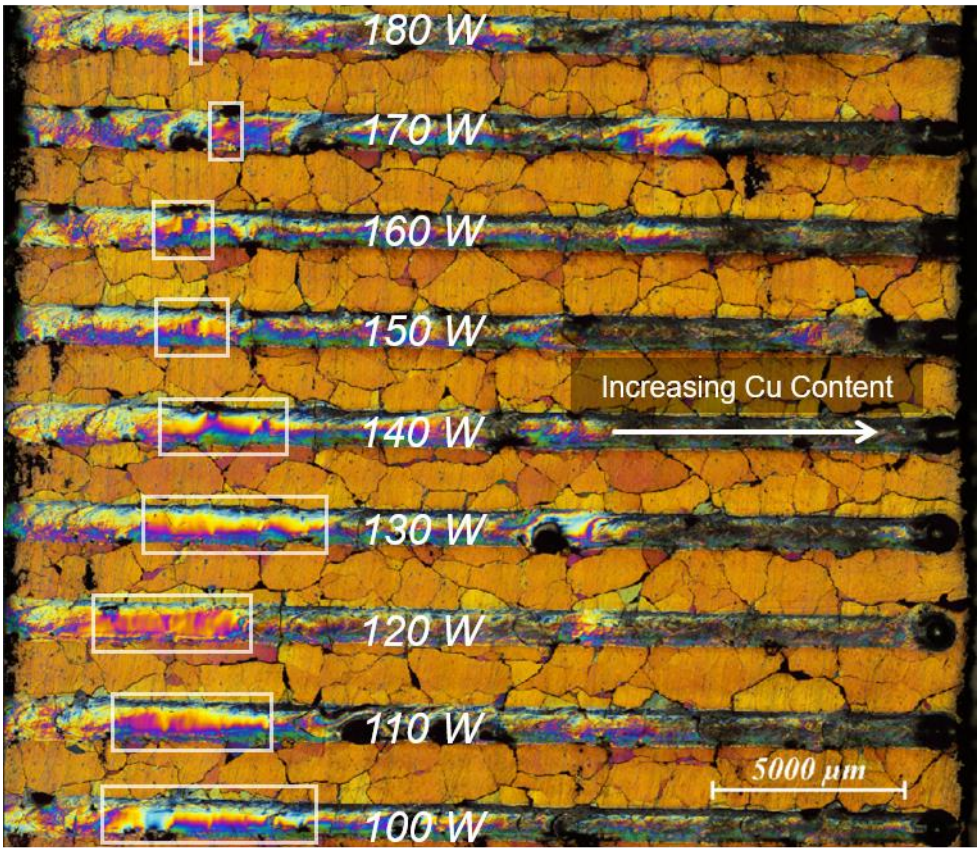

Figure 3.4 DIC image of a graded Cu-Zr deposit, showing the re-melted lines created with different laser powers. The topographically smooth segment in each re-melted line is boxed in for clarity, demonstrating a width that decreases with increasing laser power.

Figure 3.5 shows the DSC heating trace for the segment of the featureless material that was mechanically separated from the line re-melted by a 100 W laser. Although the glass transition was weak, the curve displayed a prominent exothermic crystallization peak, suggesting that the topographically featureless segments contained a significant volume fraction of amorphous material. T_g was 755 K, and the onset temperature of the crystallization peak (T_x) was 780 K, consistent with the T_g and T_x of the best reported glass former, $Cu_{64.5}Zr_{35.5}$ [10]. TEM diffraction produced a diffuse ring pattern, confirming that the topographically featureless segments in the re-melted lines were in fact amorphous.

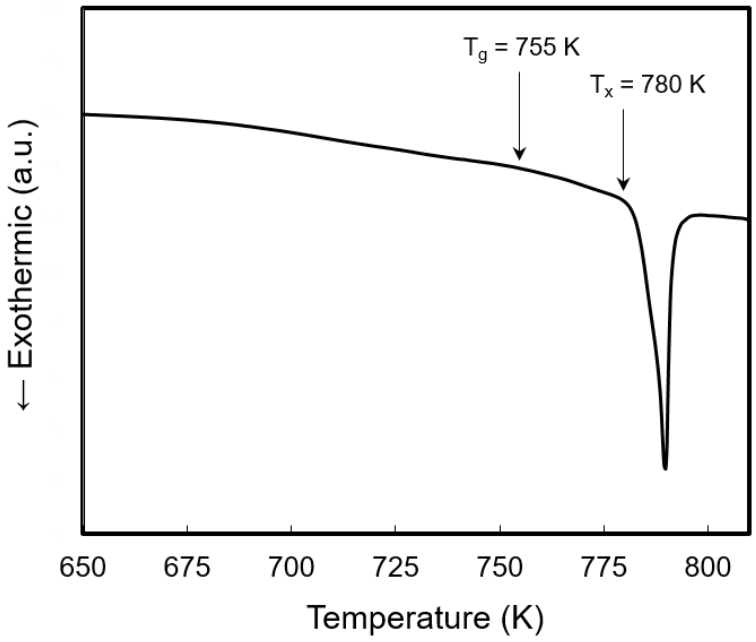

Figure 3.5 DSC heating trace of the topographically smooth segment mechanically separated from a re-melted line created with a 100 W laser and travel speed of 16.9 mm/s. DSC data was obtained at a heating rate of 20 K/min.

3.3.2 Extended Composition Range (30 – 60 at. % Zr) Specimens

Figure 3.6 shows the EDS compositional profile of a graded specimen along a re-melted line processed by a 65 W laser. The continuous composition gradient agreed well with the predicted trend calculated according to the powder delivery rates for compositions greater than 36 at. % Zr. Below 36 at. % Zr, the measured profile became discontinuous and was richer in Zr than the predicted trend line. It is unclear why the profile deviated from the calculated trend for this specimen; prior work indicated that a smoothly varying profile should be attainable over the entire composition range. For the remainder of this work, we use the measured compositions at positions of interest, rather than the predicted composition. The minimum measured Zr concentration was 30 at. %.

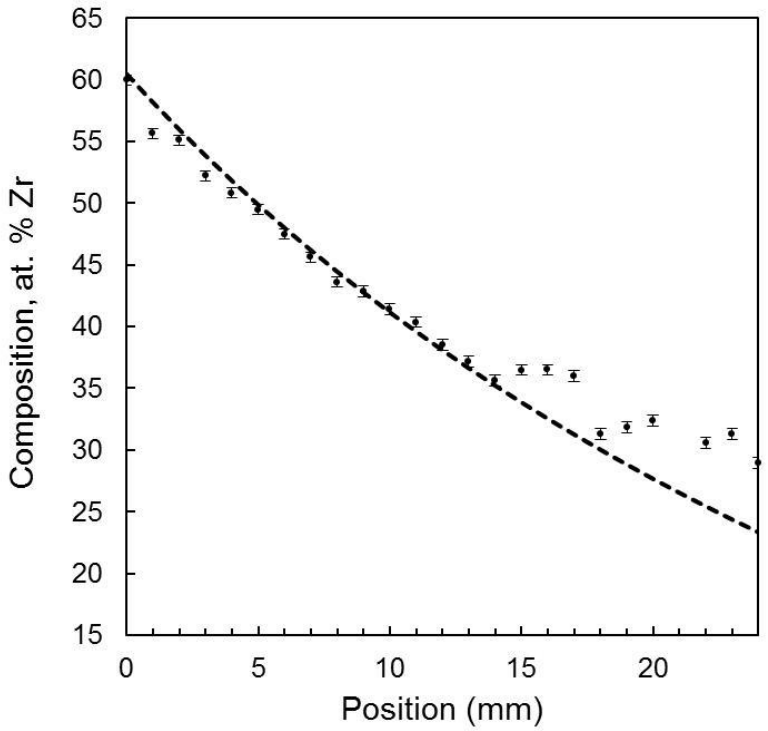

Figure 3.6 The compositional profile of a continuously graded Cu-Zr specimen, measured by EDS. For comparison, the dashed line is the trend predicted by the powder delivery rates.

Two topographically smooth segments were observed in most of the re-melted lines of both specimens (Fig. 3.7), near the compositions 36 at. % Zr and 50 at. % Zr. Based on the results from the earlier work, which covered a narrower composition range of 24 – 39 at. % Zr, the smooth segments were suspected to be amorphous and represent two separate ranges of composition with comparatively higher GFA within the binary system. Similar to the earlier study, the widths of the segments were found to generally narrow with increasing laser power.

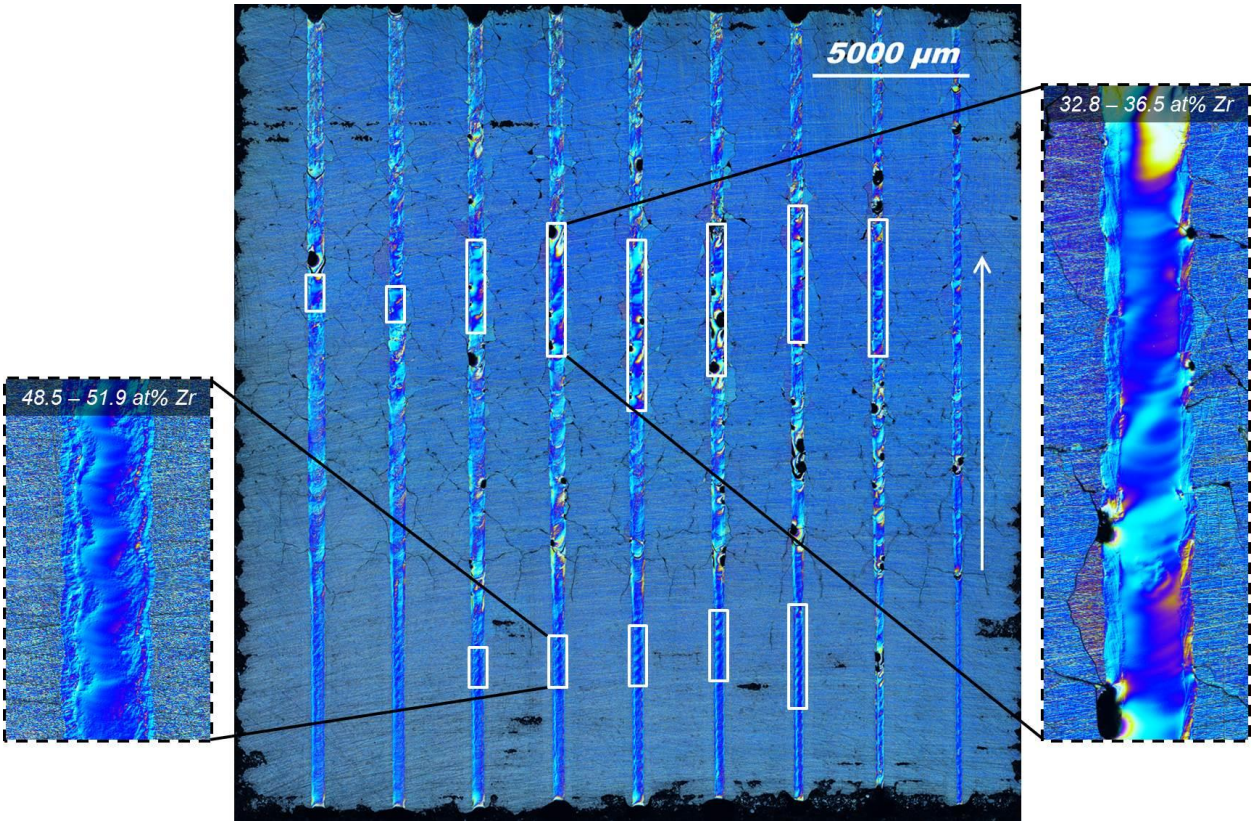

Figure 3.7 DIC image of a complete graded Cu-Zr deposit (middle), and magnified views of two topographically smooth segments (left and right) found in a line re-melted by a 75 W laser. The white arrow indicates the direction of increasing Cu content. The laser power used for each re-melted line decreases from left to right. Topographically smooth regions within each line, assumed to be amorphous, are outlined with white boxes. The composition ranges of the amorphous segments narrow with increasing heat input.

Note that the smooth segments also appeared to transition into distinctly different crystalline microstructures at their two ends (Fig. 3.8). For example, the crystalline microstructure observed at a Zr concentration of less than 33.7 at. % for a 70 W re-melt pass, shown at the top of Figure 3.8a, exhibited a rough surface terrain without visual evidence of individual crystallites or grains. In comparison, the crystalline region formed at a Zr concentration exceeding 38.0 at. %, shown at the bottom of Figure 3.8b, displayed an apparent microstructure composed of clusters of spherical crystallites.

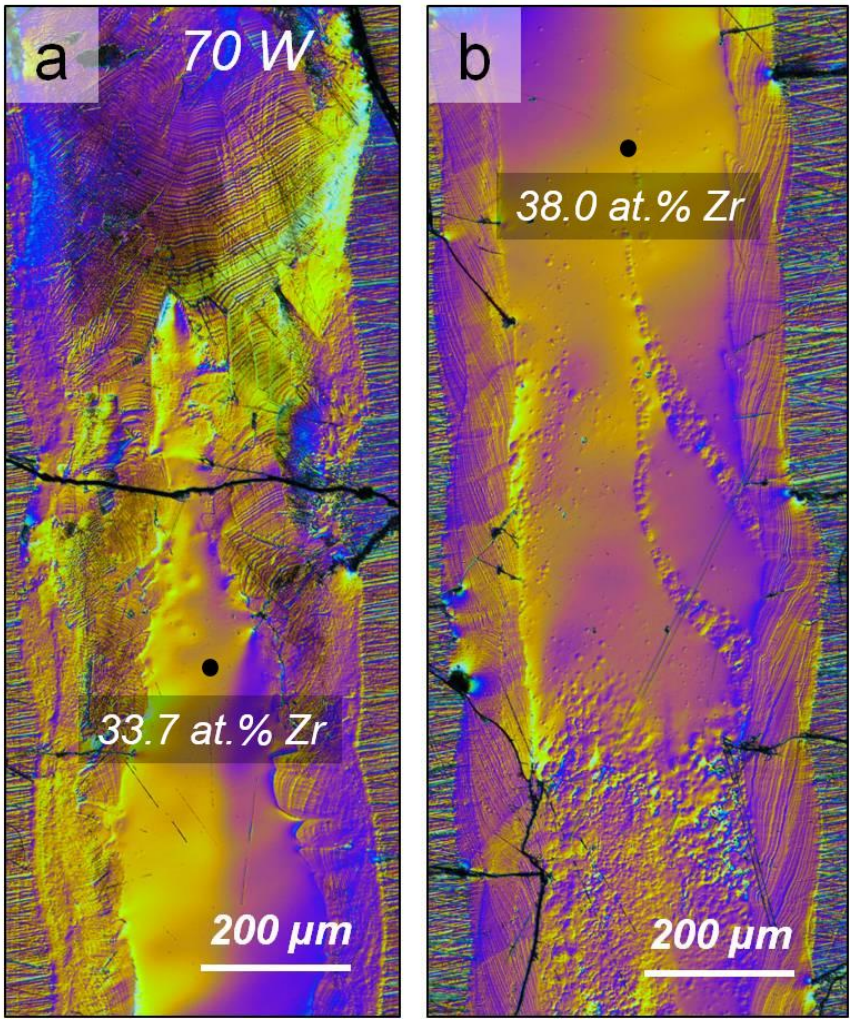

Figure 3.8 DIC images of the microstructure differences occurring at the boundaries of a smooth (amorphous) segment in a line re-melted by a 70 W laser. **(a)** Crystals at the boundary at 33.7 at% Zr exhibits a rough topography without visual evidence of individual crystallites or grains. **(b)** The boundary at 38 at. % Zr exhibits a microstructure composed of spherical crystallites that are clustered together.

Electron diffraction confirmed that the smooth segment on the copper-rich side of the specimen was fully amorphous (Fig. 3.9a). SEM micrographs of the cross section through the segment showed a featureless melt zone surrounded by a fine, dendritic microstructure (Fig. 3.9b). Fig. 3.9c shows the dendritic microstructure ending abruptly at the edge of the amorphous melt zone, without penetrating into the glass.

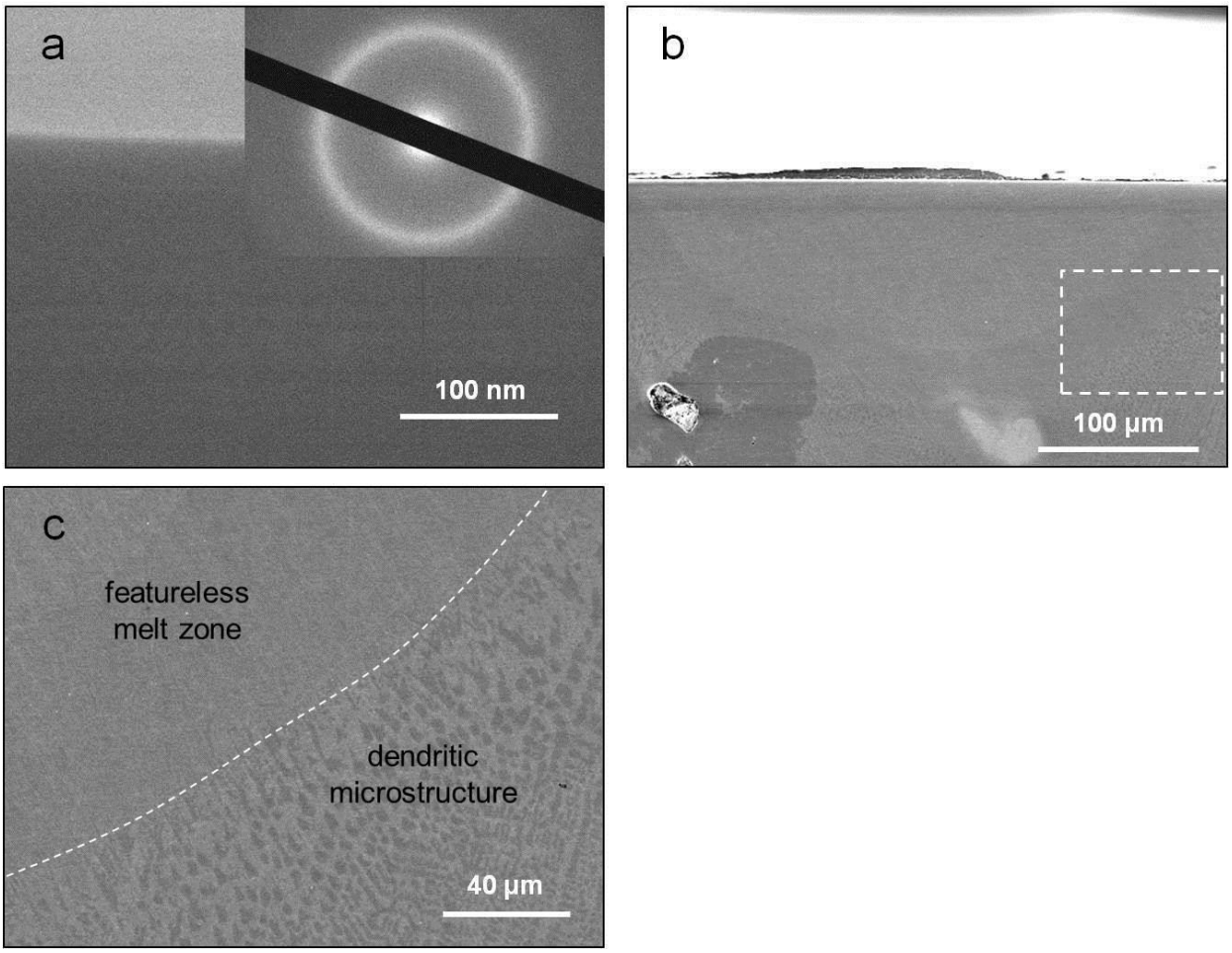

Figure 3.9 (a) Bright field TEM micrograph and corresponding diffraction pattern of a foil extracted from a topographically smooth segment (32.8 - 36.5 at% Zr) in the line re-melted by a 75 W laser. **(b)** Cross section SEM micrograph through the middle of the same segment, showing a semicircular melt zone. **(c)** Magnified view of the boxed region in (b), showing a heat affected zone consisting of a fine dendritic microstructure surrounding the featureless melt zone.

3.4 Discussion

A robust combinatorial strategy for identifying new metallic glass forming alloys requires the ability to fabricate graded composition libraries as well as a high-throughput means to distinguish potential glassy alloys from crystalline material. Although diffraction techniques are necessary to "definitively" determine whether the atomic structure is crystalline or amorphous,

these techniques typically involve time-consuming specimen preparation and serial analysis of many compositions. Benefits gained from combinatorial synthesis would be offset by the inability of diffraction to rapidly screen for vitrified material within a composition library.

Following the work of Ding *et al.*, who used a change in surface contrast of an unconstrained liquid to identify the onset of crystallization in magnetron co-sputtered thin film libraries[13], we use DIC optical microscopy as a high-throughput screening method for identifying potential vitrified regions within the compositionally-graded deposit. Unlike cast specimens, the surfaces of the re-melted lines in the laser-deposited specimens are unconstrained during quenching of the melt pool, allowing crystalline features develop into topographically distinct surface asperities. Reflected light DIC microscopy provides enhanced topographical (height) contrast, enabling easy detection of crystallites. In contrast to the topographically rough regions, we argue that segments of the re-melt lines which remain smooth indicates a high probability of having bypassed crystallization to vitrify into an amorphous solid. Again, while the final verdict of amorphicity must be confirmed via diffraction, DIC microscopy provides a rapid screening technique to exclude definite non-starters and identify candidate alloys for further characterization.

In addition to the topographically smooth regions, the topographical features of the rough regions are potential indicators of different microstructures produced from the nucleation of different primary phases. As shown in Figure 3.8, the apparent microstructures that were consistently observed at the two ends of a Cu-rich amorphous segment were distinctly different, consistent with the recently proposed hypothesis that optimum glass formers within an alloy system reside at compositions where the nucleation of competing primary phases intersect [13]. Although beyond the scope of the present work, this hypothesis could potentially be tested in the

continuously graded specimens by identifying the crystalline phases that are present at the boundaries of the smooth segments.

As mentioned in the results, the compositional widths of the amorphous segments were repeatedly found to narrow with increasing laser power, or more accurately, the laser heat input (Fig. 3.4 and 3.7). The instantaneous heat input per unit area to the melt pool is given by $\lambda = \frac{P}{vD}$, where *P*, *v*, and *D* denote the absorbed laser power, beam travel velocity, and laser beam diameter, respectively. *D* was assumed to be independent of laser power and approximated as 1 mm. The narrowing of the amorphous regions in the graded specimen can be explained by the general effect of λ on an alloy's ability to vitrify. Sun and Flores carried out laser deposition experiments with a Zr-based BMG powder on amorphous substrates and reported a dependence of glass formation on λ [14,15]. It was specifically observed that decreasing λ below a threshold value by fixing the laser power and increasing the travel speed nearly eliminated crystallinity in the heat affected zone. Chen *et al.* performed laser surface melting experiments with $Cu_{60}Zr_{30}Ti_{10}$ substrates and reported the same effect of travel speed on the ability of the local melt pool to fully vitrify [16]. The authors additionally demonstrated that for a fixed travel speed, increasing λ above a threshold value by increasing the applied laser power resulted in noticeable crystallinity. The results of these prior studies suggest the existence of a maximum instantaneous heat input λ_{max} for a given alloy, above which the thermal burden becomes too large to suppress crystallization.

We propose that λ_{max} is analogous to GFA, which is most often described in terms of a critical casting thickness. In casting experiments, the thermal load scales with the thickness of the mold, with thicker molds resulting in lower average cooling rates. Similarly, in laser processing, the average cooling rate experienced by the melt pool between the liquidus and glass transition temperature should diminish with increasing λ.

Assuming that GFA for a particular alloy system is a continuous function of composition[17], the amorphous segments observed in the continuously graded specimens correspond to local maxima in the GFA landscape of binary Cu-Zr alloys. The compositions at the boundaries of the segments represent alloys with the lowest GFA within the segment, on the cusp of being able to vitrify under the applied thermal load. In principle, when the deposit is re-melted with increasing values of laser power or λ, the compositional range of the amorphous segments should narrow until only the best glass-forming composition, possessing the highest λ_{max}, could vitrify.

To test our hypothesis, the boundary compositions of the amorphous segments for each re-melted line in the graded specimens (both limited- and extended-range) have been plotted versus the applied λ (Fig. 3.10). For improved statistical precision, each data point represents the average of at least five compositional measurements obtained at the same position. Linear trend lines fit to the upper and lower bounds of the amorphous segments describe the gradual narrowing of glass forming compositions towards local maxima in GFA. The "best" glass formers within the range of compositions explored in this work, $Cu_{64.7}Zr_{35.3}$ and $Cu_{50.2}Zr_{49.8}$, were deduced by the intersection of the trend lines.

Comparing the "limited-range" and "extended-range" data sets, the upper bound compositions of the Cu-rich glass forming segments of the two extended-range specimens showed significant scatter, while the lower bound compositions followed a trend consistent with the limited-range study. The compositional widths of the amorphous segments processed with the lower laser powers were also substantially narrower, despite a lower applied heat input. The unexpected discrepancy may be due to incomplete melting of the crystalline phase(s) on the upper bound side of the amorphous range due to the low λ. Although a lower heat input would result in a higher average cooling rate within the melt zone, the presence of residual nuclei from incomplete

melting could offset the benefit gained from increased cooling rates. Note that the continuation in the trend on the upper bound side across the full range of heat inputs further suggests that a different competing crystalline phase, having a lower melting temperature, forms on the lower bound side of this glass forming region.

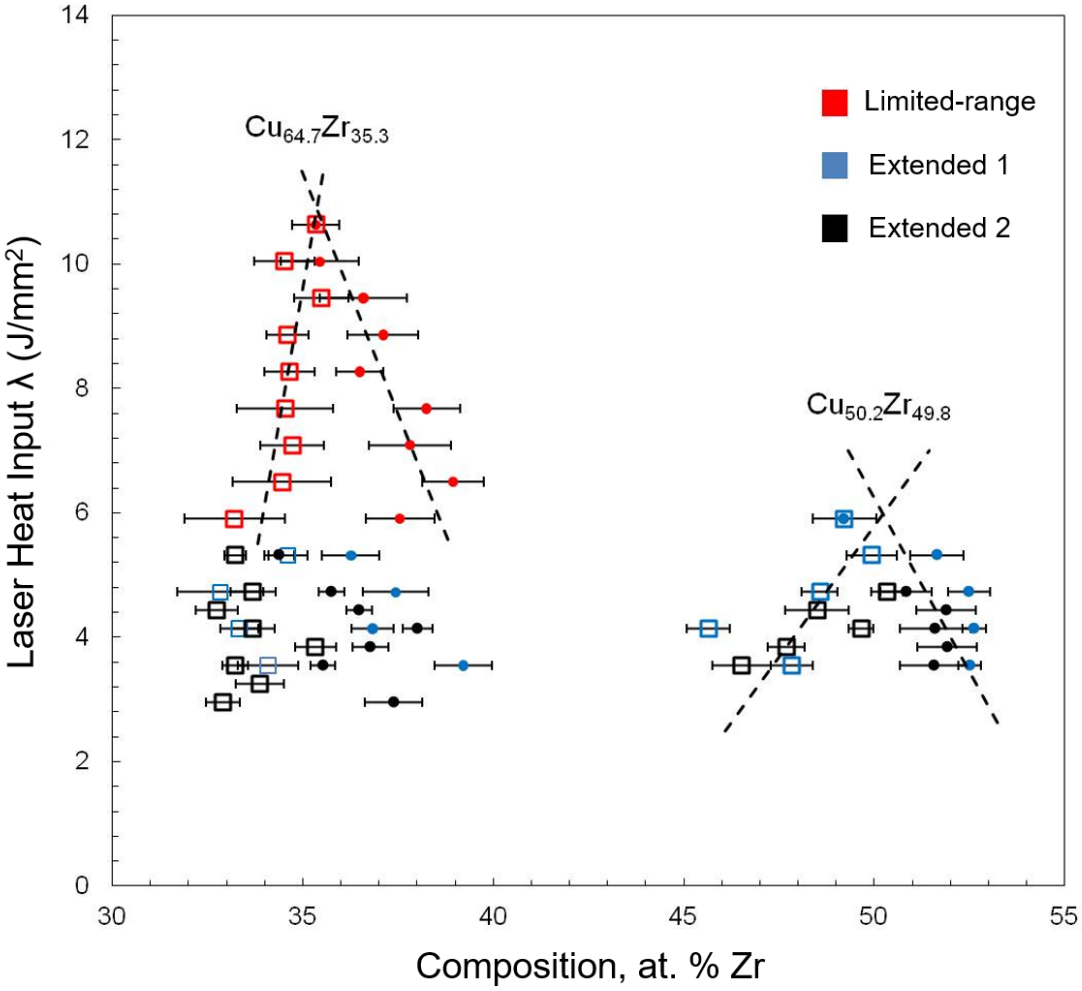

Figure 3.10 The composition at the boundaries of each amorphous segment plotted against λ, the local heat input from the laser. The square and circle symbols correspond to the lower and upper bound Zr concentrations, respectively, of the smooth segments. As λ increases, the compositional range of amorphous material narrows until only the best glass former is able to vitrify. The analysis identifies two local maxima in the GFA landscape of Cu-Zr alloys at $Cu_{64.7}Zr_{35.3}$ and $Cu_{50.2}Zr_{49.8}$.

The second local maximum in GFA was identified at $Cu_{50.2}Zr_{49.8}$, noticeably with a lower λ_{max} compared to the Cu-rich peak composition, $Cu_{64.7}Zr_{35.3}$. The data suggests this glass forming

range would not be observable at the higher λ values used in the limited-range study, further illustrating the potential tradeoff between the high λ required for complete melting and the low λ required for fast cooling.

Another interesting difference between the two glass-forming regions is apparent when comparing the steepness of the fitted trend lines in Figure 3.10. The steeper descent of λ_{max} away from $Cu_{64.7}Zr_{35.3}$ suggests that GFA in the Cu-rich glass-forming range is more sensitive to deviations from the ideal composition. Johnson *et al.* carefully mapped critical casting thicknesses in the compositional vicinity of various multicomponent BMGs and also observed steep, exponential rises in GFA surrounding a local maximum. The authors argued that the exponential rise in GFA towards a peak value is directly associated with the nucleation pathway for the competing crystalline phase[17]; according to the interpretation of their collected data, asymmetry of the peaks reflect a crossover from one nucleation pathway to another. We duly note that in our GFA analysis, the Cu-rich "peak" is also asymmetric, with the lower bound trend line being steeper than the upper bound line. Furthermore, Li *et al.* carried out comprehensive exploration of GFA in the binary Cu-Zr system, and similar asymmetry of the peak centered at $Cu_{64}Zr_{36}$ was present in the plot of critical casting thickness versus composition[9]. These observations offer strong support for the hypothesis mentioned earlier that the best glass formers are found at the compositional crossover from one primary crystalline phase to another.

In contrast to the present work, casting studies of discrete compositions in the Cu-Zr system have identified four compositions with high GFA: $Cu_{64}Zr_{36}$, $Cu_{55}Zr_{45}$, $Cu_{50}Zr_{50}$ [9,11] and the eutectic composition, $Cu_{46}Zr_{54}$ [18,19]. Although the combinatorial study presented here spans this same composition range, we do not observe glass formation at $Cu_{55}Zr_{45}$ or $Cu_{46}Zr_{54}$. Factors responsible for the lack of glass formation at these two compositions in the laser deposited specimens remain

unclear, but it is noteworthy that the high GFA of both missing compositions are not consistently reported by previous comprehensive studies of glass formation in the binary system. Li et al.'s study failed to report $Cu_{46}Zr_{54}$ as a good glass former [9], but the same composition had been reported by Johnson's group as an excellent glass former with a casting thickness up to 2 mm [18,19]. Similarly, $Cu_{55}Zr_{45}$ was reported by Li *et al.* but was not recognized in Johnson's studies. Kwon *et al.* [20] also investigated glass formation in the binary Cu-Zr system by casting a series of compositions spanning a range of 30 - 60 at% Zr. The authors reported that fully amorphous rods with a 2 mm diameter were obtained at 36 at% Zr and between the range of 50 - 53 at% Zr, agreeing well with the results of our present study.

We suspect that oxygen may negatively impact GFA and preclude glass formation at $Cu_{55}Zr_{45}$ and $Cu_{46}Zr_{54}$ in our graded specimens, as well as contribute to the disagreement in the literature. Oxygen impurity has been shown to substantially reduce the extent of undercooling attainable in otherwise chemically uncontaminated BMGs [21]. Owing to the large surface area to volume ratio of powder materials, the native oxide layer on the powders would inevitably introduce a nontrivial amount of oxygen into the deposits. While it may thus be difficult to avoid oxygen impurity in laser deposited specimens, the high oxygen content in the deposits biases this technique towards the discovery of alloys that possess exceptional resistance to the effects of oxygen contamination. For example, the two alloys identified in our combinatorial studies, $Cu_{64.7}Zr_{35.3}$ and $Cu_{50.2}Zr_{49.8}$, are likely the most chemically resilient glass formers in the binary system. This screening capability would be particularly beneficial for the industrial manufacturing of BMG products, where usage of high-purity elemental materials is often not an economically feasible option.

3.5 Conclusions

We have developed a new experimental methodology that facilitates the rapid identification of good glass formers in an alloy system. Continuously graded Cu-Zr specimens covering a wide range of compositions were fabricated by direct laser deposition. A correlation was found between the surface topography and atomic structure of the laser re-melted deposit. Using differential interference contrast microscopy, vitrified regions appeared topographically smooth and were found to occupy two continuous ranges of compositions. By processing the graded specimens with gradually increasing laser heat input, two compositions corresponding to local maxima in the GFA landscape were deduced, $Cu_{64.7}Zr_{35.3}$ and $Cu_{50.2}Zr_{49.8}$. These identified peaks agree very well with previous results obtained from casting individual specimens of discrete composition. Future studies will expand the combinatorial methodology to investigate glass formation in multicomponent alloys containing three or more elements.

3.6 References

1. Tsai, P. & Flores, K. M. A combinatorial strategy for metallic glass design via laser deposition. *Intermetallics* **55,** 162–166 (2014).
2. Tsai, P. & Flores, K. A Laser Deposition Strategy for the Efficient Identification of Glass-Forming Alloys. *Metall. Mater. Trans. A* **46,** 3876–3882 (2015).
3. Collins, P. C., Banerjee, R., Banerjee, S. & Fraser, H. L. Laser deposition of compositionally graded titanium-vanadium and titanium-molybdenum alloys. *Mater. Sci. Eng. A* **352,** 118–128 (2003).
4. Banerjee, R., Collins, P. C., Bhattacharyya, D., Banerjee, S. & Fraser, H. L. Microstructural evolution in laser deposited compositionally graded titanium-vanadium alloys. *Acta Mater.* **51,** 3277–3292 (2003).
5. Han, S. M. *et al.* Combinatorial studies of mechanical properties of Ti-Al thin films using nanoindentation. *Acta Mater.* **53,** 2059–2067 (2005).
6. Carvalho, P. M. *et al.* Automated workstation for variable composition laser cladding - its use for rapid alloy scanning. *Surf. Coatings Technol.* **72,** 62–70 (1995).

7. Vilar, R. & Colaco, R. Laser-assisted combinatorial methods for rapid design of wear resistant iron alloys. *Surf. Coatings Technol.* **203,** 2878–2885 (2009).

8. Hofmann, D. C. *et al.* Developing Gradient Metal Alloys through Radial Deposition Additive Manufacturing. *Sci. Rep.* **4,** 5357 (2014).

9. Li, A. Y., Guo, Q., Kalb, J. A., Thompson, C. V & Li, Y. Matching Glass-Forming Ability with the Density of the Amorphous Phase. *Science* **322,** 1816–1819 (2008).

10. Wang, D. *et al.* Bulk metallic glass formation in the binary Cu–Zr system. *Appl. Phys. Lett.* **84,** 4029–4031 (2004).

11. Xu, D., Lohwongwatana, B., Duan, G., Johnson, W. L. & Garland, C. Bulk metallic glass formation in binary Cu-rich alloy series – Cu100−xZrx (x=34, 36, 38.2, 40 at.%) and mechanical properties of bulk Cu64Zr36 glass. *Acta Mater.* **52,** 2621–2624 (2004).

12. Ausserre, D. & Valignat, M. P. Wide-Field Optical Imaging of Surface Nanostructures. *Nano Lett.* **6,** 1384–1388 (2006).

13. Ding, S., Gregoire, J., Vlassak, J. J. & Schroers, J. Solidification of Au-Cu-Si alloys investigated by a combinatorial approach. *J. Appl. Phys.* **111,** 114901:1–6 (2012).

14. Sun, H. & Flores, K. M. Laser deposition of a Cu-based metallic glass powder on a Zr-based glass substrate. *J. Mater. Res.* **23,** 2692–2703 (2008).

15. Sun, H. & Flores, K. M. Microstructural Analysis of a Laser-Processed Zr-Based Bulk Metallic Glass. *Metall. Mater. Trans. A* **41,** 1752–1757 (2010).

16. Chen, B. Q. *et al.* Surface vitrification of alloys by laser surface treatment. *J. Alloys Compd.* **511,** 215–220 (2012).

17. Na, J. H. *et al.* Compositional landscape for glass formation in metal alloys. *Proc. Natl. Acad. Sci.* **111,** 9031–6 (2014).

18. Hofmann, D. C., Duan, G. & Johnson, W. L. TEM study of structural evolution in a copper mold cast Cu46Zr54 BMG. *Scr. Mater.* **54,** 1117–1122 (2005).

19. Duan, G. *et al.* Molecular dynamics study of the binary Cu46Zr54 metallic glass motivated by experiments: Glass formation and atomic-level structure. *Phys. Rev. B* **71,** 224208:1–9 (2005).

20. Kwon, O., Kim, Y., Kim, K., Lee, Y. & Fleury, E. Formation of amorphous phase in the binary Cu-Zr alloy system. *Met. Mater. Int.* **12,** 207–212 (2006).

21. Lin, X. H., Johnson, W. L. & Rhim, W. K. Effect of Oxygen Impurity on Crystallization of an Undercooled Bulk Glass Forming Zr-Ti-Cu-Ni-Al Alloy. *Mater. Trans. JIM* **38,** 473–477 (1997).

Chapter 4

High-throughput Exploration of Glass-forming Alloys and their Mechanical Properties in the Cu-Zr-Ti Ternary System

This chapter is largely adapted from a paper that has been published in *Acta Materialia*[1] and written in collaboration with K.M. Flores, who edited the manuscript prior to submission and provided general guidance as the principle investigator of the work.

4.1 Introduction

Over the past century, engineering alloys have become increasingly sophisticated in order to meet challenging performance specifications required by cutting-edge technology. The most advanced structural alloys of today are multicomponent, typically comprising a dominant solvent species and at least two or more minor constituents. For example, typical Ni-based superalloys used widely in the aerospace industry could contain more than ten alloying components to achieve complex microstructures that retain the alloys' mechanical integrity at high operating temperatures [2,3]. A promising class of multicomponent alloys, and the subject of the present study, is bulk metallic glasses (BMGs). BMGs are characterized by an amorphous atomic structure devoid of long-range translational symmetry, resulting in a rare combination of properties that are unattainable in even the most advanced crystalline alloys. These include near-theoretical strengths, large elastic strain limits, and the unique ability among metallic materials to undergo thermoplastic processing [4,5]. The salient commonality among these example classes of advanced engineering alloys is the vast composition space they occupy, motivating the development of combinatorial synthesis methods that could facilitate the high-throughput discovery of new alloys

with optimized properties [6–10]. In this paper, we describe a novel strategy for correlating glass forming ability and other properties with composition in multicomponent BMGs.

Since the discovery of BMGs, intense focus has been directed towards understanding the origins of glass forming ability (GFA) and the necessary criteria for identifying alloy compositions with high GFA. As a result, a number of empirical rules, temperature-based metrics, and structural models have been developed for predicting optimum glass-forming compositions [11–19]. Despite the value that various guidelines and predictive parameters have contributed to the present understanding of GFA, none have demonstrated consistent reliability as standalone predictors of GFA *a priori* [20–22]. Johnson *et al.* recently showed that only two parameters, the reduced glass transition temperature (T_{rg}) and the dynamic fragility of the supercooled liquid, are necessary for quantifying GFA accurately [23]. However, these parameters are acquired from experimental measurements performed on the glass itself and consequently do not enable true predictive capability. Without a robust means of prediction, the exploration of glass formation in an alloy system still relies heavily on experimental trial and error methods.

Conventional approaches for investigating the compositional landscape of GFA in multicomponent systems typically follow a serial, one-at-a-time experimental paradigm, where discrete compositions are synthesized and their amorphous structure verified by various diffraction techniques. Despite the success of serial methods in discovering many notable BMG alloys, the sensitivity of GFA to chemical composition [24,25] necessitates fabrication of an impractically large quantity of individual specimens in order to systematically probe the vast composition space occupied by multicomponent alloys. As a result, many alloy systems containing potential glass formers remain either only partially investigated or entirely unexplored.

In recent years, vapor deposition techniques have emerged as a combinatorial method to explore glass formation in complex metallic systems more efficiently [26–33]. Most notably, Ding *et al.* reported using magnetron co-sputtering to deposit ternary Au-Cu-Si and Mg-Cu-Y composition libraries [31,32]. By applying a thermoplastic blow molding technique to an amorphous thin-film library, the authors were able to map out the compositional landscape of thermoplastic formability and successfully identify the compositions with optimized processability. However, it is important to note that the mechanism of vitrification from the vapor phase may produce structures and glass properties that are different from glasses synthesized by liquid quenching [34,35]. The influence of the substrate in thin-film libraries may also preclude accurate determination of mechanical properties during instrumented indentation experiments.

Alternatively, we have developed a novel experimental methodology using laser additive manufacturing as a high-throughput synthesis tool to accelerate the discovery of new BMGs. In our previous studies, compositionally graded specimens of the binary Cu-Zr alloys were fabricated and the optimum glass formers within the binary system were accurately identified [36,37]. In the present work, we demonstrate the ability to systematically investigate GFA across the substantially larger composition space of a ternary system. Alongside this effort, we demonstrate a fabrication scheme that, when combined with instrumented nanoindentation, enables high-throughput characterization of mechanical properties across large regions in composition space.

4.2 Experimental Methods

4.2.1 Continuously-graded libraries for GFA optimization

All composition libraries reported in this paper were fabricated with an Optomec MR-7 LENS^{TM} system. The substrates were grade 702 zirconium ground with 320 grit SiC paper and

then cleaned with methanol to remove surface contaminants. The elemental powders used in the experiments had minimum purities of 99.9, 99.2, and 99.2 at. % for Cu, Zr, and Ti respectively.

Three 25.4 mm x 25.4 mm compositional libraries were constructed using a three layer sequential fabrication scheme with intermediate re-melting steps to fully incorporate the deposited powders. To preserve the as-deposited surface topography, the fabricated libraries were not polished following fabrication. Figure 4.1 provides a schematic illustration of the overall experimental concept. Each elemental powder layer was deposited using a constant laser power and powder delivery rate, while the travel speed of the substrate relative to the laser and powder source was varied continuously across the specimen (8.47-29.63 mm/s) to achieve the desired composition gradient. For each library, the Zr was deposited first using a 250 W laser with the travel speed decreasing in the +x direction (in the coordinate frame of the substrate), resulting in an increasing amount of powder deposited in the +x direction. The Cu was deposited in the second layer using a 250 W laser with the travel speed decreasing in the -x direction, in the direction opposite to the Zr gradient. To facilitate thorough alloying of the Cu and Zr, a series of parallel, evenly spaced lines oriented in the y direction were then re-melted with a 200 W laser at a travel speed of 12.7 mm/s, such that each re-melted line had a fixed Cu:Zr ratio. Ti was then deposited in the third layer, using a 150 W laser with the travel speed decreasing in the +y direction, resulting in a Ti gradient perpendicular to the Cu-Zr gradient. The re-melted lines were melted again to thoroughly incorporate the Ti. Thus, the Cu:Zr molar ratio nominally remained fixed within a re-melted line while the Ti content increased along the length of the line, producing a collection of tie lines in the ternary composition map. To investigate the effect of processing conditions on the compositional extent of glass formation, the final re-melting step was performed at different laser powers (200, 240, and 280 W) for the three libraries. An individual library required no more than

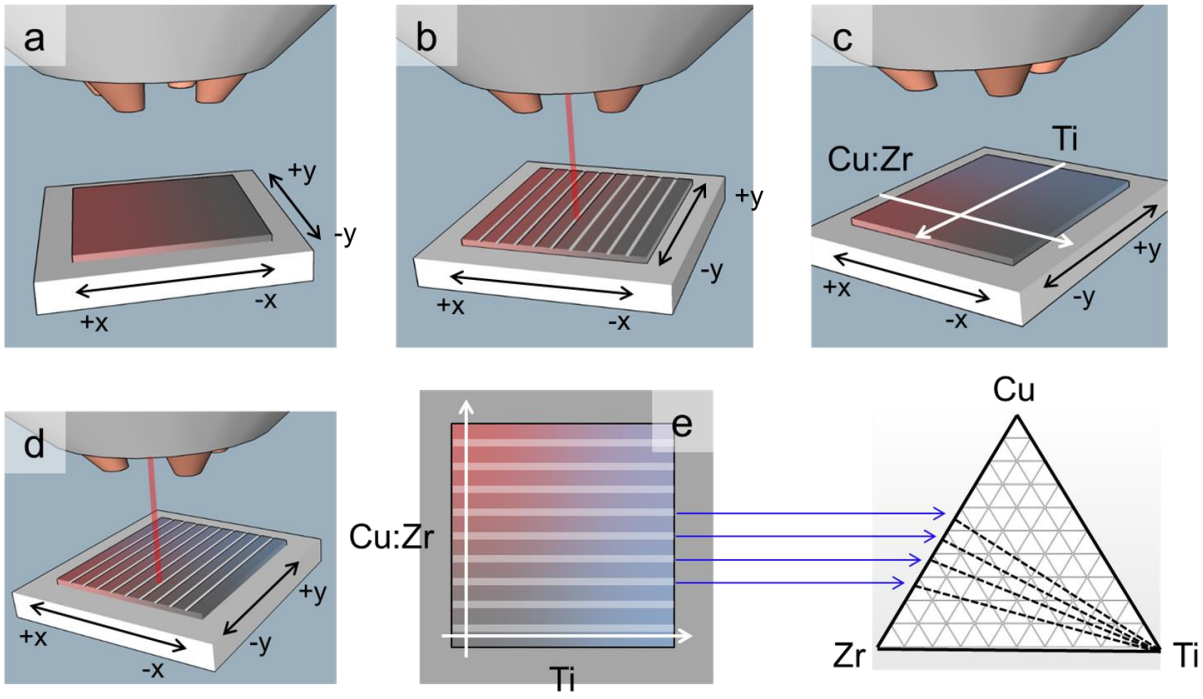

Figure 4.1 Experimental concept for fabricating a Cu-Zr-Ti composition library via laser additive manufacturing. **(a)** Initial deposition of two successive layers of Cu and Zr to produce a graded Cu-Zr composition profile. **(b)** Creation of evenly-spaced re-melted lines perpendicular to the direction of the composition gradient to promote thorough mixing of the two components. **(c)** Deposition of Ti gradient in a direction perpendicular to the initial gradient. **(d)** Final glazing of the re-melted lines with a fast laser to promote vitrification. **(e)** The alloyed lines in the completed library correspond to ternary tie lines featuring a fixed Cu:Zr ratio.

20 minutes to complete, including the three deposited layers and intermediate re-melting steps. The processing parameters used to create the specimens are summarized in Table 4.1.

A built-in two-wavelength pyrometer was used to obtain cooling rates at the surface of the laser melted zones corresponding to the 200 W, 240 W, and 280 W laser power settings. In situ acquisition of accurate temperature profiles during fabrication of the libraries was challenging due to the varying emissivity across the libraries requiring different camera exposure times. Because Zr constitutes the bulk of the thermal mass in the composition libraries, it was assumed that cooling rates are dominated by the thermal transport properties of the underlying substrate. Therefore,

temperature profiles were collected from laser line scans performed separately on a bare Zr substrate to estimate the cooling rates involved during fabrication of the libraries.

Library	Powder delivery rate (g/min)			Laser travel speed (mm/s)	Final re-melt laser power (W)	Average surface cooling rate, 1600 - 2200 ˚C
	Cu	Zr	Ti			(K/s)
Continuous 1	4.12	2.83	0.93	8.47 - 29.63	200	1.68×10^4
Continuous 2	4.12	2.83	1.3	8.47 - 29.63	240	1.43×10^4
Continuous 3	4.12	2.83	1.51	8.47 - 29.63	280	1.19×10^4
Discrete Array	0.56 - 8.80	2.51 - 0.77	0.56	8.47 - 29.63 (Ti)	180	--

Table 4.1 Processing parameters for the Cu-Zr-Ti composition libraries.

In previous work, we have demonstrated the ability to rapidly identify glassy regions of laser-deposited composition libraries using an optical microscopy-based differential interference contrast (DIC) imaging method [36,37]. We applied this high-throughput screening method to the ternary libraries prepared in this work. As was demonstrated in our prior work, smooth, liquid-like segments were assumed to be indicative of vitrified material, in contrast to the rough surface topography of crystalline material. The correlation between the smooth surface topography and a glassy structure was later confirmed by TEM. To define a compositional range of glass formation, composition measurements were collected via energy dispersive spectroscopy (EDS) at the endpoints of each topographically-smooth segment within a library.

Following the fabrication of the continuously-graded libraries, three different alloy compositions possessing high GFA in the Cu-Zr-Ti ternary system were prepared by copper mold suction casting. Two of these alloys, $Cu_{60}Zr_{30}Ti_{10}$ and $(Cu_{0.64}Zr_{0.36})_{90}Ti_{10}$, were identified in the literature as having large critical casting dimensions [22,38] . The third alloy, $Cu_{51.7}Zr_{36.7}Ti_{11.6}$, was identified in the present work as potentially having a greater GFA than these literature

compositions. The cast specimens were prepared from elemental feedstock metal with minimum purities of 99.8 at. %. Differential scanning calorimetry (DSC) was performed for the three alloys to obtain T_g and onset temperature of crystallization T_x. Differential thermal analysis (DTA) was used to obtain the liquidus temperature T_l. The heating rates for the DSC and DTA traces were 20 K min^{-1} and 5 K min^{-1}, respectively.

4.2.2 Discrete composition library for mechanical properties evaluation

An alternative deposition scheme was used to create a 12 x 12 square array of discrete composition "dot" specimens, with each dot spaced 2 mm from its nearest neighbors (Fig. 4.2). Cu and Zr powders were simultaneously deposited row by row with a 250 W laser. In this deposition scheme, the powders were again continuously delivered to the substrate, but the laser shutter was open for a duration of 120 milliseconds only at the positions defined in the array. The delivery rates of the two elemental powders were maintained fixed during the deposition of a row of dots to achieve a constant Cu:Zr molar ratio within each row. After completion of a row, the powder delivery rates were adjusted incrementally to increase the molar ratio in the next row of dots. This was repeated sequentially until completion of the array, resulting in a discretized Cu-Zr composition gradient along each column. Following the initial deposit, a layer of Ti powder was deposited over the entire array of binary dots using a 150 W laser and the travel speed increasing in the -x direction from 8.47-29.63 mm/s. Each dot was re-melted with a 200 W laser and a pulse time of 200 milliseconds to facilitate thorough mixing of the three components. In the final step, the array was re-melted again with a 180 W laser and reduced pulse time of 60 milliseconds. Following fabrication, EDS was used for compositional characterization of the library.

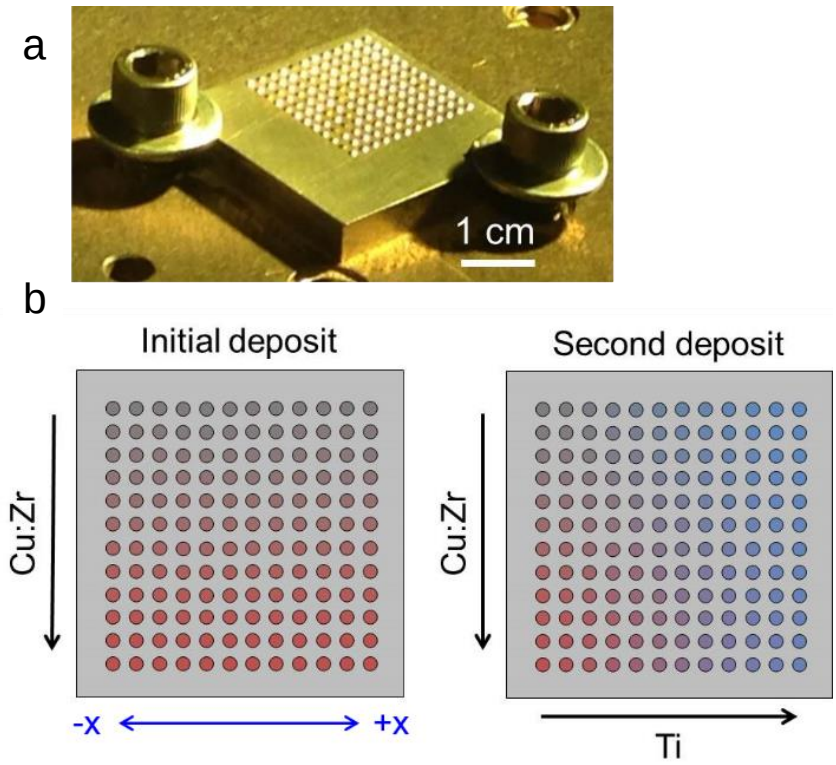

Figure 4.2 (a) Photograph of discrete dot Cu-Zr-Ti composition library. **(b)** Schematic illustrating the deposition scheme for incorporating the desired composition gradients in the discrete dot libraries. Black arrows indicate direction of increasing Cu:Zr molar ratio (vertical) and Ti content (horizontal).

The DIC microscopy screening method was also applied to identify vitrified dots in the discrete library. Due to the exceptionally smooth surface of the vitrified material, no further polishing was necessary to prepare the discrete dot library for instrumented nanoindentation measurements. All indentation experiments were performed with a Hysitron TI 950 Triboindenter equipped with a diamond Berkovich indenter tip. Using a maximum load of 25 mN and loading rate of 3.1 mN/s, four indents, spaced 10 μm apart, were performed in the central region of each vitrified dot in the array to obtain average hardness (H) and indentation modulus (E_r) values.

4.3 Results

4.3.1 Continuously-graded libraries

A number of distinct surface topographies were observed in the as-deposited specimens, representing a wide spectrum of possible microstructures, from fully amorphous (featureless and smooth) to fully crystalline (rough with distinct asperities) (Fig. 4.3). The surface roughness of smooth regions was quantitatively evaluated with scanning probe microscopy. The resulting probe images yielded sub-nanometer roughness values, an order of magnitude lower than the surface roughness of metallic samples that have been polished to a mirror finish with colloidal media.

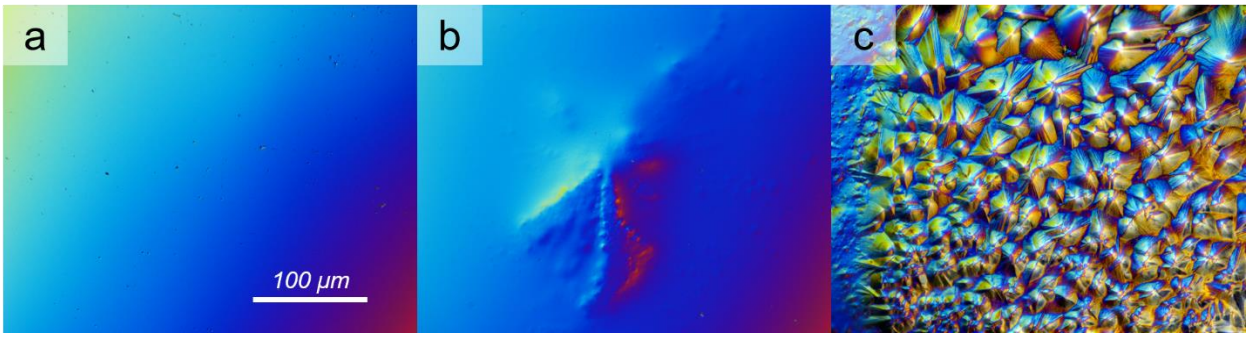

Figure 4.3 Differential interference contrast (DIC) optical micrographs showing the surface topography of various microstructures in the as-deposited libraries. **(a)** Fully amorphous, **(b)** Semi-crystalline and **(c)** Crystalline.

Using the smooth surface topography as an indicator of a predominantly glassy structure, the compositional range of glass formation was identified in each of the three as-deposited libraries (Fig. 4.4). The compositional range of the glass region was observed to diminish with increasing laser power (or laser heat input, defined below), consistent with our previous findings in the Cu-Zr binary system [36,37]. A master plot containing the experimentally-obtained glass region of each

library is shown on the ternary composition map in Figure 4.5. For comparison, two compositions [22,38] reported in literature to possess high GFA are also shown on the plot.

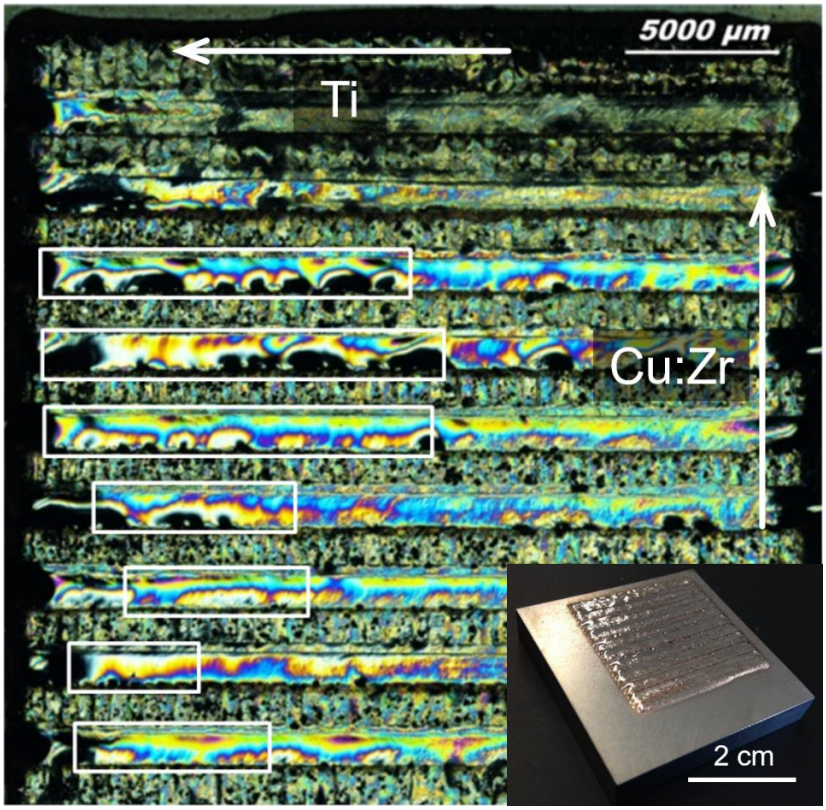

Figure 4.4 DIC image of the composition library processed with a 200 W laser. The boxed segments collectively represents the glass-forming region identified by observing the smooth, liquid-like topography of amorphous material. White arrows indicate directions of increasing Ti and Cu:Zr molar ratio. Inset is a photograph of a complete as-deposited library.

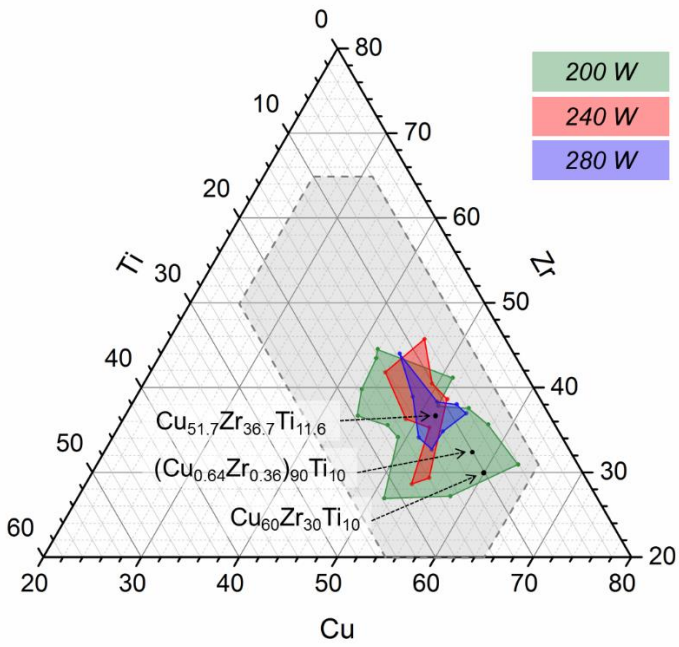

Figure 4.5 Vitrified regions of three composition libraries processed with different final-glazing laser powers (200, 240, and 280 W), plotted on a ternary composition map. The black dot within the glass region of the 280 W library is the predicted best glass former. The other two black dots are notable glass formers previously reported in other studies (Refs. 22 and 38). The gray region approximates the overall extent of the ternary composition space contained within the three libraries.

Average surface cooling rates estimated from laser melting a Zr substrate are listed in Table 4.1, calculated directly from the measured thermal profiles by the product of the temperature gradient with laser travel speed, averaged from 1600 to 2200 ˚C. (While the cooling rate through the glass transition temperature is of greatest interest, lower temperatures were not accessible by the two wavelength pyrometer employed in this study.) The estimated rates decrease with increasing laser power, in agreement with the diminishing compositional range of vitrified regions in the three continuously-graded libraries. The magnitude of the estimated surface cooling rates are also consistent with prior finite element analyses of cooling rates achieved with the LENS™ process [39,40].

4.3.2 Discrete composition library

Figure 4.6 shows a cross-sectional view of a dot screened as amorphous in the discrete composition library. Heat affected zones corresponding to each re-melting step are clearly visible, surrounding a featureless melt zone that is presumably amorphous. The featureless melt zone has a depth of approximately 200 µm, sufficiently thick to avoid substrate effects during nanoindentation. The apex of the dots provided a flat, planar surface for nanoindentation, eliminating the usual requirement of post-fabrication polishing. Assuming a radius of curvature of at least 1 mm, and indentations with lateral dimensions of 2 µm, the variation in surface height across the width of an indent would not exceed 10 nm for the indents performed in this study, meeting the acceptable surface condition required for nanoindentation.

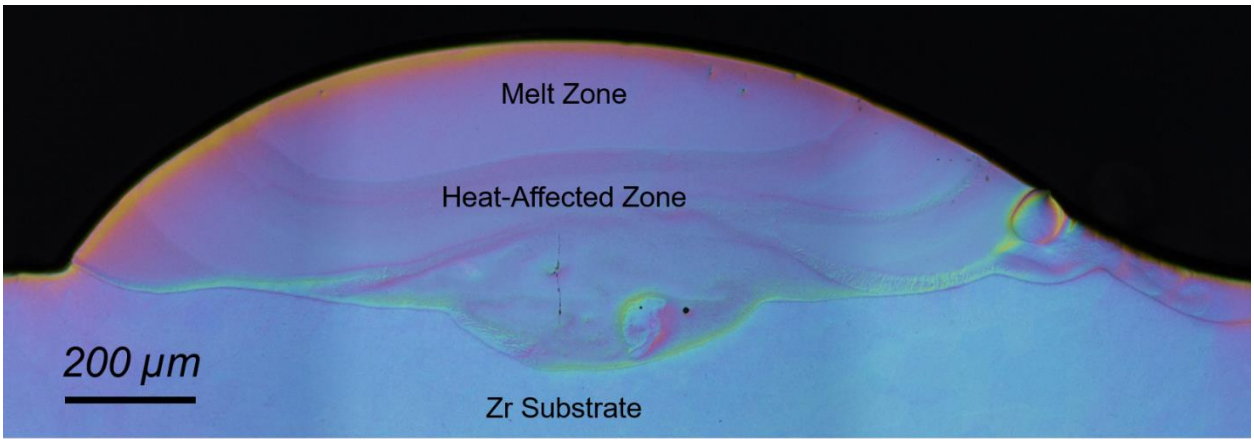

Figure 4.6 DIC image of a cross section through one of the dots screened as amorphous in the discrete composition library. Heat affected zones produced by the re-melting steps are visible surrounding a featureless melt zone.

Of the 144 discrete dots in the discrete composition library, 92 of them were screened as amorphous via differential interference contrast imaging. Figure 4.7a-b are property-composition contour plots for the measured E_r and H values. Each data point used to construct the plots

represents the average value of interest from the four indents performed on every vitrified dot in the array (*see Experimental Methods*). The average standard deviation was 0.85 GPa and 0.03 GPa for E_r and H, respectively.

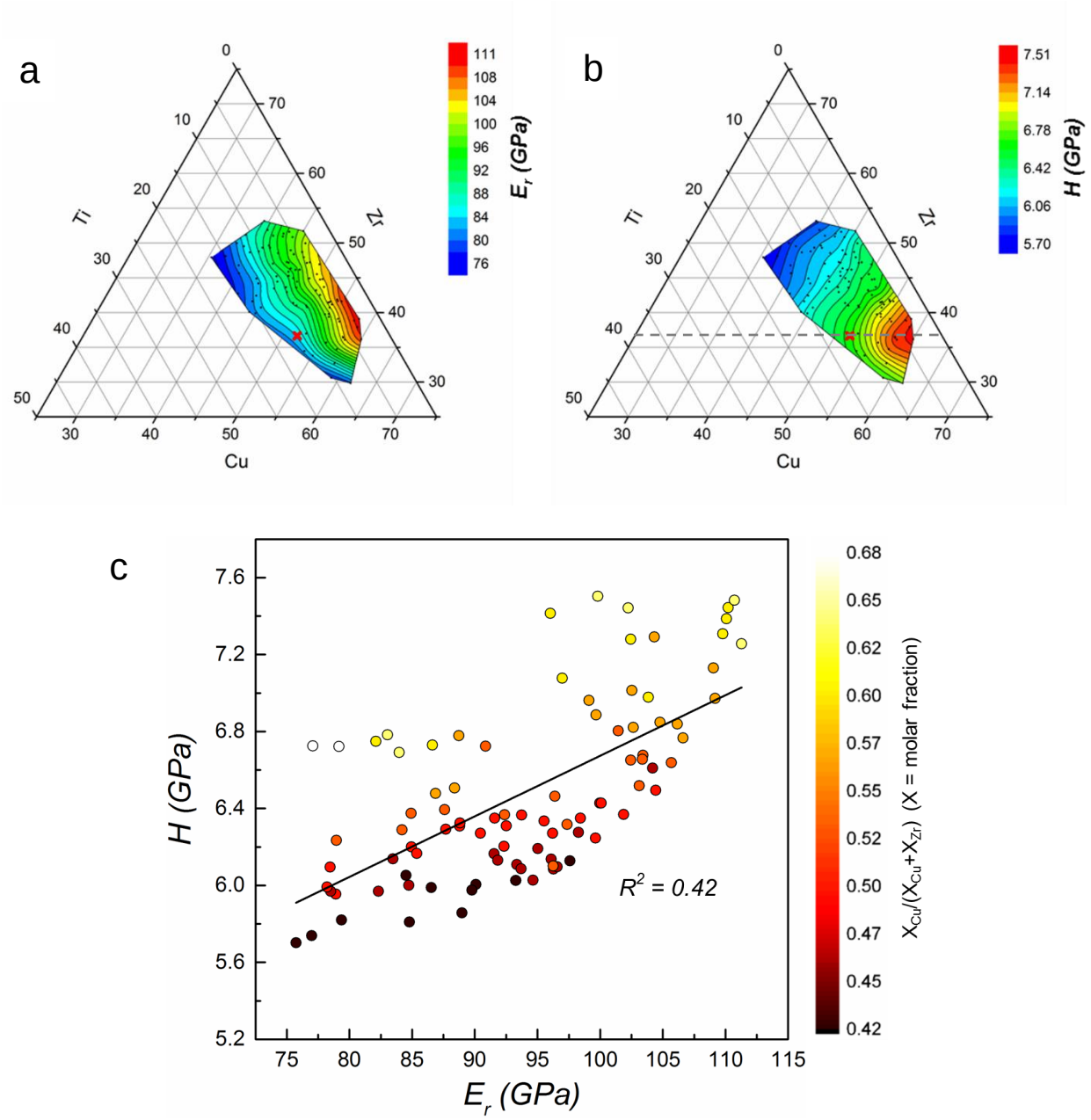

Figure 4.7 (a) Reduced modulus and **(b)** hardness contour plots, constructed from nanoindentation measurements performed on 92 glassy alloys within the ternary Cu-Zr-Ti system. Our predicted best glass-former is indicated by a red X. **(c)** Hardness plotted against the reduced modulus for all 92 alloys. The color of each data point indicates its corresponding Cu:Zr molar ratio.

It should be noted that the discrete and continuously graded composition libraries did not overlap completely; the continuous libraries extended to larger Ti contents than the 12 x 12 array of discrete dots. Thus, while the property maps of Figure 4.7 do not include all of the glass forming compositions delineated in Figure 4.5, this is because the complete 12 x 12 array did not include any dots in that composition range. In fact, the glass forming range of the discrete dots extends to lower Ti and Cu contents than was observed in any of the continuously-graded libraries.

4.4 Discussion

A central goal of this work was to demonstrate a high-throughput method for evaluating glass forming ability as a function of composition in multicomponent alloys. This was facilitated by the use of differential interference contrast (DIC) optical microscopy, which is highly sensitive to surface topography, to screen the as-deposited libraries and eliminate the obviously crystalline compositions from further consideration. When the free surface of a liquid solidifies, crystal nucleation and growth produces a rough surface that is easily visible using DIC [41]. In contrast, if the liquid vitrifies on cooling, no surface asperities are apparent using DIC, suggesting a lack of crystallites larger than the resolution of the measurement, on the order of 100 nm. Further scanning probe microscopy observations of the smooth regions identified by DIC confirmed sub-nanometer RMS surface roughness values, consistent with the lack of even smaller crystallites. Using this screening as a first step, the amorphous structure can then be confirmed by x-ray or electron diffraction methods. In our previous studies of the binary Cu-Zr system [36,37], TEM foils extracted from the smooth areas identified by DIC were repeatedly verified as amorphous by electron diffraction, lending support for DIC microscopy as a reliable screening tool. For the remainder of

this work, we assume that the regions of the composition libraries screened as "smooth" by DIC are primarily amorphous.

In order to evaluate the glass-forming ability of a given alloy composition, it is necessary to experimentally access a wide range of cooling rates. In the conventional serial casting approach, this is accomplished primarily by casting wedge shaped specimens or several individual specimens of different cross-sectional thicknesses, in order to determine the critical casting thickness that avoids crystallization. Notably, the measured critical thicknesses are highly sensitive to other processing parameters, such as the initial temperature of the melt or dwell time in the liquid phase prior to casting. Differences in the details of the processing often lead to different critical casting dimensions [25] as measured by different laboratories, complicating cross-lab comparisons. In the present work, the full range of compositions in a given library are prepared under consistent processing conditions, facilitating the GFA comparison.

In laser processing, cooling rates within the localized melt pool depend largely on the laser heat input, defined as $\lambda = P/(vD)$, where P, v, and D denote laser power, travel speed, and beam diameter, respectively. It is well-known from studies involving crystalline alloys that high laser powers or low travel speeds produce coarser grain microstructures, signaling an inverse scaling of cooling rate with λ [42–44]. Thus, an alloy's minimum or critical cooling rate should correspond to an upper limit of λ. Indeed, Chen *et al.* performed laser surface melting experiments on $Cu_{60}Zr_{30}Ti_{10}$ substrates and reported a threshold laser power above which crystallization became unavoidable [45]. Similarly, Sun and Flores conducted laser deposition experiments with a Zr-based BMG powder on amorphous substrates of the same composition [46]. By fixing P and increasing v above a threshold value, the authors were able to nearly eliminate crystalline features from the heat affected zone. Taking advantage of the empirical relationship between GFA and laser heat input,

we demonstrated in our prior studies of compositionally-graded binary specimens that increasing the applied λ has the general effect of narrowing the compositional range of glass formation towards the best glass-former in the system [36,37].

It follows that the reduction in the extent of the smooth region within the ternary composition libraries with increasing laser power, or equivalently, increasing λ (Fig. 4.5), was a direct consequence of subjecting the ternary libraries to successively lower cooling rates. Our pyrometer measurements of surface temperature profiles indicated that increasing the laser power from 200 W to 280 W reduces the average cooling rate by nearly 30%. As cooling rates decreased with increasing laser power, fewer compositions remained that could vitrify, resulting in the gradual convergence of the glass region towards the composition with the highest GFA. Based on this trend in GFA with λ and a qualitative assessment of the overlapping regions in Figure 4.5, GFA appears to be much more sensitive to the Ti content than to Cu or Zr; the glass forming regions narrow much more rapidly with changes in Ti content than with Cu or Zr. This is consistent with the extensive glass forming range of the Cu-Zr binary system.

It is important to note that the average surface cooling rates (on the order of 10^4 K/s) measured with the pyrometer are not the *critical* cooling rates required for glass formation in the vitrified regions within the libraries. The critical cooling rate for glass formation is derived from averaging the instantaneous cooling rate in the temperature range between T_g and T_l, approximately 430 – 900 ˚C for near-eutectic Cu-Zr-Ti compositions, well below the range of the pyrometer employed in the present study. However, the measured surface cooling rates are consistent with the results of previous finite element models of laser surface melting in similar metallic glass systems [38,39]. These models demonstrated that the instantaneous cooling rate decreases rapidly with time and temperature after the surface heating event. Approaching the glass transition

temperature, the cooling rates measured by the models were an order of magnitude lower than those measured at high temperatures. Both the peak temperature and the cooling rates also decrease rapidly away from the surface. While the high temperature surface cooling rates measured here represent an extreme, the pyrometry results remain useful in providing quantitative verification of the inverse relationship between laser heat input and average cooling rate, as well as the relative change in the necessary critical cooling rate for extending the compositional region of glass formation.

On the basis of the observed GFA trend with composition, we predicted $Cu_{51.7}Zr_{36.7}Ti_{11.6}$ as the optimum glass former in the region of the ternary system covered by our composition libraries. Within this ternary system, Inoue *et al*. had previously identified $Cu_{60}Zr_{30}Ti_{10}$ as a notable glass former [22], while Wang *et al*. further explored glass formation along a series of compositional tie lines and reported $(Cu_{0.64}Zr_{0.36})_{90}Ti_{10}$ as the best glass former in the alloy system [38]. (Note the similarity in the Ti content among these three "optimal" compositions, which again highlights the strong sensitivity of GFA to Ti in this system.) Both studies reported a critical rod diameter of 4 mm for their respective compositions. It is significant that while these two compositions occupied the vitrified region of the 200 W library, they were excluded from the glass regions in the 240 and 280 W libraries, implying that our predicted composition should exhibit higher GFA. In addition, although the same reported critical casting diameter of the Inoue and Wang compositions would suggest equivalence of GFA, our results indicated that $Cu_{60}Zr_{30}Ti_{10}$, positioned near the periphery of the vitrified region in the 200 W library, should have poorer glass forming ability than both Wang's alloy and our predicted composition.

To validate our method for optimizing GFA, wedge samples of $Cu_{51.7}Zr_{36.7}Ti_{11.6}$, $Cu_{60}Zr_{30}Ti_{10}$, and $(Cu_{0.64}Zr_{0.36})_{90}Ti_{10}$ were prepared by copper mold suction casting. Care was

taken to maintain consistent processing conditions for all three alloys. The wedge critical casting thickness was determined to be 1.50, 1.35, and 1.20 mm (± 0.05 mm), respectively for $Cu_{51.7}Zr_{36.7}Ti_{11.6}$, $(Cu_{0.64}Zr_{0.36})_{90}Ti_{10}$, and $Cu_{60}Zr_{30}Ti_{10}$. While these differences are small, they are consistent with the expected ranking of GFA among the three alloys based on the results from the laser-deposited libraries. The apparent discrepancy between the critical casting dimensions measured here and those measured by the Inoue and Wang studies again highlights the difficulty of comparing critical casting dimensions across multiple laboratories and processing methods to evaluate GFA.

Figure 4.8 provides the DSC heating traces for the three suction cast samples. The glass transition temperature T_g, crystallization temperature T_x, and liquidus temperature T_l (obtained from DTA measurements) for each alloy are listed in Table 4.2. Also listed are $T_{rg} = T_g/T_l$ and $\Delta T = (T_x - T_g)$, two of the most prevalent indicators of GFA and glass stability in the literature. According to the ranking of ΔT, $Cu_{51.7}Zr_{36.7}Ti_{11.6}$ has the lowest thermal stability, defined here as the temperature range over which the supercooled liquid resists crystallization. On the other hand, the similar T_{rg} values show no correlation with the respective glass forming ability of the three alloys, as measured by either their critical casting thicknesses or their assumed critical laser heat inputs based on the present work. This demonstrates that, although temperature-based predictors reflect certain crucial aspects of glass formation, they neglect other important determining factors of GFA, such as the structural motifs that comprise the overall glass as well as kinetic properties (e.g. viscosity, dynamic fragility) of the supercooled liquid.

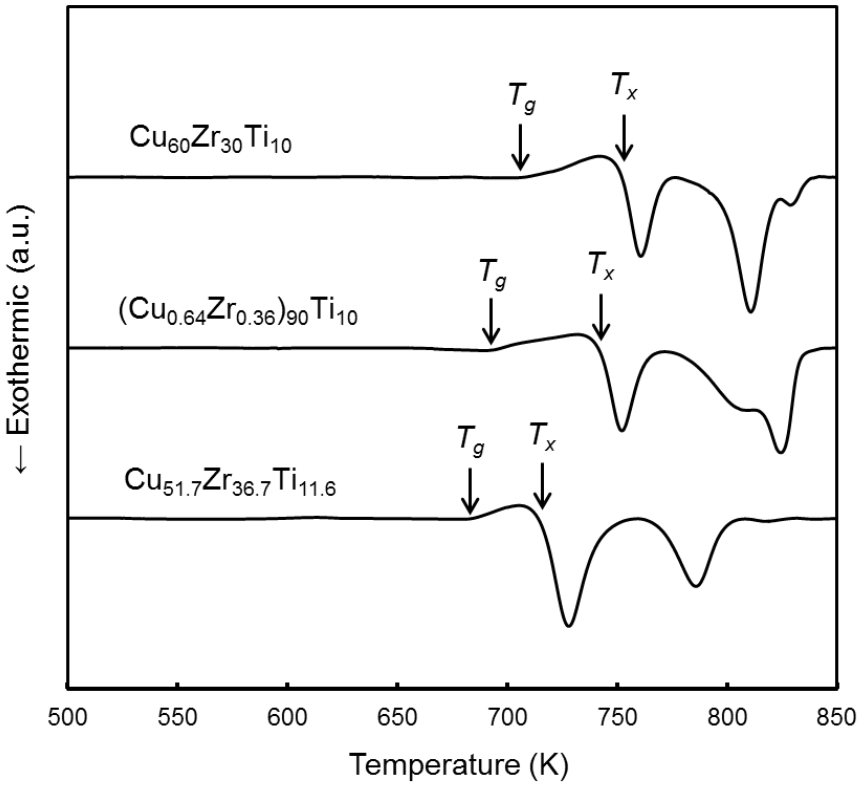

Figure 4.8 Differential scanning calorimetry heating traces of three suction-cast Cu-Zr-Ti metallic glass alloys. The scans were performed at a heating rate of 20 K/min.

Alloy Composition	T_g (K)	T_x (K)	T_l (K)	T_{rg}	ΔT (K)	d_c (mm)
$Cu_{60}Zr_{30}Ti_{10}$	708	751	1146	0.62	43	1.20
$(Cu_{0.64}Zr_{0.36})_{90}Ti_{10}$	693	740	1167	0.59	47	1.35
$Cu_{51.7}Zr_{36.7}Ti_{11.6}$	682	715	1146	0.60	33	1.50

Table 4.2 Characteristic temperatures, temperature-based predictive parameters, and wedge critical casting thickness (d_c) of three Cu-Zr-Ti metallic glass alloys.

A second major objective of this work was to identify correlations between glass composition and mechanical behavior, taking advantage of the extensive compositional range that can be rapidly produced by the laser deposition technique. The contour plot (Fig. 4.7a) of the

measured indentation modulus values from the discrete library shows a strong inverse relationship between E_r and the titanium content and less sensitivity of E_r to changes in the Cu:Zr molar ratio. Comparing Figure 4.5 with 4.7a, it is apparent that GFA does not directly correlate with the elastic modulus.

For alloys with Zr contents less than ~37 at. %, the hardness also exhibits an inverse relationship with the Ti content (Fig. 4.7b). For alloys with greater than 37 at % Zr, however, H diverges from the trend shared with E_r and instead scales with the Cu content. Again, there is no clear correlation between the hardness and GFA. However, it is interesting that the optimal glass forming composition identified in this work, $Cu_{51.7}Zr_{36.7}Ti_{11.6}$ (marked with a red X in Fig. 4.7b), is on the boundary between the region where H scales with Cu and where it scales with Ti. Like the elastic modulus, the hardness (or resistance to plastic deformation) should depend on the underlying atomic structure, in particular the ease with which atomic rearrangements occur. That our optimal composition occurs along the intersection of two competing compositional trends in hardness suggests that it may correspond to a composition at a crossover where two structural motifs are competing for dominance. Further study is required to describe the glass structure as a function of composition in this region of the ternary system.

The disparate compositional trends of H and E_r over the majority of the investigated compositions contrasts with a previous study investigating the correlation between Vickers hardness and shear modulus for a wide variety of BMGs belonging to different compositional families [47]. In that work, the hardness was observed to scale linearly with shear modulus. Figure 4.7c shows a master plot of H versus E_r from data obtained in the present study. The data exhibits a large amount of scatter; a linear fit to the data yielded a relatively low R^2 value of 0.42. However, within narrow bands of Cu:Zr ratios (highlighted by the color-coded scale provided), a stronger

linear trend does seem to persist, with higher Cu:Zr ratios yielding larger intercept values for the trend lines (not shown). Although these results suggest a weak correlation between hardness and modulus over the entire composition range, it is important to recognize that our measurements were limited to only ternary Cu-Zr-Ti alloys and covered a relatively narrow range of hardness values. From a global perspective that includes all BMG alloys, a strong linear relationship between hardness and modulus may still apply, but here we show that deviation from the rule is possible when studying a specific family of alloys.

As shown in Figure 4.7c, for a given value of indentation modulus, hardness increases with increasing Cu content. Indentation hardness measures the resistance of a material to permanent deformation under a constrained state of stress determined by the indenter shape, the applied load, and the material's elastic properties. For two compositions possessing identical E_r but different H values, the elastic contribution to the total tip displacement is the same for both alloys, but the plastic contribution is larger for the alloy with the lower hardness. That is, the alloy with the lower H value would be intrinsically less resistant against plastic flow under identical loading conditions. The direct implication of the trend in hardness with Cu:Zr ratio for a fixed E_r value is that reducing the overall Cu content in the ternary alloys may enhance plasticity.

Recent molecular dynamics studies of the binary Cu-Zr system carried out by Ma *et al*. have linked elastically soft regions within the heterogeneous structure of the model glasses to a propensity to undergo localized, non-affine shear transformations [48,49]. Moreover, the soft regions strongly corresponded with the most unstable atomic cluster species, termed by the authors as geometrically unstable motifs (GUMs). It was observed that the population of GUMs increased with increasing Zr content (decreasing Cu) in the binary alloys, providing a fundamental design rationale for the discovery of $Zr_{61}Cu_{25}Al_{12}Ti_2$, which to date exhibits the highest reported fracture

toughness among known monolithic BMG alloys [50]. Our experimental finding that decreasing the Cu content promotes plastic deformation in Cu-Zr-Ti ternary alloys is in agreement with the results of these previous studies, suggesting structural changes of the glass with varying composition as the underlying reason for the measured trends in H and E_r.

The present work introduces a high-throughput method for rapidly evaluating the relative ductility or toughness of glass forming alloys. It should be noted that the state of stress in nanoindentation experiments is very different from the stress distribution immediately ahead of crack tip in fracture toughness tests, and one could argue that pronounced plasticity observed in indentation does not necessarily translate to higher fracture toughness or ductility. However, if we assume that plastic flow is ultimately dictated by the availability of structurally soft regions that are more susceptible to shear transformation, alloys with a denser population of soft spots should display a greater intrinsic capacity for accommodating plastic strain regardless of the manner in which stress is applied. Although further experimental validation is needed, we propose that the high-throughput mechanical testing method described in this paper, in conjunction with computational modeling, offers a promising pathway for designing new monolithic alloys with optimal combinations of toughness and GFA.

4.5 Conclusions

We have demonstrated a novel high-throughput methodology to systematically examine glass formation in complex, multicomponent alloy systems. Continuously graded Cu-Zr-Ti libraries covering a composition range of several tens of atomic percent were rapidly fabricated by a laser additive manufacturing technique. Smooth, liquid-like surface topographies in the as-deposited libraries were indicative of vitrified material, enabling rapid screening via optical microscopy to define continuous regions of glass forming within a library. Multiple libraries were

synthesized with varying laser heat input in the final re-melting step. With increasing laser heat input, the regions of glass formation were observed to gradually diminish towards the glass-forming composition(s) with the lowest critical cooling rate(s). $Cu_{51.7}Zr_{36.7}Ti_{11.6}$ was estimated as the optimum glass former in the ternary system and subsequent casting results verified the new alloy's superior GFA in comparison with previously identified bulk glass formers.

Nanoindentation measurements performed on the discrete composition library revealed that indentation modulus was primarily sensitive to the Ti content, while hardness was sensitive to Ti for low Zr contents and to Cu for high Zr contents. The cross-over in the trend for hardness with composition, which corresponded to the composition of the optimal glass former identified in this work, suggested a change in the underlying structural motifs controlling both glass forming ability and plastic deformation. Comparison of the hardness and modulus trends further suggested that reducing the Cu content promotes ductility.

Although the procedural strategy described in this study is most suitable for exploring ternary composition space, it could be adapted to interrogate higher order systems through the use of elemental powder blends and pre-alloyed powders. An alternative application of our methodology is the optimization of existing multicomponent BMGs that possess notably high GFA. It is unclear whether such BMGs, originally identified through conventional serial casting methods, truly represent the global GFA maxima in their respective composition space. However, it is likely that the global maximum lies in the compositional neighborhood of these alloys [25]. By using the method described in this paper to probe the neighboring space surrounding known glass formers, new BMGs with optimized GFA could be quickly identified.

4.6 References

1. Tsai, P. & Flores, K. M. High-throughput Discovery and Characterization of Multicomponent Bulk Metallic Glass Alloys. *Acta Mater.* **120,** 426–434 (2016).

2. Caron, P. & Tasadduq, K. Evolution of Ni-based superalloys for single crystal gas turbine blade applications. *Aerosp. Sci. Technol.* **3,** 513–523 (1999).

3. Furrer, D. & Fecht, H. Ni-based superalloys for turbine discs. *Jom* **51,** 14–17 (1999).

4. Wang, W. H., Dong, C. & Shek, C. H. Bulk metallic glasses. *Mater. Sci. Eng. R Reports* **44,** 45–89 (2004).

5. Schroers, J. Processing of bulk metallic glass. *Adv. Mater.* **22,** 1566–97 (2010).

6. Zhao, J. C. A combinatorial approach for structural materials. *Adv. Eng. Mater.* **3,** 143–147 (2001).

7. Zhao, J. C. Combinatorial approaches as effective tools in the study of phase diagrams and composition-structure-property relationships. *Prog. Mater. Sci.* **51,** 557–631 (2006).

8. Gebhart, T., Music, D., Takahashi, T. & Schneider, J. M. Combinatorial thin film materials science: From alloy discovery and optimization to alloy design. *Thin Solid Films* **520,** 5491–5499 (2012).

9. Han, S. M. *et al.* Combinatorial studies of mechanical properties of Ti-Al thin films using nanoindentation. *Acta Mater.* **53,** 2059–2067 (2005).

10. Ludwig, A., Zarnetta, R., Hamann, S., Savan, A. & Thienhaus, S. Development of multifunctional thin films using high-throughput experimentation methods. *Int. J. Mater. Res.* **99,** 1144–1149 (2008).

11. Turnbull, D. Under what conditions can a glass be formed ? *Contemp. Phys.* **10,** 473–488 (1969).

12. Inoue, A., Zhang, T. & Masumoto, T. Glass-forming ability of alloys. *J. Non. Cryst. Solids* **156–158,** 473–480 (1993).

13. Inoue, A. STABILIZATION OF METALLIC SUPERCOOLED LIQUID. *Acta Mater.* **48,** 279–306 (2000).

14. Miracle, D. B. A structural model for metallic glasses. *Nat. Mater.* **3,** 697–702 (2004).

15. Miracle, D. B. The efficient cluster packing model – An atomic structural model for metallic glasses. *Acta Mater.* **54,** 4317–4336 (2006).

16. Wang, A. P., Wang, J. Q. & Ma, E. Modified efficient cluster packing model for calculating alloy compositions with high glass forming ability. *Appl. Phys. Lett.* **90,** 121912:1–3 (2007).

17. Cheng, Y. Q. & Ma, E. Atomic-level structure and structure–property relationship in metallic glasses. *Prog. Mater. Sci.* **56,** 379–473 (2011).

18. Lu, Z. P. & Liu, C. T. A new glass-forming ability criterion for bulk metallic glasses. *Acta Mater.* **50,** 3501–3512 (2002).

19. Laws, K. J., Miracle, D. B. & Ferry, M. A predictive structural model for bulk metallic glasses. *Nat. Commun.* **6,** 8123 (2015).

20. Waniuk, T. A., Schroers, J. & Johnson, W. L. Critical cooling rate and thermal stability of Zr–Ti–Cu–Ni–Be alloys. *Appl. Phys. Lett.* **78,** 1213–1215 (2001).

21. Long, Z. *et al.* On the new criterion to assess the glass-forming ability of metallic alloys. *Mater. Sci. Eng. A* **509,** 23–30 (2009).

22. Inoue, A., Zhang, W., Zhang, T. & Kurosaka, K. High-strength Cu-based bulk glassy alloys in Cu–Zr–Ti and Cu–Hf–Ti ternary systems. *Acta Mater.* **49,** 2645–2652 (2001).

23. Johnson, W. L., Na, J. H. & Demetriou, M. D. Quantifying the origin of metallic glass formation. *Nat. Commun.* **7,** 10313 (2016).

24. Choi-Yim, H., Xu, D. & Johnson, W. L. Ni-based bulk metallic glass formation in the Ni–Nb–Sn and Ni–Nb–Sn–X (X=B,Fe,Cu) alloy systems. *Appl. Phys. Lett.* **82,** 1030–1032 (2003).

25. Na, J. H. *et al.* Compositional landscape for glass formation in metal alloys. *Proc. Natl. Acad. Sci.* **111,** 9031–9036 (2014).

26. Deng, Y. P. *et al.* A combinatorial thin film sputtering approach for synthesizing and characterizing ternary ZrCuAl metallic glasses. *Intermetallics* **15,** 1208–1216 (2007).

27. Chen, C. J. *et al.* On the amorphous and nanocrystalline Zr-Cu and Zr-Ti co-sputtered thin films. *J. Alloys Compd.* **483,** 337–340 (2009).

28. Chou, H. S. *et al.* Amorphous and nanocrystalline sputtered Mg-Cu thin films. *J. Alloys Compd.* **483,** 341–345 (2009).

29. Hata, S., Yamauchi, R., Sakurai, J. & Shimokohbe, A. Combinatorial Arc Plasma Deposition of Thin Films. *Jpn. J. Appl. Phys.* **45,** 2708–2713 (2006).

30. Li, A. Y., Guo, Q., Kalb, J. A., Thompson, C. V & Li, Y. Matching Glass-Forming Ability with the Density of the Amorphous Phase. *Science* **322,** 1816–1819 (2008).

31. Ding, S., Gregoire, J., Vlassak, J. J. & Schroers, J. Solidification of Au-Cu-Si alloys investigated by a combinatorial approach. *J. Appl. Phys.* **111,** 114901:1–6 (2012).

32. Ding, S. *et al.* Combinatorial development of bulk metallic glasses. *Nat. Mater.* **13,** 1–7 (2014).

33. Evertz, S. *et al.* Revealing the relationships between chemistry, topology and stiffness of ultrastrong Co-based metallic glass thin films: A combinatorial approach. *Acta Mater.*

107, 213–219 (2016).

34. Yu, H. Bin, Luo, Y. & Samwer, K. Ultrastable metallic glass. *Adv. Mater.* **25,** 5904–5908 (2013).

35. Chen, N. *et al.* Formation and properties of Au-based nanograined metallic glasses. *Acta Mater.* **59,** 6433–6440 (2011).

36. Tsai, P. & Flores, K. M. A combinatorial strategy for metallic glass design via laser deposition. *Intermetallics* **55,** 162–166 (2014).

37. Tsai, P. & Flores, K. M. A Laser Deposition Strategy for the Efficient Identification of Glass-Forming Alloys. *Metall. Mater. Trans. A* **46A,** 3876-3882 (2015).

38. Wang, Q. *et al.* Cu-Zr-Al(Ti) bulk metallic glasses: Cluster selection rules and glass formation. *Intermetallics* **15,** 711–715 (2007).

39. Sun, H. & Flores, K. M. Laser deposition of a Cu-based metallic glass powder on a Zr-based glass substrate. *J. Mater. Res.* **23,** 2692–2703 (2008).

40. Sun, H. & Flores, K. M. Formation of metallic glass coatings via laser deposition. *30th Int. Congr. Appl. Lasers Electro-Optics, ICALEO 2011, Oct. 23, 2011 - Oct. 27, 2011* 503–510 (2011).

41. Ausserre, D. & Valignat, M. P. Wide-Field Optical Imaging of Surface Nanostructures. *Nano Lett.* **6,** 1384–1388 (2006).

42. Majumdar, J. D., Pinkerton, A., Liu, Z., Manna, I. & Li, L. Microstructure characterisation and process optimization of laser assisted rapid fabrication of 316L stainless steel. *Appl. Surf. Sci.* **247,** 320–327 (2005).

43. Amine, T., Newkirk, J. W. & Liou, F. An investigation of the effect of direct metal deposition parameters on the characteristics of the deposited layers. *Case Stud. Therm. Eng.* **3,** 21–34 (2014).

44. Frazier, W. E. Metal additive manufacturing: A review. *J. Mater. Eng. Perform.* **23,** 1917–1928 (2014).

45. Chen, B. Q. *et al.* Surface vitrification of alloys by laser surface treatment. *J. Alloys Compd.* **511,** 215–220 (2012).

46. Sun, H. & Flores, K. M. Microstructural Analysis of a Laser-Processed Zr-Based Bulk Metallic Glass. *Metall. Mater. Trans. A* **41,** 1752–1757 (2010).

47. Chen, X. Q., Niu, H., Li, D. & Li, Y. Modeling hardness of polycrystalline materials and bulk metallic glasses. *Intermetallics* **19,** 1275–1281 (2011).

48. Ding, J., Patinet, S., Falk, M. L., Cheng, Y. & Ma, E. Soft spots and their structural signature in a metallic glass. *Proc. Natl. Acad. Sci.* **111,** 14052–14056 (2014).

49. Ma, E. Tuning order in disorder. *Nat. Mater.* **14,** 547–552 (2015).

50. Xu, J. & Ma, E. Damage-tolerant Zr–Cu–Al-based bulk metallic glasses with record-breaking fracture toughness. *J. Mater. Res.* **29,** 1489–1499 (2014).

Chapter 5

Hierarchical Heterogeneity and an Elastic Microstructure Observed in a Metallic Glass Alloy

This chapter is largely adapted from a manuscript that has been prepared for and submitted to *Nature Communications* for publication, and written in collaboration with K. Kranjc and K.M. Flores. I carried out the dynamic modulus mapping experiments, analyzed all experimental raw data, and am the main contributor of the manuscript. K. Kranjc carried out the nanoindentation experiments and provided relevant data. K.M. Flores wrote part of the manuscript and provided supervision as the principle investigator of the work.

5.1 Introduction

To reiterate, the nanoindentation property trends discussed in the previous chapter brings to light the importance of structure, in addition to chemistry, as a determining factor of mechanical properties in BMGs. Nevertheless, while property trends may expose regimes in composition space where different structural motifs prevail (e.g. crossover in indentation hardness trend within the Cu-Zr-Ti system), the actual details of glass structure and its correlation with mechanical properties require further interrogation at a microscopic level.

Understanding structure-property relationships has long been at the heart of alloy development and design. For crystalline alloys, depending on the complexity of the overall microstructure, variations in structural features could span length scales across many orders of magnitude. Due to the periodic nature of atomic packing in even the most complex crystalline alloys, their underlying structures are readily characterized by conventional techniques such as electron microscopy and x-ray diffraction. In contrast to crystalline alloys, the atomic structure of monolithic metallic glasses is devoid of long range translational symmetry, although it is known

that short and medium range ordering persists[1–3]. For this reason, metallic glasses appear deceptively homogeneous and isotropic when investigated with conventional characterization techniques, without the typical microstructural features that account for complexity and uniqueness in crystalline alloys. Despite the apparent microstructural similarity of metallic glasses, however, their deformation behavior can vary drastically with both alloy composition and processing conditions[4–6], implying the existence of a complex underlying structure that is not yet fully understood.

On the atomic length scale, the structure of an amorphous alloy is by definition heterogeneous, possessing a statistical spread of different atomic cluster configurations, randomly orientated and distributed throughout its volume. Structural heterogeneities extending beyond the size of atomic clusters are less obvious, especially considering the high atomic packing efficiency of bulk amorphous alloys and their general resemblance to the disordered liquid[7]. Recent experimental and molecular dynamics studies have reported nanoscale heterogeneous structure in metallic glasses[8–13]. The presence of such heterogeneities carries profound implications with respect to macroscopic mechanical behavior[14]. For example, in simulated Cu-Zr binary glasses, Ma *et al.* demonstrated that elastically-soft regions densely populated with unstable cluster motifs are more susceptible to local shear transformations[12,13,15]. The authors proposed that increasing the population of soft spots in a glass would encourage profuse shear banding, resulting in high fracture toughness and enhanced plastic behavior, both of which are rare among known bulk metallic glasses (BMG). On the experimental front, using atomic force microscopy techniques, nanoscale fluctuations of elastic modulus and energy dissipation have been measured in several amorphous alloys[8–11], but important details such as the characteristic size of the heterogeneous

features, their morphology and spatial distribution, and their sensitivity to thermal processing history remain ambiguous.

5.2 Experimental Methods

We used two techniques, quasi-static nanoindentation and dynamic modulus mapping (DMM) on a nanoindentation platform, to investigate spatial fluctuations of mechanical properties in $Zr_{58.5}Cu_{15.6}Ni_{12.8}Al_{10.3}Nb_{2.8}$, a BMG with centimeter-scale critical casting thickness[16]. In the nanoindentation experiments, a 20 x 25 array of indents spaced 3 μm apart were performed on each specimen. The maximum load for each indent was 1500 μN, with loading and unloading rates of 300 μN/s. To explore the existence of heterogeneities on a smaller length scale, the DMM experiments were performed over reduced areas measuring 3 μm x 3 μm. DMM combines scanning probe microscopy with dynamic mechanical analysis to map the indentation modulus in a 256 x 256 pixel array over a region of interest on a sample's surface. During mapping, a sinusoidal load function is applied such that the nanoindenter tip (diamond Berkovich) maintains contact with the surface at all times. An appropriate load amplitude is chosen to achieve a tip displacement amplitude between 1-2 nm, resulting in good image contrast while ensuring all deformation remains elastic. A load frequency of 200 Hz was used for all mapping experiments conducted in this study. Accounting for the mass (m_T) and stiffness (k_T) of the force transducer, the indentation storage stiffness (k') of the sample can be calculated from the following expression:

$$k' = \frac{F_D \cos(\phi)}{d_D} + m_T \times \omega^2 - k_T$$

where F_D, d_D, ϕ, and ω are the dynamic load, dynamic displacement, phase shift, and angular frequency, respectively. For the small dynamic displacements in DMM experiments, the

Berkovich tip can be approximated as spherical with a radius of curvature *r*. The storage modulus (E_r') is then obtained from the stiffness values according to classical Hertzian contact theory:

$$E_r' = \sqrt{\frac{(k')^3}{6F_D r}}$$

The BMG samples used for both nanoindentation and DMM were prepared by arc melting pure elements in an argon atmosphere and casting into a copper mold to produce a 3 mm diameter rod. Four slices, each approximately 1 mm thick, were prepared from the as-cast rod and polished to a mirror finish with colloidal silica. Nanoindentation was performed on the polished surface of two of the slices, one of which was annealed at 370 °C ($0.95T_g$, where T_g is the glass transition temperature) for 2 hours prior to the experiments. Modulus mapping was performed on the remaining two slices in their as-cast state, at multiple locations across the polished cross sections. After the initial DMM experiments, one of the two slices was also annealed at 370 °C for 2 hours, followed by mapping performed at approximately the same locations. Following the mapping experiments, TEM foils were prepared by conventional ion milling to verify the amorphous structure of the as-cast and annealed samples.

5.3 Results

Conventional bright field and high-resolution TEM (Fig. 5.1) confirmed fully amorphous atomic structures for both the as-cast and annealed BMGs. However, annealing caused an increase in the average indentation modulus (E_r) of the glass from 108 to 115 GPa and the average hardness (H) from 7.08 to 7.74 GPa. Significant spatial variation was also observed in both *H and* E_r, as shown for the as-cast condition in Figure 5.2a-b. Here, both properties are expressed as deviations from average, $100 \times \left(X - X_{avg}\right)/X_{avg}$, where X denotes the measured property of interest. Histograms of the data are well described by Gaussian distributions (Fig. 5.2c-d). The Gaussians

narrow slightly as a result of the annealing treatment. To compare the statistical spread of properties with a structurally homogeneous material, nanoindentation was repeated in the same 20 x 25 pattern on a polished single-crystal silicon wafer grown in the <100> direction. In comparison to the BMG specimens, the silicon displayed a substantially narrower distribution of H and E_r values.

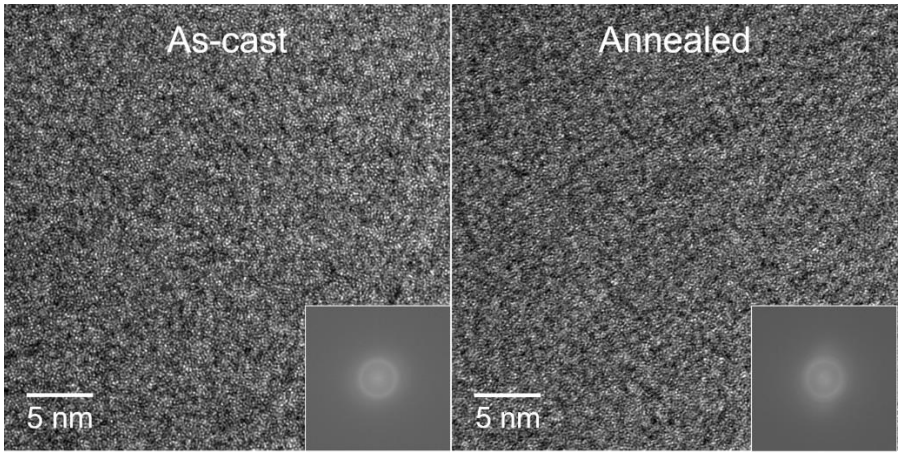

Figure 5.1 High-resolution TEM bright field images of the as-cast and annealed BMG samples used for the modulus mapping measurements. Both samples, prepared from the same cast rod, were fully amorphous, indicated by the maze pattern and accompanying FFT diffraction patterns.

Figure 5.3a shows 9 of the 3 μm x 3 μm storage modulus maps collected from 13 locations on the circular cross section of one of the polished slices in the as-cast state. For ease of comparison between different mapping locations, the modulus values are again represented as a normalized deviation from average rather than their absolute values. Spatial fluctuations of local elastic properties are clearly evident in each of the maps, forming an "elastic microstructure" with a stiffer-than-average network encompassing pockets of elastically softer material. Corresponding histograms of the modulus data exhibited statistical profiles that can be fit with bimodal mixed-Gaussian distributions (Fig. 5.3b). Figure 5.3c is a collection of normalized autocorrelation

functions (see 2.3.1 for more information) derived from the 13 modulus maps. Significant directionality of the elastic fluctuations is present near the edge of the circular cross section, with the heterogeneous features circumferentially aligned with the edge. The strength of the alignment decreases away from the edge towards an approximately non-directional distribution of heterogeneities at the center of the cross section.

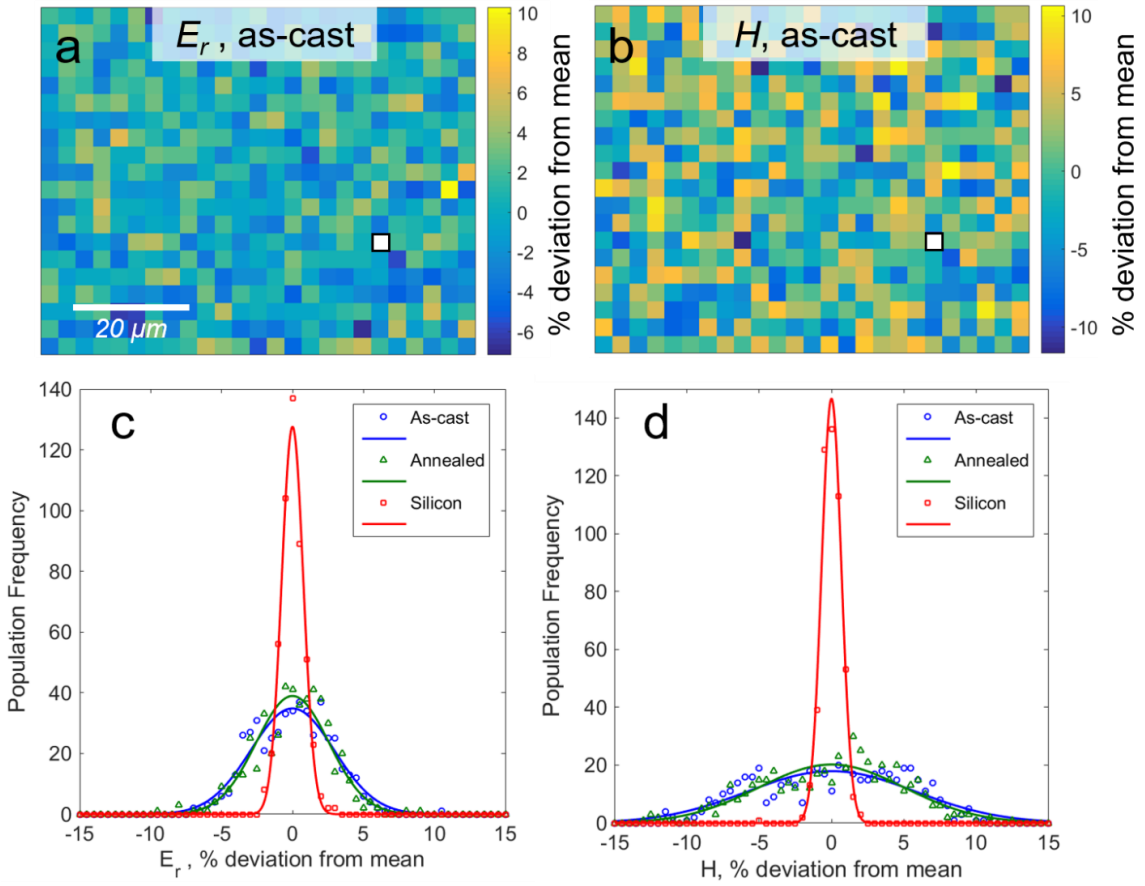

Figure 5.2 Micron-scale heterogeneities observed by instrumented nanoindentation. **(a-b)** Color map representations of 500 nanoindentation (a) modulus, E_r, and (b) hardness, H, measurements collected over a rectangular array measuring 57 μm x 72 μm in an as-cast specimen. The white squares refer to an unsuccessful indent. **(c-d)** Corresponding histograms of (c) E_r *and (d)* H for nanoindentation experiments performed on the as-cast and annealed BMG, as well as a single-crystal silicon wafer grown in the <100> direction for comparison.

a

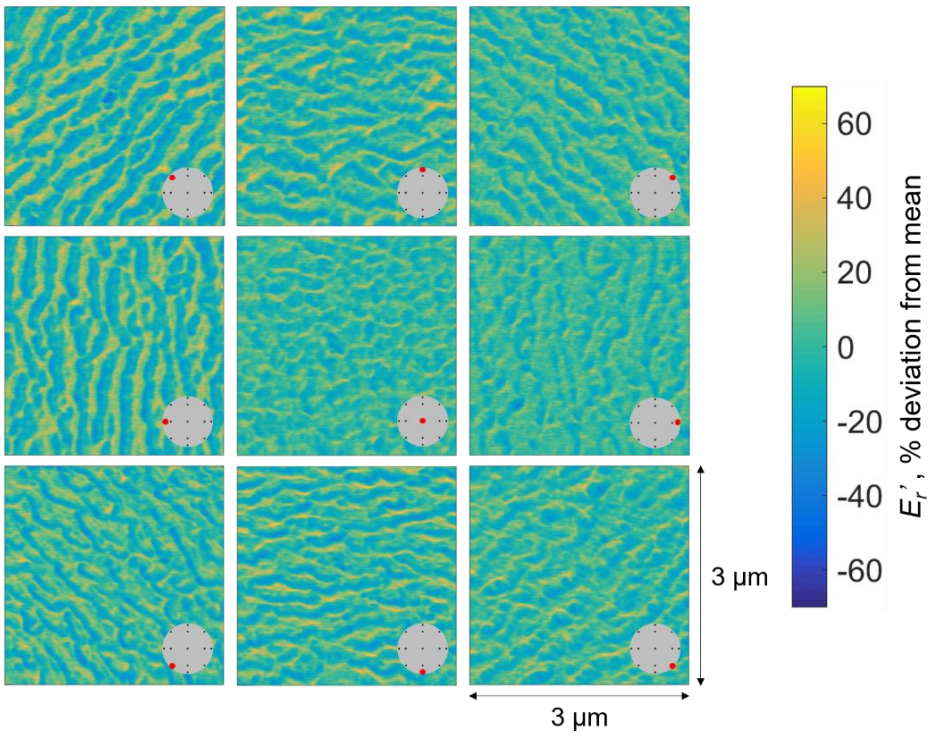
60
40
20
0
-20
-40
-60
E_r', % deviation from mean
3 µm
3 µm

b

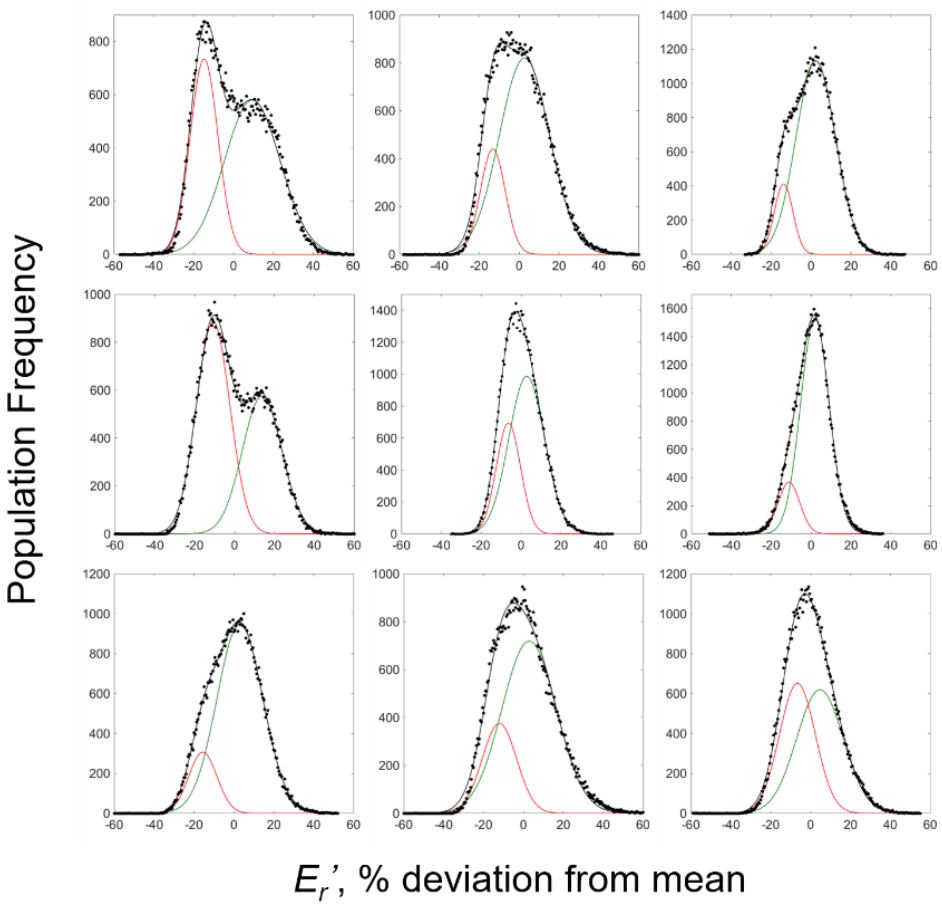
Population Frequency
E_r', % deviation from mean

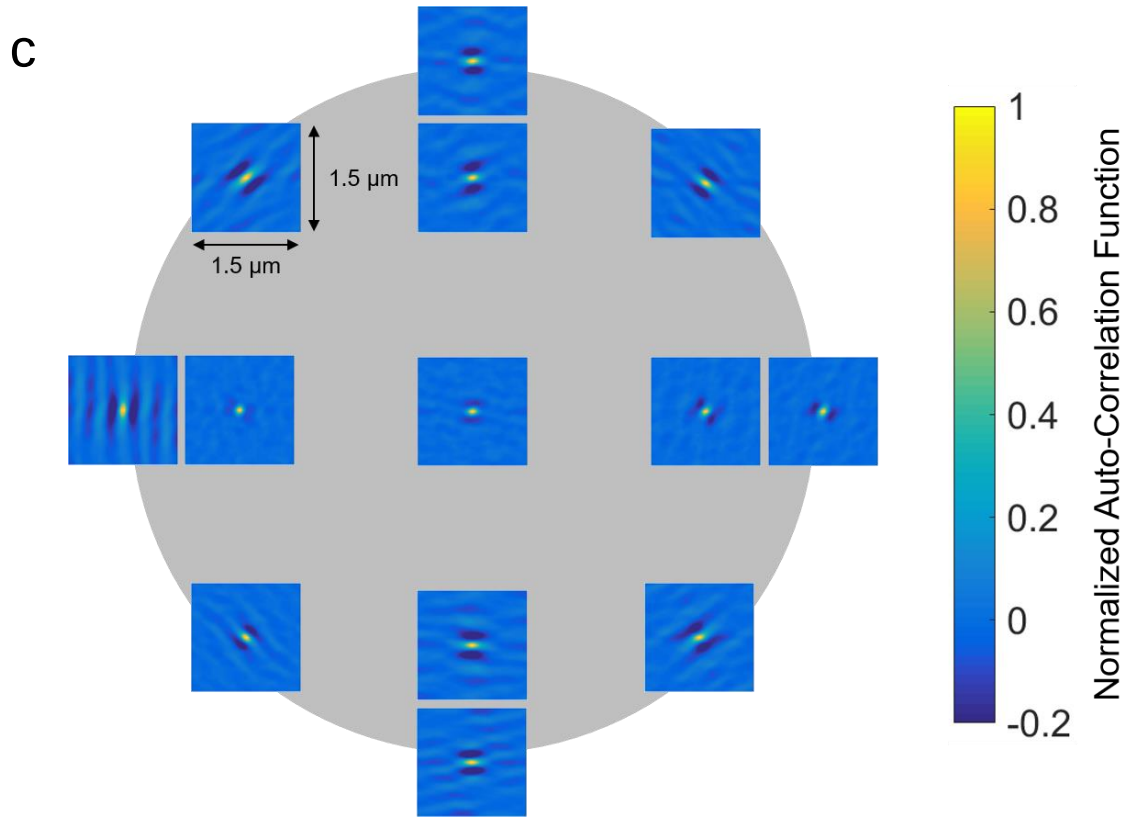

Figure 5.3 Elastic heterogeneities observed by dynamic modulus mapping. **(a)** Selected 3 µm x 3 µm storage modulus (E_r') maps for the BMG in the as-cast condition, collected from various locations (lower right insets) around the cross section of the cylindrical specimen. **(b)** Corresponding histograms, showing a bi-modal Gaussian distribution of E_r'. **(c)** Normalized auto-correlation functions corresponding to the modulus maps collected from all 13 locations examined, revealing the circumferential alignment of the elastic features and variation with radial position.

Although a Gaussian or Gaussian-like distribution of elastic moduli in metallic glass is consistent with previous computational and experimental studies of nanometer-scale heterogeneities[10,17–19], random errors will also contribute to a Gaussian profile. To evaluate the severity of random error contributions, DMM was performed on the same polished silicon wafer used for the nanoindentation experiments. The resulting modulus map and histogram are shown in Figure 5.4a-b. Similar to the indentation results comparing the silicon and BMG, the modulus map collected from the silicon was much more uniform than the maps collected from the BMG.

The corresponding histogram exhibited a full width at half maximum (FWHM) of 6.2%, compared to 22.5% for the mapping data obtained from the central location of the BMG sample cross section. At positions near the edge of the BMG cross section, the degree of variability is even more severe, with FWHM as large as 42.5 %.

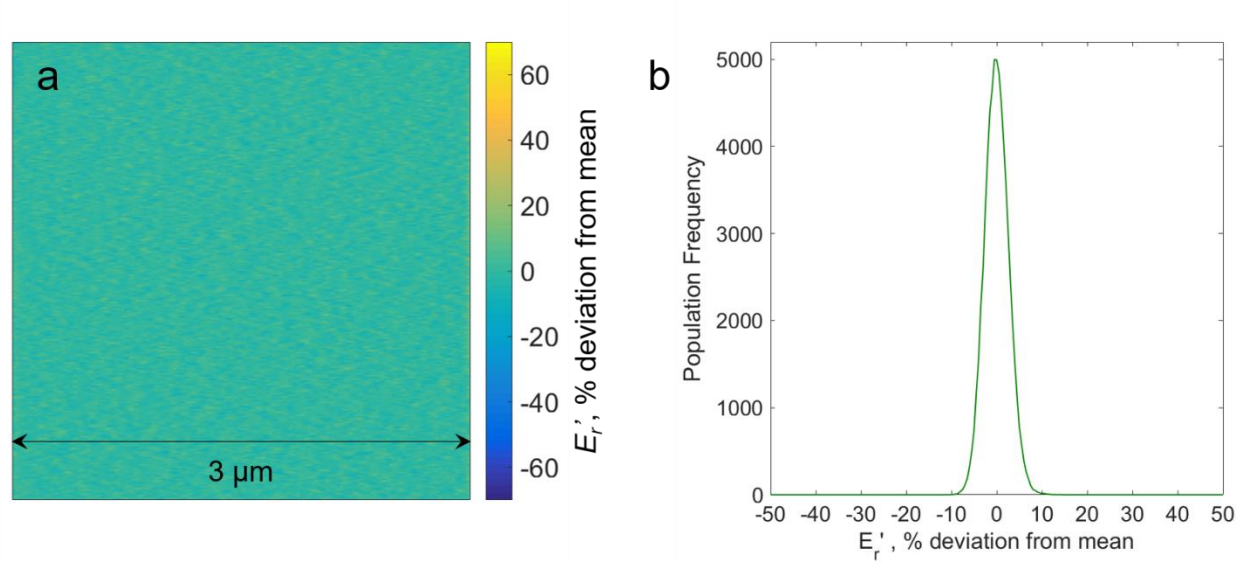

Figure 5.4 Absence of spatial heterogeneities in a structurally homogeneous material. **(a)** 3 μm x 3 μm storage modulus map collected from the surface of a single-crystal silicon wafer grown in the <100> direction and **(b)** corresponding histogram.

Dynamic modulus maps collected from the annealed sample used for studying the effects of thermal relaxation showed elastic microstructures very similar to those from the as-cast state (Fig. 5.5a). Histograms of the data (Fig. 5.5b) also revealed a narrowing in the statistical spread of E_r' at each mapping location as a result of the annealing process.

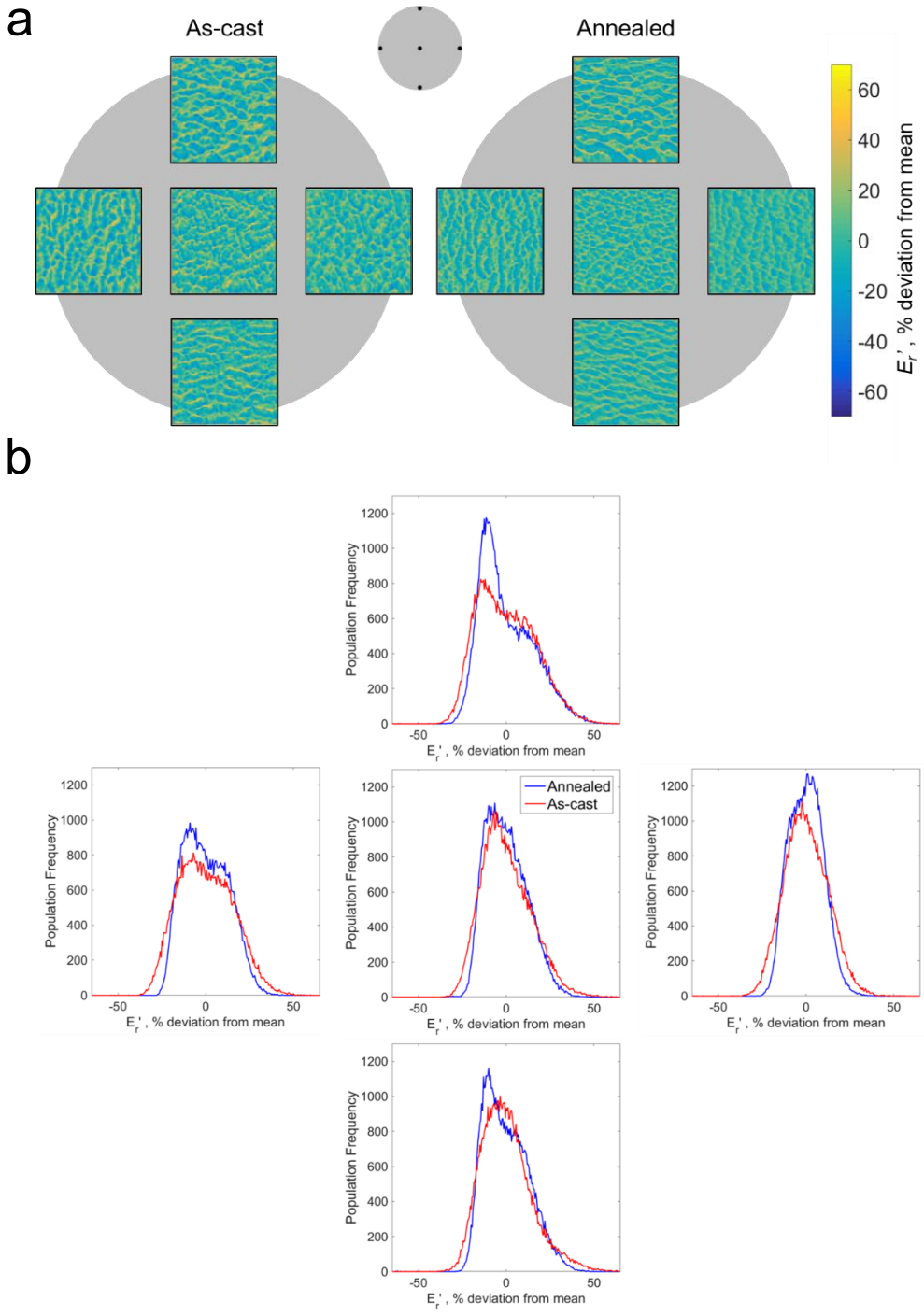

Figure 5.5 The effect(s) of annealing treatment on the statistical and spatial distribution of elastic heterogeneity. **(a)** Two sets of storage modulus maps obtained from the same specimen before (left) and after (right) isothermal annealing treatment for 2 hours at 370 °C. Maps collected post-annealing were from approximately the same locations. **(b)** Corresponding histograms demonstrating the consistent narrowing of the statistical spread of E_r' values due to thermal annealing.

5.4 Discussion

Both the as-cast and annealed BMG exhibit a much broader distribution of indentation hardnesses (H) and moduli (E_r) compared to the single crystal silicon. Assuming that the distribution of measured H and E_r values in the silicon, which is presumably homogeneous, are indicative of the degree of random error in the measurement, we now consider the source of the much larger variability in the glasses.

A previous study involving numerous BMGs reported a universal linear scaling of Vickers hardness with shear modulus[20]. Compositionally distinct alloys were shown to occupy distinct positions on the universal trend line. In the present work, a linear correlation is observed between H and E_r over the range of measured values in both the as-cast and annealed BMG specimens, as shown in Figure 5.6. Both sets of data obey approximately the same linear scaling law, with $H \sim 0.1E_r$. When plotted together (*inset*), the combined data covers a continuous range with a regression line (not shown) consistent with that of the individual data sets. In contrast to the glass, there appears to be no correlation between H and E_r within the data set of the single-crystal silicon, consistent with the structural and compositional homogeneity of the material. When all three data sets are plotted together, a fit to the master data set reveals a very strong linear relationship between H and E_r, in excellent agreement with the individual glass data sets. The agreement between the linear fits of the BMG data and the overall master trend line including silicon, and the phenomenological agreement with the prior study[20], strongly suggests that a significant portion of the property variability within the BMG samples is due to compositional fluctuations; each indent probed a slightly different composition, resulting in the continuous spread of values along the trend line.

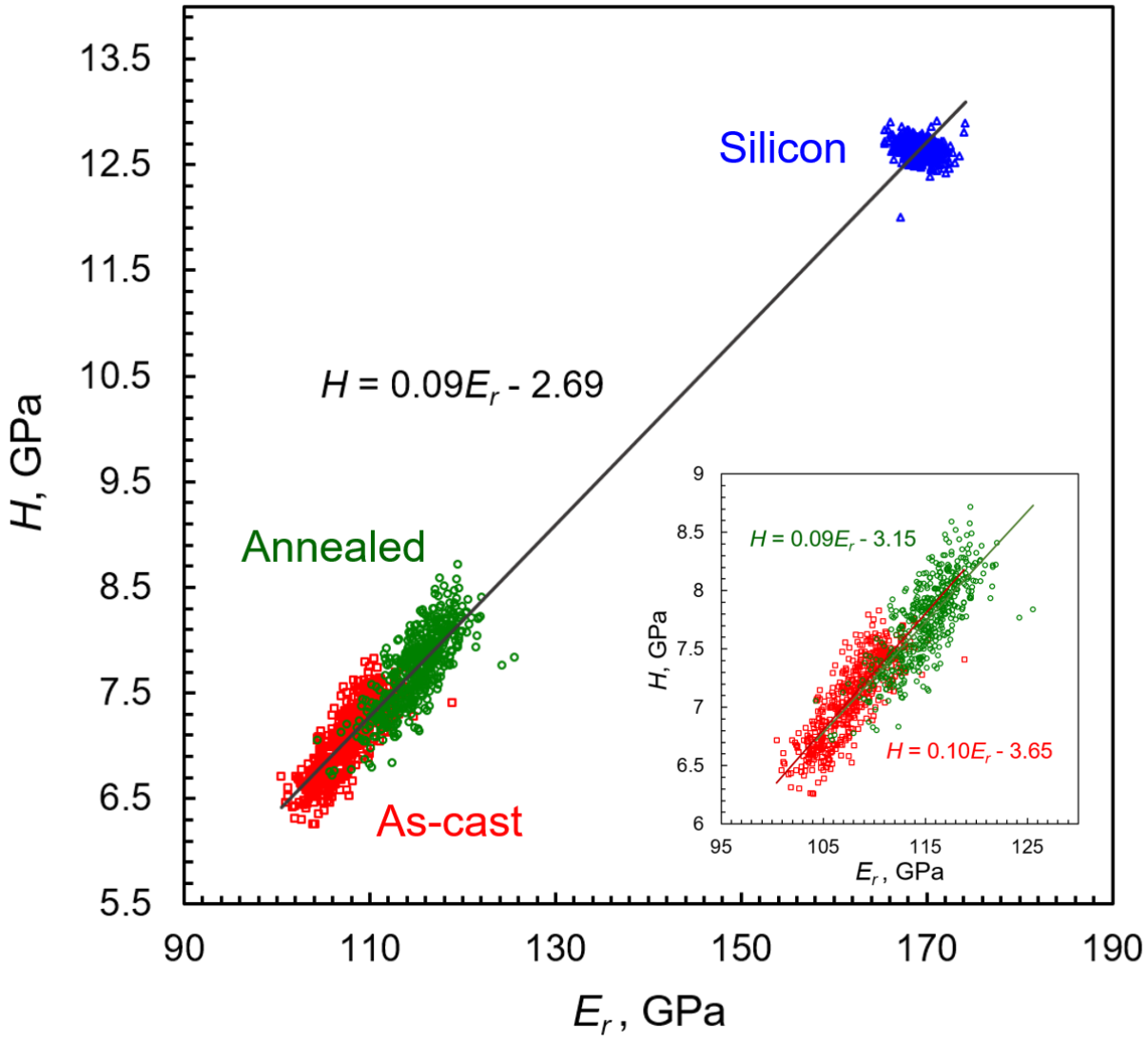

Figure 5.6 *H* plotted against E_r for the data sets collected from the as-cast and annealed BMG samples and the <100> silicon. H scaled linearly with E_r in each of the BMG data sets (*inset*), but the silicon data showed no correlation. When plotted together, the collective data set (BMG and silicon) follows a master trend line in good agreement with the trend lines of the individual BMG data sets.

The linear scaling between *H* and E_r suggests a common structural origin for both properties in metallic glasses. As an elastic property, E_r fundamentally depends on the stiffness of the atomic bonds participating in affine deformation. In perfect crystalline alloys, non-affine deformation is absent in the elastic regime, since the strain is uniformly shared among all atomic

bonds. In contrast to crystalline alloys, a significant fraction of the volume in metallic glasses may be occupied by topologically unstable, liquid-like flow defects that undergo localized non-affine (plastic) strains, even though the macroscopic behavior may appear fully elastic[21,22]. Atoms belonging to the liquid-like regions have a propensity to freely reconfigure under applied stress but do not contribute to the resistance of the glass against macroscopic elastic deformation. Indeed, computational studies of binary Cu-Zr glass have shown that global shear modulus is sensitive to the fraction and interconnectivity of topologically-stable icosahedral clusters that make up the elastic backbone of the glass[23,24]. Hardness, on the other hand, generally describes a material's resistance to irreversible plastic flow, and again, simulations of binary glasses have demonstrated that the onset of global yielding is closely related to the breakdown of the stable clusters that comprise the elastic backbone[24–27], thereby allowing isolated flow defects to coalesce into shear bands. Thus, the same elastic network that determines E_r in metallic glasses also controls the onset of irreversible plastic flow, and therefore H.

Annealing increases the average values of both H and E_r along the same trend line; it also slightly narrows the spread of the data (Fig. 5.2). This slight increase in uniformity most likely reflects an overall increase in atomic packing efficiency due to β-relaxation[11,28–30]. When rapidly quenched, a vitrified specimen initially occupies a metastable state of high potential energy, corresponding to a structure that contains a dense population of topologically-unstable atomic clusters. As the unstable regions undergo β-relaxation during annealing, local atomic structures rearrange into more efficiently packed, stable configurations, increasing the rigidity of the elastic backbone and simultaneously making the initiation of plastic flow more difficult. In the present data, the effect of β-relaxation is expressed as a preferential loss of low hardness, elastically

compliant regions, and therefore a more uniform structure, although compositional fluctuations persist.

The nanoindentation results provide insight into the significant variations in the properties of the glass, and suggest that these variations are primarily the result of compositional fluctuations on a length scale of several microns. Nevertheless, the nanoindentation sampling volumes are very large compared to most conceivable structural length scales in the glass, and therefore the spatial arrangements of the fluctuations in Figures 5.2a-b appear to be random. DMM provides the opportunity to investigate variations in the storage modulus at a much finer spatial resolution. Because the average storage modulus varies from map to map, consistent with the nanoindentation results described above, we focus solely on variations around the mean within each map. Heterogeneity is once again observed (Fig. 5.3a), manifested as nanometer-scale fluctuations of the storage modulus. Notably, the variation from the mean is broader at this length scale than for the nanoindentation results (Fig. 5.3b compared with Fig. 5.2c). At this length scale, the fluctuations are not randomly distributed, and there is a strong circumferential alignment of the elastic heterogeneities with the edge of the cylindrical rod cross sections. Furthermore, although alignment was present along the entire circular edge of the sample cross section, some locations exhibited a much stronger alignment of the elastic features, as revealed by the auto-correlation functions (Fig. 5.3c). We suspect the asymmetrical profile may be the result of an uneven cooling history caused by convection during the casting process.

The gradual increase of circumferential alignment of features with radial distance away from the central region of the cross section is reminiscent of surface-directed spinodal decomposition (SDSD)[31–33], which has been theoretically modeled and extensively observed to occur in certain polymeric mixtures, but has never been reported for metallic glass systems. When

spinodal decomposition transpires in the bulk, the fluctuating composition profile can be described as a superposition of a set of randomly oriented composition wave vectors. Under the right conditions, decomposition occurring near a surface or physical boundary will instead produce a lamellar microstructure, comprising layers of alternating phases and characterized by a dominant wave vector oriented perpendicular to the boundary.

Beside the phenomenological similarity of our modulus maps to microstructures produced by SDSD, several other characteristics of the mapping data point to spinodal decomposition as the probable origin of the elastic fluctuations. First of all, the bi-modal Gaussian fits to the E_r' histograms (Fig. 5.3b) suggests separation into two dominant phases, one elastically more rigid than the other. Second, as was true for the nanoindentation results, histograms of the data (Fig. 5.5b) for the annealed specimen revealed a narrowing in the statistical spread of E_r' at each mapping location, indicating increased uniformity at the submicron length scale as a result of annealing. However, at several locations the bimodal character of the statistical profiles became noticeably more defined with annealing, bifurcating into an enhanced primary peak accompanied by a pronounced shoulder. The preservation of bimodal character with annealing reinforces the notion of spinodal decomposition in the supercooled liquid as the primary cause of the salient heterogeneous features. If the origin of the elastic fluctuations was purely structural (i.e. free volume inhomogeneity) or a byproduct of quenched-in residual stress[34], the annealing treatment would have expectedly homogenized the distribution of E_r' towards a narrower single-Gaussian instead of becoming more bifurcated.

Phase separation in monolithic alloys has been reported previously, and in some cases, has been linked with improved toughness or ductility[35–38]. In known phase-separated alloys, the interface between chemically distinct regions can be either sharp or diffuse, depending on whether

the separation in the undercooled liquid is occurring by a nucleation and growth mechanism or by spinodal decomposition[39]. In our modulus maps, the variation in modulus is continuous and the position of a boundary separating "high" and "low" modulus regions is ambiguous, suggesting spinodal decomposition to be the more probable separation mechanism. It should also be noted that contrast indicative of compositional fluctuations was not apparent in either conventional bright field or high resolution TEM images collected from the as-cast and annealed specimens (Fig. 5.1), seemingly contradicting the possibility of phase separation. However, we note that the absence of heterogeneous microstructure in the bright-field images does not absolutely confirm chemical homogeneity, as demonstrated in previous atomic probe tomography studies of phase-separated BMGs[40,41].

Similar to other dynamic probing methods, surface roughness of the sample could adversely affect the accuracy of DMM measurements[9–11]. In our results, directional alignment of features is evident in both the storage modulus maps and accompanying surface topography maps (Fig. 5.7). (Note that directionally unbiased polishing was applied during sample preparation, which excludes the possibility of polishing causing the observed alignment of the topographical features.) Analysis of the topography images yielded root mean square surface roughness (height) values between 3-5 nm. To further evaluate the potential impact of the surface roughness on our DMM measurements, we compare characteristic feature sizes. A characteristic feature length can be approximated from each storage modulus map by measuring the distance from the origin of the autocorrelation image to its nearest local minimum; the same analysis can be repeated for the corresponding topography maps and the two sets of feature lengths compared. For the modulus maps of the as-cast material in Figure 5.3, the characteristic length ranges from 120 – 147 nm, with an average of 132 nm. Similar results were obtained for the annealed specimen. In contrast,

analysis of the topography images revealed a much larger average characteristic feature length of 190 nm. The dissimilarity of the characteristic lengths of the modulus and topography maps

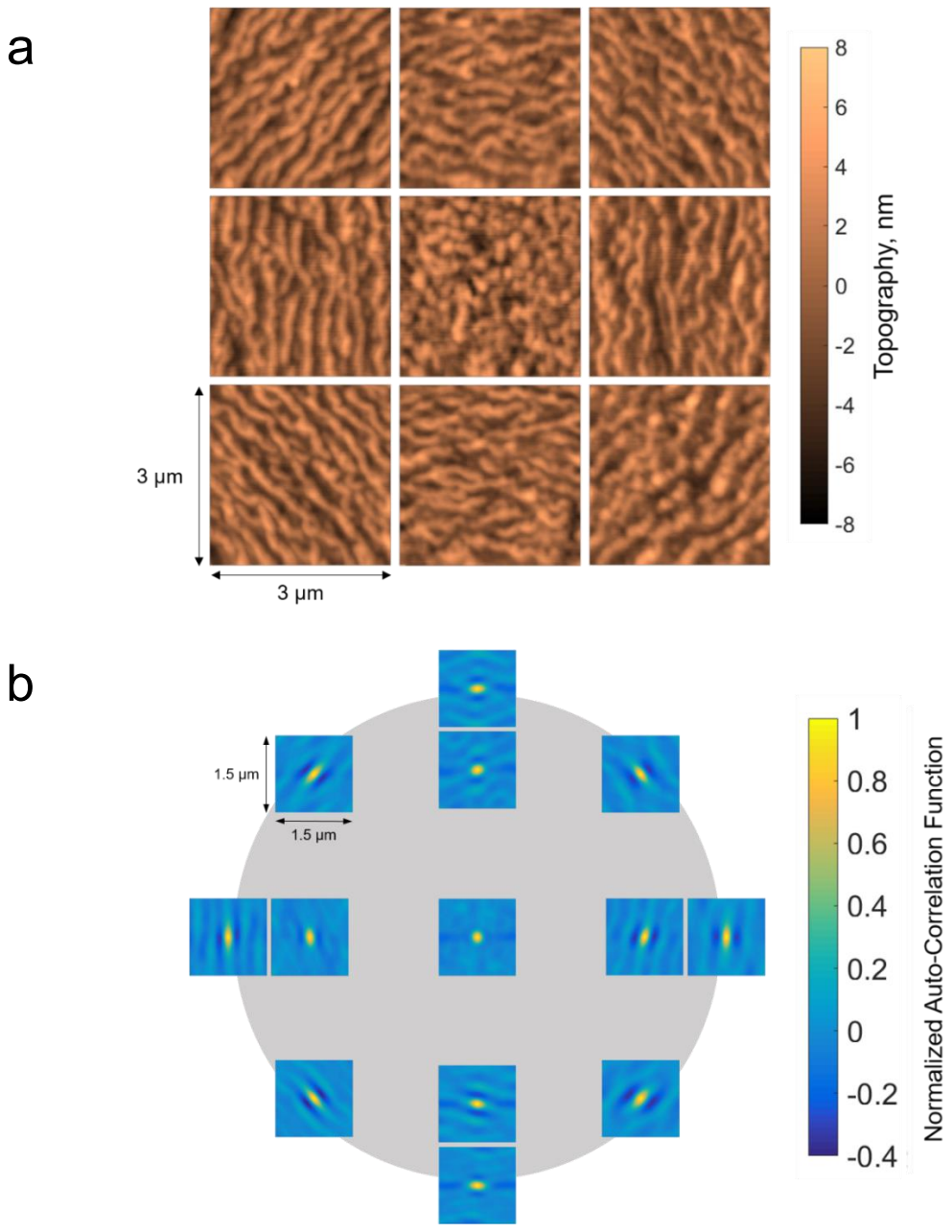

Figure 5.7 (a) Corresponding 3 µm x 3 µm topography (height) images of the modulus maps shown in Fig. 5.3a. **(b)** Normalized auto-correlation functions computed from all 13 topography images.

verifies that the measured elastic fluctuations are intrinsic to the glass and largely unaffected by the minor surface roughness of the polished amorphous sample. Indeed, we conclude that the surface roughness was a result of the fluctuations in local mechanical properties leading to variations in the wear behavior, rather than their cause.

An important difference between the heterogeneous structures we report in the present work and those from previous studies is in the general length scale of the observed fluctuations. The characteristic length scale of the elastic microstructure, on the order of 100 nm, is as much as two orders of magnitude larger than structural heterogeneities discussed in previous studies. A widely-accepted theoretical model based on cooperative shearing estimated a universal diameter of shear transformation zones to be approximately 15 angstroms[42,43]. Similarly, molecular dynamics studies of binary Cu-Zr glasses have reported soft spots with dimensions of a few nanometers[12,13]. Various dynamic AFM studies also reported spatial heterogeneities of internal friction and viscoelastic phase shift with characteristic lengths of a few nanometers[8,9,11]. The elastic microstructure observed in the present work may represent a networked structure of these nanometer-scale heterogeneities. Furthermore, the ~100 nm fluctuations in the storage modulus are superimposed upon larger fluctuations in the average hardness and modulus over micron-scale distances, observed here by nanoindentation. Yet other recent studies have reported millimeter-scale variations in hardness leading to improved tensile ductility and fracture reliability[44,45].

The diversity of characteristic feature sizes investigated through different methods suggests a hierarchical description of heterogeneity in metallic glass alloys that spans several orders of magnitude in length. A hierarchical description of microstructure would expand the role of heterogeneities beyond merely supplying fertile sites for initiating plastic flow at the atomic level, to potentially controlling the pathway and stability of propagating shear bands. Bharathula and

Flores[46] argued that the scatter in the yield strength of microcompression pillars of the $Zr_{58.5}Cu_{15.6}Ni_{12.8}Al_{10.3}Nb_{2.8}$ could be explained by a distribution of defects ranging 90-190 nm, in excellent agreement with the feature size observed here for the same alloy. Work by Jiang and Greer noted that a critical specimen diameter of ~100 nm was required to successfully nucleate a shear band in a similar Zr-based glass[47]; the present work indicates that the elastic modulus is more homogeneous below this length scale. These prior observations raise the possibility that the elastic microstructure may control shear band nucleation and propagation. The current work also indicates that the elastic microstructure is sensitive to conditions of thermal processing, particularly the interaction of the liquid with the mold material as well as temperature gradients that are present during quenching. This may explain the wide statistical scattering in the measured fracture toughness of monolithic BMGs[48–53]. Further investigation is required to determine if significant coarsening or refinement of the elastic microstructure is possible, and if so, what impact this has on shear banding and subsequent fracture behavior.

5.5 Conclusions

In summary, using quasi-static nanoindentation and dynamic modulus mapping, we revealed heterogeneities permeating a Zr-based BMG on two length scales. On a micron-scale, variations in the hardness and indentation modulus occur randomly in space but scale with one another. A similar scaling law has been observed across metallic glasses and brittle materials of different compositions, suggesting that the variations reported in this study are the result of compositional fluctuations on the micron-scale. Superimposed on these variations, at the sub-micron length scale, an “elastic microstructure” is observed. The ~100 nm length scale of the elastic microstructure was in excellent agreement with critical length scales for shear band nucleation and propagation, suggesting that the modulus fluctuations may play an important role

in controlling the plastic deformation of metallic glasses. The observed fluctuations in the storage modulus display a pronounced alignment perpendicular to the direction of the temperature gradients during quenching from the melt. Isothermal annealing treatment at a temperature below the glass transition increased the average values of indentation hardness and modulus but reduced the overall degree of heterogeneity in the alloy. This work demonstrates the importance of thermal processing conditions to the structure of metallic glasses at multiple length scales, and provides a new experimental approach for studying the microstructure of BMGs with a view towards improving the ductility and structural reliability of these materials.

5.6 References

1. Cheng, Y. Q. & Ma, E. Atomic-level structure and structure–property relationship in metallic glasses. *Prog. Mater. Sci.* **56,** 379–473 (2011).
2. Sheng, H. W., Luo, W. K., Alamgir, F. M., Bai, J. M. & Ma, E. Atomic packing and short-to-medium-range order in metallic glasses. *Nature* **439,** 419–25 (2006).
3. Hirata, A. *et al.* Direct observation of local atomic order in a metallic glass. *Nat. Mater.* **10,** 28–33 (2011).
4. Xi, X. K. *et al.* Fracture of brittle metallic glasses: Brittleness or plasticity. *Phys. Rev. Lett.* **94,** 125510:1–10 (2005).
5. Demetriou, M. D. *et al.* A damage-tolerant glass. *Nat. Mater.* **10,** 123–8 (2011).
6. Lewandowski, J. J., Wang, W. H. & Greer, A. L. Intrinsic plasticity or brittleness of metallic glasses. *Philos. Mag. Lett.* **85,** 77–87 (2005).
7. Laws, K. J., Miracle, D. B. & Ferry, M. A predictive structural model for bulk metallic glasses. *Nat. Commun.* **6,** 8123 (2015).
8. Yang, Y. *et al.* Fractal growth of the dense-packing phase in annealed metallic glass imaged by high-resolution atomic force microscopy. *Acta Mater.* **60,** 5260–5272 (2012).
9. Liu, Y. H. *et al.* Characterization of nanoscale mechanical heterogeneity in a metallic glass by dynamic force microscopy. *Phys. Rev. Lett.* **106,** 125504:1–4 (2011).
10. Wagner, H. *et al.* Local elastic properties of a metallic glass. *Nat. Mater.* **10,** 439–42 (2011).

11. Zhu, F. *et al.* Intrinsic correlation between β-relaxation and spatial heterogeneity in a metallic glass. *Nat. Commun.* **7,** 11516 (2016).

12. Ding, J., Patinet, S., Falk, M. L., Cheng, Y. & Ma, E. Soft spots and their structural signature in a metallic glass. *Proc. Natl. Acad. Sci.* **111,** 14052–14056 (2014).

13. Ma, E. Tuning order in disorder. *Nat. Mater.* **14,** 547–552 (2015).

14. Ma, E. & Ding, J. Tailoring structural inhomogeneities in metallic glasses to enable tensile ductility at room temperature. *Mater. Today*, in press (2016).

15. Xu, J. & Ma, E. Damage-tolerant Zr–Cu–Al-based bulk metallic glasses with record-breaking fracture toughness. *J. Mater. Res.* **29,** 1489–1499 (2014).

16. Hays, C. C. *et al.* Vitrification and determination of the crystallization time scales of the bulk-metallic-glass-forming liquid Zr58.5Nb2.8Cu15.6Ni12.8Al 10.3. *Appl. Phys. Lett.* **79,** 1605–1607 (2001).

17. Fan, Y., Iwashita, T. & Egami, T. Evolution of elastic heterogeneity during aging in metallic glasses. *Phys. Rev. E* **89,** 062313:1–7 (2014).

18. Ke, H. B., Zeng, J. F., Liu, C. T. & Yang, Y. Structure Heterogeneity in Metallic Glass: Modeling and Experiment. *J. Mater. Sci. Technol.* **30,** 560–565 (2014).

19. Mizuno, H., Mossa, S. & Barrat, J. L. Measuring spatial distribution of the local elastic modulus in glasses. *Phys. Rev. E* **87,** 042306:1–12 (2013).

20. Chen, X. Q., Niu, H., Li, D. & Li, Y. Modeling hardness of polycrystalline materials and bulk metallic glasses. *Intermetallics* **19,** 1275–1281 (2011).

21. Dmowski, W., Iwashita, T., Chuang, C.-P., Almer, J. & Egami, T. Elastic Heterogeneity in Metallic Glasses. *Phys. Rev. Lett.* **105,** 205502:1–4 (2010).

22. Ketov, S. V *et al.* Rejuvenation of metallic glasses by non-affine thermal strain. *Nature* **524,** 200–203 (2015).

23. Cheng, Y. & Ma, E. Configurational dependence of elastic modulus of metallic glass. *Phys. Rev. B* **80,** 064104:1–6 (2009).

24. Shi, Y. & Falk, M. L. Does metallic glass have a backbone? The role of percolating short range order in strength and failure. *Scr. Mater.* **54,** 381–386 (2006).

25. Lee, M., Lee, C. M., Lee, K. R., Ma, E. & Lee, J. C. Networked interpenetrating connections of icosahedra: Effects on shear transformations in metallic glass. *Acta Mater.* **59,** 159–170 (2011).

26. Cheng, Y. Q., Cao, A. J., Sheng, H. W. & Ma, E. Local order influences initiation of plastic flow in metallic glass: Effects of alloy composition and sample cooling history. *Acta Mater.* **56,** 5263–5275 (2008).

27. Baumer, R. E. & Demkowicz, M. J. Glass Transition by Gelation in a Phase Separating

Binary Alloy. *Phys. Rev. Lett.* **110,** 145502:1–5 (2013).

28. Murali, P. & Ramamurty, U. Embrittlement of a bulk metallic glass due to sub-Tg annealing. *Acta Mater.* **53,** 1467–1478 (2005).

29. Qiao, J. *et al.* Relaxation of Bulk Metallic Glasses Studied by Mechanical Spectroscopy. *J. Phys. Chem. B* **117,** 13658–13666 (2013).

30. Launey, M. E., Busch, R. & Kruzic, J. J. Effects of free volume changes and residual stresses on the fatigue and fracture behavior of a Zr-Ti-Ni-Cu-Be bulk metallic glass. *Acta Mater.* **56,** 500–510 (2008).

31. Ball, R. C. & Essery, R. L. H. Spinodal decomposition and pattern formation near surfaces. *J. Phys. Condens. Matter* **2,** 10303–10320 (1990).

32. Jones, R. A. L., Norton, L. J., Kramer, E. J., Bates, F. S. & Wiltzius, P. Surface-directed spinodal decomposition. *Phys. Rev. Lett.* **66,** 1326–1329 (1991).

33. Knutsson, A. *et al.* Surface directed spinodal decomposition at TiAlN / TiN interfaces Surface directed spinodal decomposition at TiAlN / TiN interfaces. *J. App. Phys.* **113,** 114305:1–8 (2013).

34. Zhang, Y., Wang, W. H. & Greer, A. L. Making metallic glasses plastic by control of residual stress. *Nat. Mater.* **5,** 857–860 (2006).

35. Kündig, A. A., Ohnuma, M., Ping, D. H., Ohkubo, T. & Hono, K. In situ formed two-phase metallic glass with surface fractal microstructure. *Acta Mater.* **52,** 2441–2448 (2004).

36. Park, B. J. *et al.* Phase separating bulk metallic glass: A hierarchical composite. *Phys. Rev. Lett.* **96,** 245503:1–4 (2006).

37. Chen, N., Zhang, H. & Yao, K.-F. Structural heterogeneity in a binary Pd–Si metallic glass. *Philos. Mag. Lett.* **95,** 77–84 (2015).

38. Kim, K. B. *et al.* Heterogeneity of a Cu 47.5 Zr 47.5 Al 5 bulk metallic glass. *Appl Phys Lett* **88,** 051911:1-3 (2006).

39. Kim, D. H., Kim, W. T., Park, E. S., Mattern, N. & Eckert, J. Phase separation in metallic glasses. *Prog. Mater. Sci.* **58,** 1103–1172 (2013).

40. Oh, J. C., Ohkubo, T., Kim, Y. C., Fleury, E. & Hono, K. Phase separation in Cu43Zr43Al7Ag7 bulk metallic glass. *Scr. Mater.* **53,** 165–169 (2005).

41. Mattern, N. *et al.* Spinodal decomposition of Ni-Nb-Y metallic glasses. *Acta Mater.* **57,** 903–908 (2009).

42. Johnson, W. L. & Samwer, K. A universal criterion for plastic yielding of metallic glasses with a (T/Tg)2/3 temperature dependence. *Phys. Rev. Lett.* **95,** 195501:1–4 (2005).

43. Zink, M., Samwer, K., Johnson, W. L. & Mayr, S. G. Plastic deformation of metallic

glasses: Size of shear transformation zones from molecular dynamics simulations. *Phys. Rev. B* **73,** 172203:1–3 (2006).

44. Scudino, S. *et al.* Ductile bulk metallic glasses produced through designed heterogeneities. *Scr. Mater.* **65,** 815–818 (2011).

45. Li, B. S., Shakur Shahabi, H., Scudino, S., Eckert, J. & Kruzic, J. J. Designed heterogeneities improve the fracture reliability of a Zr-based bulk metallic glass. *Mater. Sci. Eng. A* **646,** 242–248 (2015).

46. Bharathula, A. & Flores, K. M. Variability in the yield strength of a metallic glass at micron and submicron length scales. *Acta Mater.* **59,** 7199–7205 (2011).

47. Jang, D. & Greer, J. R. Transition from a strong-yet-brittle to a stronger-and-ductile state by size reduction of metallic glasses. *Nat. Mater.* **9,** 215–219 (2010).

48. Gu, X. J., Poon, S. J., Shiflet, G. J. & Lewandowski, J. J. Ductile-to-brittle transition in a Ti-based bulk metallic glass. *Scr. Mater.* **60,** 1027–1030 (2009).

49. Madge, S. V., Louzguine-Luzgin, D. V., Lewandowski, J. J. & Greer, A. L. Toughness, extrinsic effects and Poisson's ratio of bulk metallic glasses. *Acta Mater.* **60,** 4800–4809 (2012).

50. Henann, D. L. & Anand, L. Fracture of metallic glasses at notches: Effects of notch-root radius and the ratio of the elastic shear modulus to the bulk modulus on toughness. *Acta Mater.* **57,** 6057–6074 (2009).

51. Flores, K. M. & Dauskardt, R. H. Enhanced toughness due to stable crack tip damage zones in bulk metallic glass. *Scr. Mater.* **41,** 937–943 (1999).

52. Gludovatz, B., Naleway, S. E., Ritchie, R. O. & Kruzic, J. J. Size-dependent fracture toughness of bulk metallic glasses. *Acta Mater.* **70,** 198–207 (2014).

53. Chen, W. *et al.* Does the fracture toughness of bulk metallic glasses scatter? *Scr. Mater.* **107,** 1–4 (2015).

Chapter 6

Evolution of the Elastic Microstructure in a Metallic Glass Alloy Revealed by Laser-Pulsed Melting

6.1 Introduction

The ability to sustain substantial plastic strain in tension is an essential attribute of reliable engineering alloys. But among metallic glasses, tensile ductility is rarely observed on the macroscopic length scale, even for recently discovered "damage-tolerant" BMGs with exceptionally high fracture toughness[1,2]. For this reason, despite possessing an attractive set of mechanical properties unique to the material, the implementation of BMGs in structural applications have been very limited since their discovery. To remedy the lack of tensile ductility, some have adopted the strategy of extrinsically reinforcing the glass with an embedded crystalline phase[3–6]. Macroscopic ductility in BMG-crystalline composite alloys is not inherited directly from the embedded phase but rather by the simultaneous ability of the crystals to catalyze the formation of multiple shear bands at the glass-crystal interface and also to provide barriers that arrest the unstable propagation of a dominant shear band towards catastrophic failure.

Alternatively, it has been proposed that tensile ductility may be achievable in monolithic BMGs by tuning their intrinsic structural heterogeneities[7]. Already, there are a limited number of cases reporting ductility, or at least enhanced plasticity, when a metallic glass is either rapidly quenched during synthesis to freeze in a higher concentration of free volume flow defects, or performing post-synthesis treatment to incorporate "soft" features that promote plastic flow[8–13]. In these previous cases, the nature of the heterogeneities responsible for enhanced plastic behavior is understood to be strictly topological. On the other hand, the influence of compositional inhomogeneity on deformation behavior in monolithic alloys is more ambiguous, although several

studies have suggested correlation between enhanced compressive plasticity and chemical phase separation[14–16]. In contrast to the assumed notion that monolithic BMGs are devoid of microstructural barriers that can stabilize shear bands, it is conceivable that chemical heterogeneities in phase-separated BMGs could contribute to plasticity and toughness by affecting the formation and propagation behavior of shear bands in a manner analogous to the mechanisms at play in BMG-crystalline composite alloys[17].

Dynamic modulus mapping (DMM) results from the previous chapter introduced the possibility of spinodal decomposition occurring in the supercooled liquid of the BMG alloy, $Zr_{58.5}Cu_{15.6}Ni_{12.8}Al_{10.3}Nb_{2.8}$, prior to its glass transition. Intriguingly, an "elastic microstructure" composed of alternating "stiff" and "compliant" regions of submicron dimensions was observed in each of the storage modulus (E_r') maps, but similar contrast indicative of chemical segregation was undetectable when imaged with electron microscopy. Regardless of whether the spatial variations of E_r' measured by DMM is truly due to spinodal decomposition of the supercooled liquid, the fluctuations nonetheless represent features in a "monolithic" BMG that are potentially tunable through different processing routes, to obtain designed microstructures that could optimize the alloy's plasticity and toughness. As discussed in Chapters 3 and 4, an inverse relationship exists between laser heat input and subsequent cooling rate of the melt pool during laser processing. Applying this principle in the present study, we use laser pulse melting combined with DMM to investigate the morphological evolution of the elastic microstructure when processed with various cooling histories.

6.2 Experimental Methods

A 3 mm in diameter rod of $Zr_{58.5}Cu_{15.6}Ni_{12.8}Al_{10.3}Nb_{2.8}$ was prepared by arc melting elemental feedstock with minimum purities of 99.9 at. % in an argon atmosphere, and casting

into a copper mold. The rod was sectioned into 7 cylindrical segments, each 1.6 mm in width. The circular cross sections of the segments were polished with 600 grit SiC paper and sonicated in a methanol bath to remove surface contaminants. Each segment was then pulsed with a laser for a duration of 100 milliseconds at the center position of the polished and cleaned cross section. Laser power was increased from one sample to the next (100 – 220 W) in stepwise increments of 20 W. All laser-pulsed melting was performed within the glovebox of an Optomec MR-7 LENS^{TM}, the same instrument used in the combinatorial studies described in Chapters 3 and 4.

3 μm x 3 μm storage modulus (E_r') maps were collected from the center of the laser-pulsed spots, according to the DMM procedure described in the previous chapter. Following acquisition of each modulus map, a larger (5 μm x 5 μm) topography image was obtained via scanning probe microscopy from the same location to ensure that sample deformation during modulus mapping remained fully elastic. Finally, TEM foils were prepared from each segment by gentle mechanical polishing to a thickness of 30 μm, followed by conventional ion milling until electron transparent. High-resolution TEM was used to verify amorphous structure in each sample.

6.3 Results

Figure 6.1a are DIC microscopy images of the laser-pulsed spots. As expected for an amorphous alloy, the free surface of the melted material appear exceptionally smooth with no detectable surface asperities for the first four spots (100 – 160 W). The spots pulsed with the 180 W and 200 W lasers still maintained smooth topography but with some diffuse features resembling unrelaxed perturbations on the surface of a viscous liquid. The melted spot made with the 220 W laser is decidedly different from the others, displaying regions of wave-like topography. Figure 6.1b shows the corresponding modulus maps, represented as percentage deviations from the mean

value, and Figure 6.1c are the same maps, but each with a rescaled color bar (not shown) relative to the average modulus in each map for maximum visual contrast of the elastic heterogeneities. Figure 6.1d are the accompanying topography images.

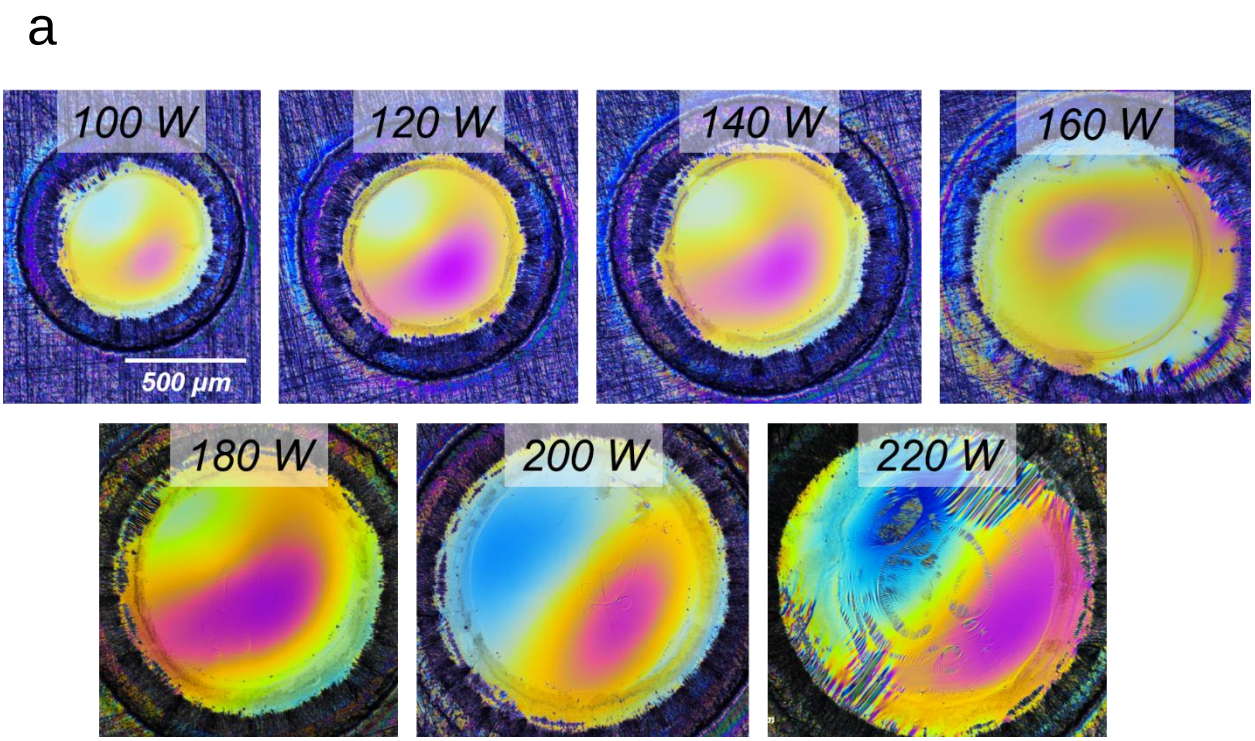

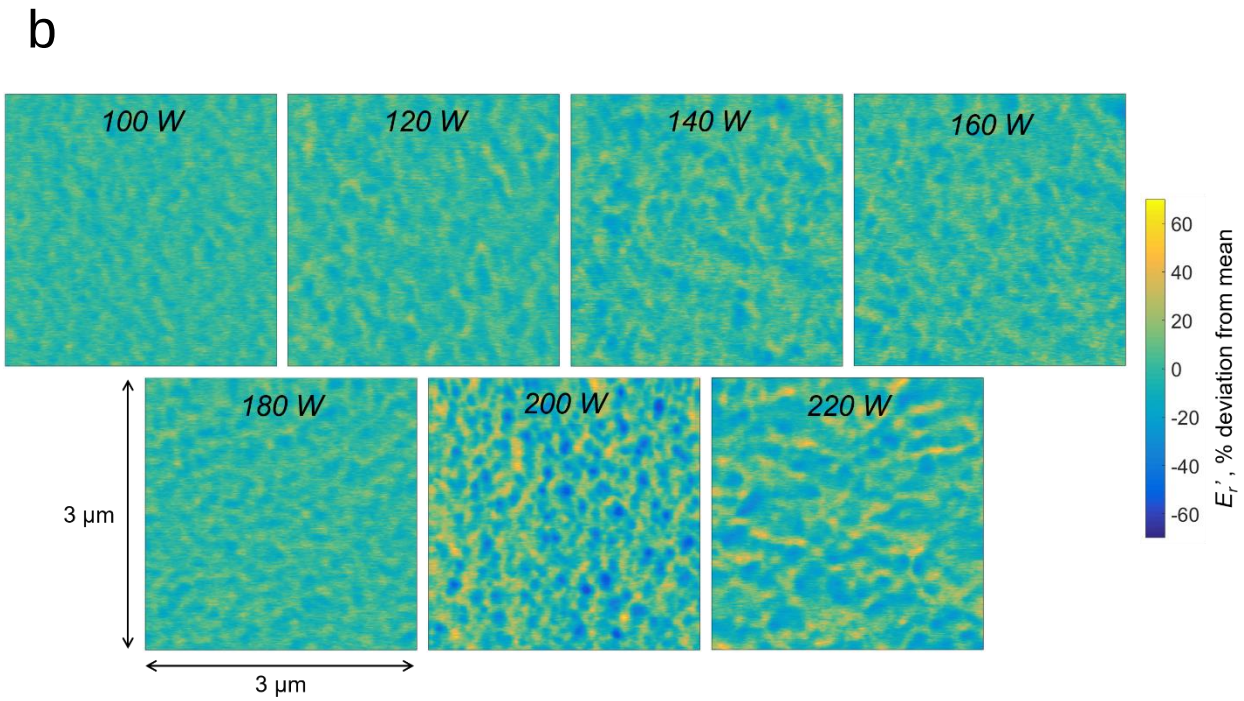

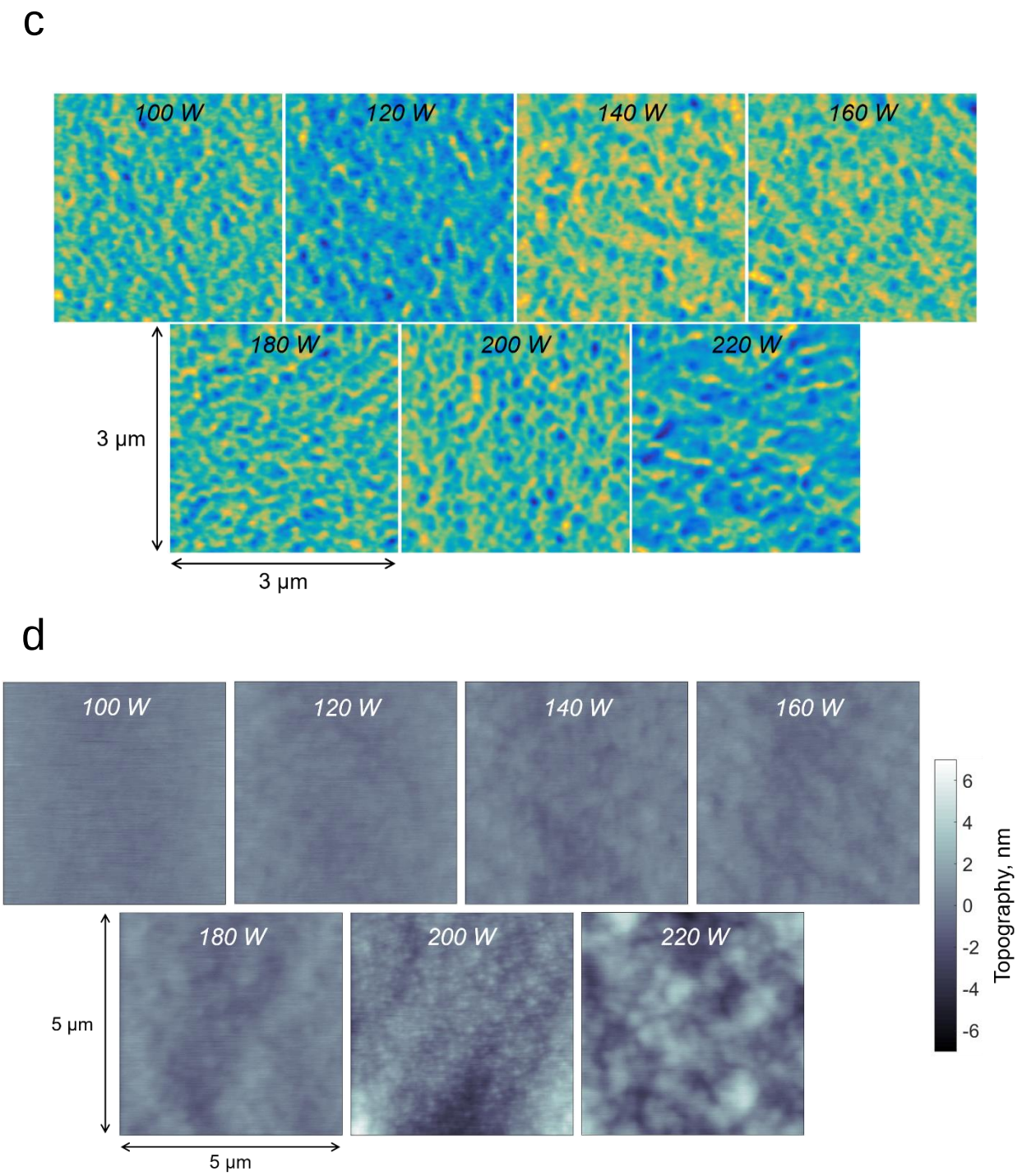

Figure 6.1 (a) DIC images of the laser melted spots. **(b)** 3 µm x 3 µm storage modulus maps, collected from the center of each spot. **(c)** The same maps as in (c) but with a rescaled color representation relative to the average modulus in each map to maximize visual contrast of the elastic features. **(d)** corresponding 5 µm x 5 µm topography maps.

Similar to the modus maps collected from the bulk cast specimen in Chapter 5, elastic microstructures are clearly evident at the center of each of the laser melted spots. Comparing the histograms between the two studies, the statistical spread of normalized E_r' values for the first five samples (100 – 180 W) are considerably narrower than those from the bulk cast specimen, while the final two maps (200 and 200 W) displayed comparable spread (Fig. 6.2a). To assess the evolution of both elastic microstructure and topography with increasing laser heat input, the root mean square (RMS) surface roughness as well as the statistical spread (2σ) of the data in each modulus map are computed (Fig. 6.2b). The trend in both properties exhibit an abrupt increase transitioning from the 180 W sample to the 200 W sample, but neither trend is perfectly correlated with the other; while the topography maps developed sequentially rougher surfaces with increasing heat input from the laser, the statistical spread in normalized E_r' reaches a local maximum at 140 W and again at 200 W. Also noteworthy is the substantially lower RMS roughness of the unpolished laser melted samples compared to the polished cross sections of the bulk specimen described in the previous chapter.

a

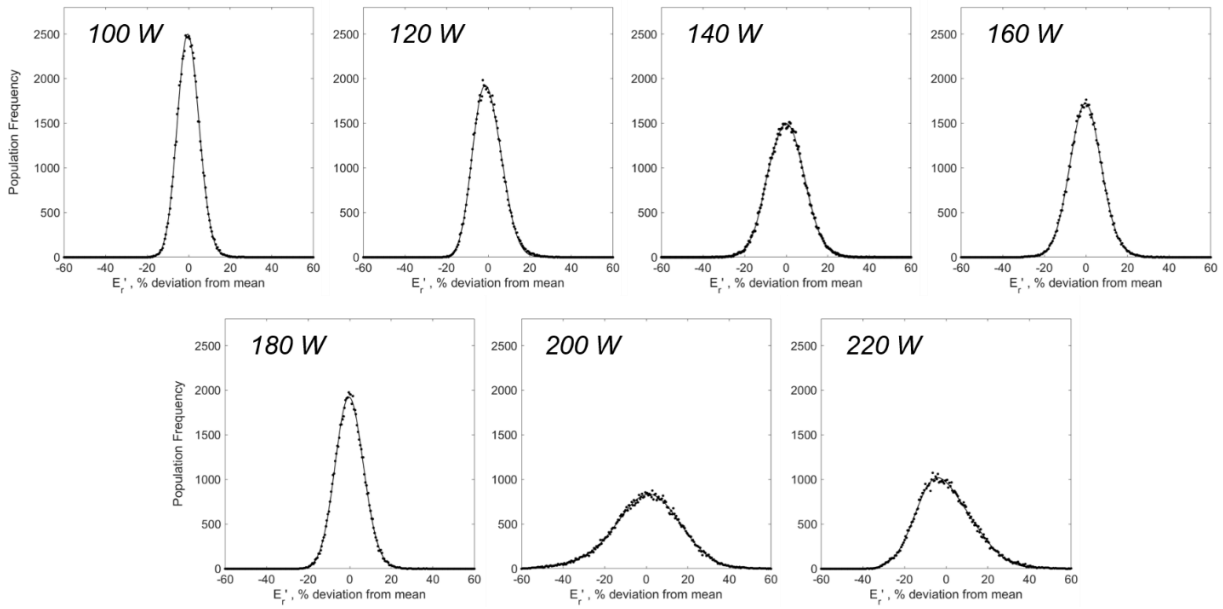

b

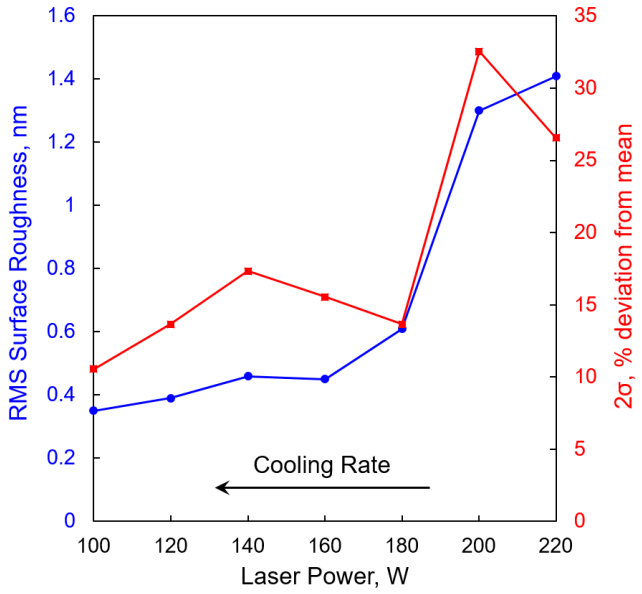

Figure 6.2 (a) Histograms of E_r' for each of the modulus maps, demonstrating the evolution of the extent of heterogeneity in the elastic microstructures with increasing heat input from the laser. **(b)** RMS surface roughness and statistical spread of E_r' (2σ) plotted versus laser power.

Conventional bright field and high resolution TEM confirmed amorphous structure in each of the samples, although crystallinity confined to an isolated location was found in the 200 W sample but not in the following 220 W sample. Further study is necessary to ascertain whether the crystalline features are anomalous or reproducible under the same processing conditions. Again, contrast resembling the elastic features from the modulus maps was not observed. Figure 6.3 provides a selection of HRTEM images from each of the samples, along with their fast Fourier transform (FFT) diffraction patterns.

6.4 Discussion

Using a built-in pyrometer housed within the LENS, we have demonstrated in the multicomponent combinatorial work described in Chapter 4 that processing with higher laser heat input causes lower average cooling rates within the melt pool. In the present work, the BMG samples are treated with a single laser pulse lasting 100 milliseconds, too brief a duration for the

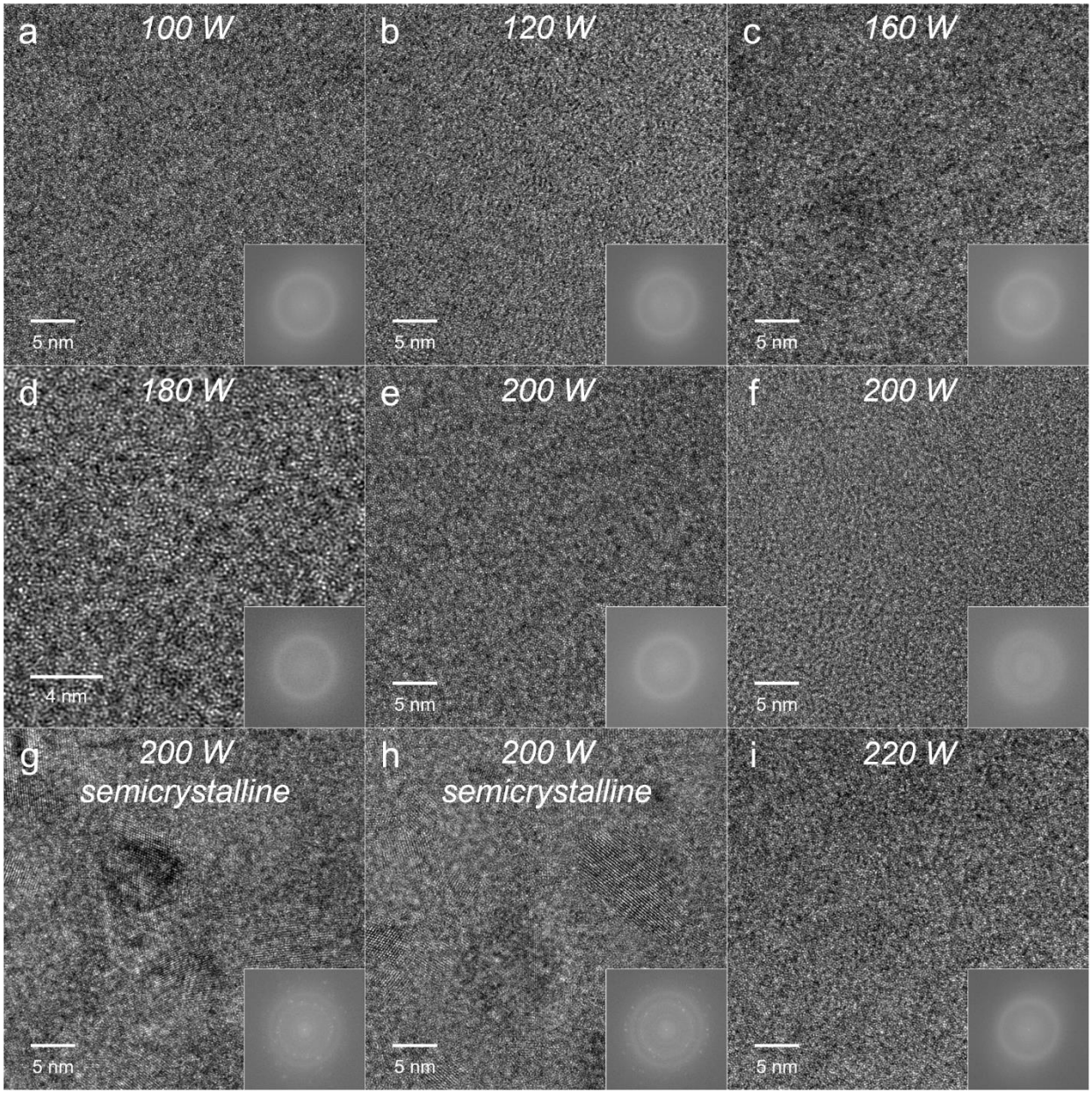

Figure 6.3 A selection of HRTEM images and their respective FFT diffraction patterns (inset). **(a-e, i)** Fully amorphous atomic structures with diffraction patterns showing a diffuse ring at the same radial position in reciprocal space. **(f)** Amorphous structure near a semi-crystalline region found in the sample processed with the 200 W laser; note that an additional diffuse ring appears in the diffraction pattern. **(g-h)** Nano-crystals embedded in an amorphous matrix; two diffuse rings are clearly visible along with diffraction spots from the crystalline reflections.

pyrometer to capture the temporal progression of the temperature profile. Although the quantitative details of heating and cooling history were not actually measured, the inverse relationship between laser heat input and cooling rate can still be applied to qualitatively establish the "causal" effect of decreasing cooling rate on the elastic microstructure in the BMG. In general, metallic glasses synthesized with higher cooling rates are understood to be topologically less relaxed, possessing more quenched-in free volume, and are therefore structurally more heterogeneous[7,18–20]. Fan *et al*. carried out molecular dynamics studies to investigate the effect of quench rate on the statistical distribution of atomic-level shear modulus[21]; the simulated glass created with a lower quench rate resulted in a narrower, or less heterogeneous, distribution of local shear modulus. Similarly, Liu *et al*. reported reduced spatial variability in the viscoelastic properties of a thin-film metallic glass when annealed to a more relaxed state[22]. Our nanoindentation and DMM work described in the previous chapter also demonstrated reduced heterogeneity, presumably due to structural relaxation processes that occur during sub-T_g annealing.

The expected evolution towards a more homogeneous material when processed with progressively lower cooling rates, or larger heat input, is not observed in the laser-pulsed samples. On the contrary, the mapping data shows that the magnitude of elastic non-uniformity, quantified here as 2σ, becomes generally more severe with increasing laser power (Fig. 6.2b), leading us to suspect that topological heterogeneities from quenched-in free volume do not constitute the primary source of the observed fluctuations in E_r'. Alternatively, we propose that spinodal decomposition, which spontaneously amplifies preexisting compositional variations over time, is more likely to be the dominant mechanism responsible for the contrasting features seen in the modulus maps. However, between 140 W and 180 W and also beyond 200 W, 2σ deviates from

the dominant trend by decreasing slightly with additional increments of heat input. Assuming the degree of heterogeneity in each 3 μm x 3 μm modulus map is an accurate representation of the average microstructure within the melted volume of material, a possible explanation for the deviatory behavior of 2σ is the opposite effects of cooling rate on the severity of topological versus compositional heterogeneity in the glass. Slower cooling permits more time for spinodal decomposition to evolve compositional heterogeneities in the undercooled liquid, but would also expectedly produce topologically relaxed (homogeneous) atomic-level structures. Conversely, rapid quenching preserves topological heterogeneities but would prevent the development of phase separated microstructures. According to this line of reasoning, both compositional and topological heterogeneity contribute to the overall spread of the mapping data, although the results in this study seem to indicate that the former type is more prevailing on the length scales probed by DMM.

In view of the discussion on spinodal decomposition, it is worthwhile to consider why phase separation would transpire in the Zr-based alloy explored in this work. Phase separation in monolithic metallic glasses have been reported[14,16,23–26], but most often for cases where the pairwise enthalpy of mixing (ΔH_{mix}) is positive for at least one of the elemental pairs, resulting in a pronounced liquid miscibility gap at undercooled temperatures. For the vast majority of existing BMG alloys, including the alloy of the present study, ΔH_{mix} between the major components tend to be strongly negative, seemingly ruling out the possibility of spinodal decomposition. While a positive ΔH_{mix} may be required for a liquid miscibility gap to develop in binary alloys, for multicomponent alloys, the enthalpic preference of one atomic species to be surrounded by another is not equally shared among all elemental pairs in the alloy; for example, ΔH_{mix} in the A-B-C ternary system between A and B atoms may be more negative than between A and C atoms. At high temperatures, where there is an entropic advantage to have a homogeneous liquid, phase

separation is unlikely. But at the deep liquid undercoolings experienced by many multicomponent BMGs, the Gibb's free energy of the liquid is governed by configurational enthalpy rather than entropy, and the emergence of a non-equilibrium miscibility gap is certainly plausible[24,27]. Our consistent discovery of similar "elastic microstructures" in several other well-known Zr-based BMGs that do not possess substantially positive ΔH_{mix} among any of the elemental pairs suggests that spinodal decomposition may be more prevalent in multicomponent BMGs than previously recognized by the research community.

To evaluate the morphological evolution of the elastic microstructures with cooling rate, characteristic feature lengths (L_c) are extracted from computed autocorrelation functions associated with each modulus map. The average L_c was 150 nm, similar to the coarseness of the elastic microstructures reported for the bulk cast specimen in Chapter 5. Furthermore, no obvious correlation or scaling is found between the applied heat input and L_c (Fig. 6.4).

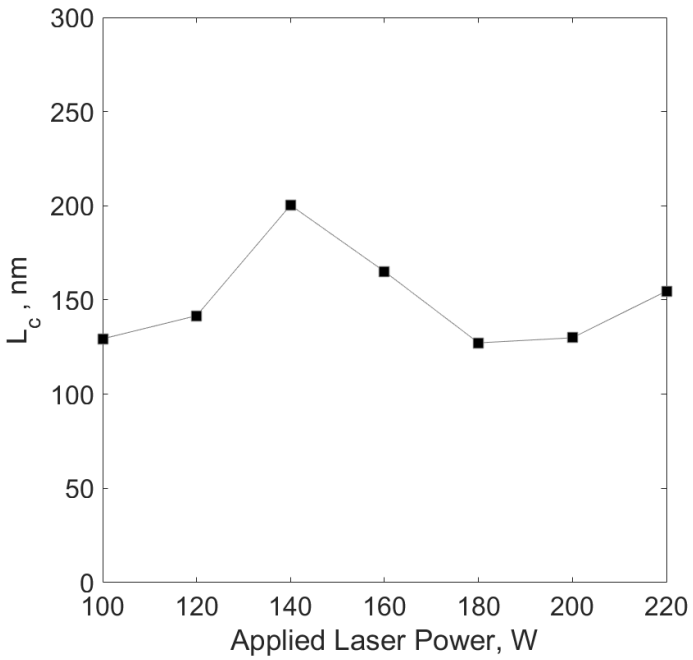

Figure 6.4 The characteristic length L_c of the elastic fluctuations in each modulus map, plotted against the laser power. L_c is extracted from the autocorrelation functions derived for each map, according to the method described in Chapter 5.

Based on the Cahn and Hilliard's theoretical formulation on spinodal decomposition[28–31], coarsening of the phase-separated features occurs over time but most rapidly in the later stages of the process; prior to significant coarsening, the evolution of spinodal patterns involves mainly amplification of the compositional fluctuations. It is possible that the temporal regime over which the decomposition transpired in the laser-pulsed spots was confined to the earlier stages of development due to rapid cooling. Further investigation is necessary to determine whether significant coarsening can be achieved, either by further increasing laser heat input or performing isothermal annealing above T_g for an extended duration.

6.5 Conclusions

To summarize, single pulse laser melting was carried out to investigate the dependence of elastic microstructure in $Zr_{58.5}Cu_{15.6}Ni_{12.8}Al_{10.3}Nb_{2.8}$ to different heating and cooling histories. Unlike topological heterogeneities, which become more prevalent with increasing cooling rates, the interconnected elastic microstructures measured by DMM displayed the opposite trend, becoming more heterogeneous with lower cooling rates (higher heat input), reinforcing the notion of chemical phase separation in the form of spinodal decomposition as the main cause of the prominent features observed in the modulus maps. Actual details of the trend suggests that although phase separation may be the dominant mechanism of elastic heterogeneity on length scales accessible to DMM, the contribution of topological heterogeneities cannot be ignored. Whether phase-separated elastic microstructure can substantially improve (or degrade) the mechanical deformation behavior of BMGs remains to be explored.

6.6 References

1. Demetriou, M. D. *et al.* A damage-tolerant glass. *Nat. Mater.* **10,** 123–8 (2011).

2. Xu, J. & Ma, E. Damage-tolerant Zr–Cu–Al-based bulk metallic glasses with record-breaking fracture toughness. *J. Mater. Res.* **29,** 1489–1499 (2014).

3. Hays, C., Kim, C. & Johnson, W. Microstructure Controlled Shear Band Pattern Formation and Enhanced Plasticity of Bulk Metallic Glasses Containing in situ Formed Ductile Phase Dendrite Dispersions. *Phys. Rev. Lett.* **84,** 2901–2904 (2000).

4. Hofmann, D. C. *et al.* Development of tough, low-density titanium-based bulk metallic glass matrix composites with tensile ductility. *Proc. Natl. Acad. Sci.* **105,** 20136–20140 (2008).

5. Hofmann, D. C. *et al.* Designing metallic glass matrix composites with high toughness and tensile ductility. *Nature* **451,** 1085–9 (2008).

6. Launey, M. E., Hofmann, D. C., Johnson, W. L. & Ritchie, R. O. Solution to the problem of the poor cyclic fatigue resistance of bulk metallic glasses. *Proc. Natl. Acad. Sci.* **106,** 4986–91 (2009).

7. Ma, E. & Ding, J. Tailoring structural inhomogeneities in metallic glasses to enable tensile ductility at room temperature. *Mater. Today*, in press (2016).

8. Liontas, R. *et al.* Substantial tensile ductility in sputtered Zr-Ni-Al nano-sized metallic glass. *Acta Mater.* **118,** 270–285 (2016).

9. Wang, X. L. *et al.* Plasticity of a scandium-based nanoglass. *Scr. Mater.* **98,** 40–43 (2015).

10. Ketov, S. V *et al.* Rejuvenation of metallic glasses by non-affine thermal strain. *Nature* **524,** 200–203 (2015).

11. Song, K. K. *et al.* Significant tensile ductility induced by cold rolling in Cu47.5Zr47.5Al5 bulk metallic glass. *Intermetallics* **19,** 1394–1398 (2011).

12. Scudino, S., Jerliu, B., Surreddi, K. B., Kühn, U. & Eckert, J. Effect of cold rolling on compressive and tensile mechanical properties of Zr52.5Ti5Cu18Ni14.5Al10 bulk metallic glass. *J. Alloys Compd.* **509,** 5–8 (2011).

13. Wang, Q. *et al.* Superior tensile ductility in bulk metallic glass with gradient amorphous structure. *Sci. Rep.* **4,** 4757 (2014).

14. Yao, K. F., Ruan, F., Yang, Y. Q. & Chen, N. Superductile bulk metallic glass. *Appl. Phys. Lett.* **88,** 23–26 (2006).

15. Chen, N., Zhang, H. & Yao, K.-F. Structural heterogeneity in a binary Pd–Si metallic glass. *Philos. Mag. Lett.* **95,** 77–84 (2015).

16. Oh, J. C., Ohkubo, T., Kim, Y. C., Fleury, E. & Hono, K. Phase separation in

Cu43Zr43Al7Ag7 bulk metallic glass. *Scr. Mater.* **53,** 165–169 (2005).

17. Wang, Y., Li, M. & Xu, J. Toughen and harden metallic glass through designing statistical heterogeneity. *Scr. Mater.* **113,** 10–13 (2016).

18. Zhu, Z.D., Ma, E. & Xu, J. Elevating the fracture toughness of Cu49Hf42Al9 bulk metallic glass: Effects of cooling rate and frozen-in excess volume. *Intermetallics* **46,** 164–172 (2014).

19. Wakeda, M., Saida, J., Li, J. & Ogata, S. Controlled rejuvenation of amorphous metals with thermal processing. *Sci. Rep.* **5,** 10545 (2015).

20. Saida, J., Yamada, R. & Wakeda, M. Recovery of less relaxed state in Zr-Al-Ni-Cu bulk metallic glass annealed above glass transition temperature. *Appl. Phys. Lett.* **103,** 1–5 (2013).

21. Fan, Y., Iwashita, T. & Egami, T. Evolution of elastic heterogeneity during aging in metallic glasses. *Phys. Rev. E* **89,** 062313:1–7 (2014).

22. Liu, Y. H. *et al.* Characterization of nanoscale mechanical heterogeneity in a metallic glass by dynamic force microscopy. *Phys. Rev. Lett.* **106,** 125504:1–4 (2011).

23. Mattern, N. *et al.* Spinodal decomposition of Ni-Nb-Y metallic glasses. *Acta Mater.* **57,** 903–908 (2009).

24. Busch, R., Schneider, S., Peker, A. & Johnson, W. L. Decomposition and primary crystallization in undercooled Zr 41.2Ti13.8Cu12.5Ni10.0Be 22.5 melts. *Appl. Phys. Lett.* **67,** 1544-1546 (1995).

25. Park, E. S. & Kim, D. H. Phase separation and enhancement of plasticity in Cu-Zr-Al-Y bulk metallic glasses. *Acta Mater.* **54,** 2597–2604 (2006).

26. Park, B. J. *et al.* Phase separating bulk metallic glass: A hierarchical composite. *Phys. Rev. Lett.* **96,** 245503:1–4 (2006).

27. Johnson, W. L. Bulk Glass-Forming Metallic Alloys : Science and Technology. *MRS Bull.* **24,** 42–56 (1999).

28. Cahn, J. W. Phase Separation by Spinodal Decomposition in Isotropic Systems. *J. Chem. Phys.* **42,** 93–99 (1965).

29. Cahn, J. W. & Hilliard, J. E. Spinodal Decomposition: A Reprise. *Acta Metall.* **19,** 151–161 (1971).

30. Rundman, K. B. & Hilliard, J. E. Early stages of spinodal decomposition in an aluminum-zinc alloy. *Acta Metall.* **15,** 1025–1033 (1967).

31. Cahn, J. W. The Later Stages of Spinodal Decomposition and the Beginnings of Particle Coarsening. *Acta Metall.* **14,** 1685–1692 (1966).

Chapter 7

Quantifying the Intrinsic Plasticity of Bulk Metallic Glasses Through Instrumented Nanoindentation

7.1 Introduction

The clear benefit of instrumented nanoindentation lies in its ability to accurately characterize mechanical properties, namely hardness (H) and indentation modulus (E_r), by probing very small volumes of material. However, beyond providing H and E_r values, the load-displacement (P-h) curves acquired during nanoindentation may themselves offer valuable insight with respect to the deformation characteristics of the material at hand. For example, Schuh *et al.* conducted extensive nanoindentation experiments on bulk metallic glasses under a variety of loading conditions; it was discovered that at sufficiently slow loading rates, the plastic deformation could be entirely accounted for by sudden depth excursions (i.e. pop-ins) corresponding to individual shear band events[1,2]. Notably, another study used spherical indenter tips to study the statistical variability of the applied load at the first pop-in in a BMG, and then correlated the results with the concentration of flow defects in the alloy[3].

In the present study, we employ P-h curves to analyze the work energy expended by a diamond Berkovich indenter tip during nanoindentation. The total work of indentation (W_{tot}) is simply the area under the loading portion of the curve (Fig. 7.1). The area beneath the unloading portion represents the total elastic energy (W_{el}) stored within the material, and the energy dissipated by plastic deformation is given by $W_{pl} = W_{tot} - W_{el}$. We hypothesize that the ratio $R_{pl} = W_{pl}/W_{tot}$ serves as a general figure of merit for quantifying the intrinsic plasticity of a material and can be

used to differentiate between "ductile" and brittle BMGs. To test this hypothesis, we first computed R_{pl} for a large number of existing indentation curves from our database of previous measurements. Following the preliminary analysis, nanoindentation was performed on a cast specimen of $Zr_{58.5}Cu_{15.6}Ni_{12.8}Al_{10.3}Nb_{2.8}$ that was systematically annealed below T_g to investigate whether R_{pl} is sensitive to the deterioration of plasticity caused by the annihilation of free volume.

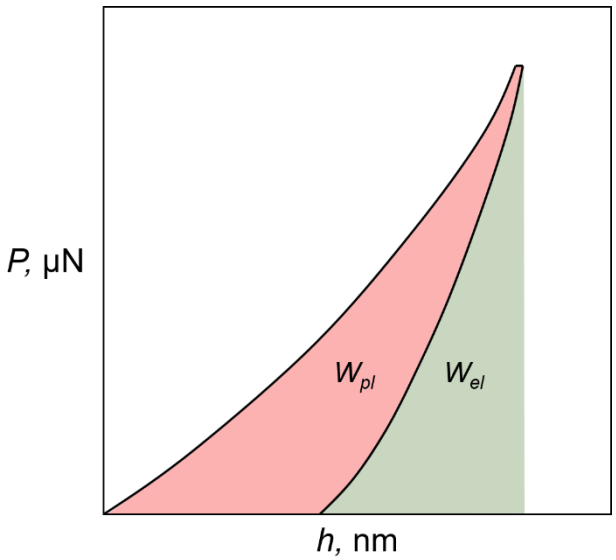

Figure 7.1 Schematic nanoindentation load-displacement curve illustrating the plastic and elastic portions of the total work energy.

7.2 Experimental Methods

A 1 mm thick disc was prepared from a 3 mm diameter rod of $Zr_{58.5}Cu_{15.6}Ni_{12.8}Al_{10.3}Nb_{2.8}$, produced by arc-melting pure (> 99.9 at. %) constituents together in an argon-filled atmosphere and casting into a copper mold. One side of the disc was polished to a mirror finish with 20 nm colloidal silica prior to performing nanoindentation measurements. 100 evenly-spaced indents in a square array were performed at the central location of the polished surface, within a square area measuring 72 μm x 72 μm. A maximum load of 8 mN and loading rate of 1.6 mN/s were used for

each indent, with a two second hold at maximum load before unloading. The specimen was subsequently annealed for 1 hour at 370 ˚C ($0.95T_g$) and then lightly polished with colloidal media to remove the markings from the previous set of indents as well as surface oxide that may have formed during annealing. The same nanoindentation measurements were performed on the annealed specimen. Finally, the indentation measurements were repeated twice more, each following an additional hour of annealing. The experimental methods employed for all data collected previously but analyzed presently has already been described in previous chapters and will not be repeated here.

7.3 Results

7.3.1 Aluminum, silicon, and fused silica

R_{pl} calculated from a number of indents performed on single-crystal aluminum, single-crystal silicon wafer grown in the <100> direction, and fused silica displayed the expected ranking of values according to the plasticity of the indented material. Figure 7.2 provides representative *P-h* curves for all three disparate materials. Aluminum, a ductile metal, exhibited the largest R_{pl}, 0.925 ± 0.011. In comparison, the R_{pl} of silicon and fused silica, both brittle materials, were much lower, 0.416 ± 0.003 and 0.292 ± 0.001, respectively.

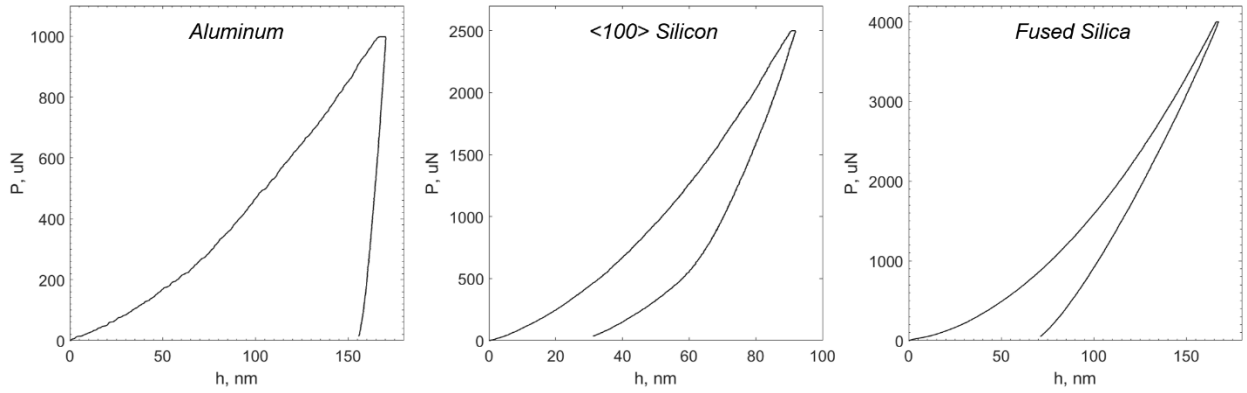

Figure 7.2 Representative load-displacement curves from three mechanically disparate materials. As expected, plastic work dominates the total work of indentation in aluminum, a ductile metal.

7.3.2 Zr-based BMG, as-cast and annealed

Analysis of the 1000 indentation curves (500 as-cast and 500 post-anneal) collected from the Zr-based BMG specimens of the work described in Chapter 5 showed a reduction in the average R_{pl} from 0.590 to 0.576 as a result of annealing at 370 ˚C for two hours. Figure 7.3 shows the histogram distributions of R_{pl} and its Gaussian fit for the two sets of curves. In addition to shifting the average R_{pl}, note that annealing broadened and stretched the distribution towards lower values. As a reminder, the maximum load used for the measurements was 1.5 mN and the loading rate was fixed at 0.3 mN/s.

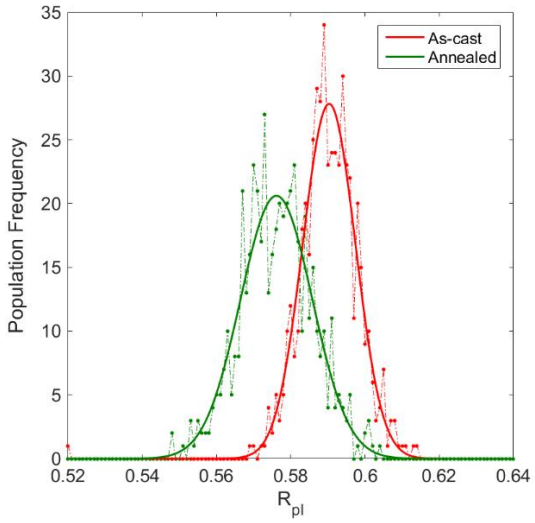

Figure 7.3 The statistical distribution of R_{pl} for the two sets of indentation curves (as-cast and annealed at $0.95T_g$ for two hours) collected from the Zr-based BMG samples of the work described in Chapter 5.

7.3.3 Systematic study on the effect of sub-Tg annealing on R_{pl}

Figure 7.4a is a plot of H versus E_r for the BMG sample described in the experimental methods section. Similar to the results reported in Chapter 5, each set of indentation data display a linear scaling of the two properties. Aside from the final set of data, measured after 3 hours of annealing, the average H and E_r progressively shift to higher values along a shared trend line with

increments of annealing time. It is suspected that the unexpected reduction in the measured properties for the most relaxed state of the glass is an artifact of poor specimen adhesion to the magnetic mounting discs that were used in the experiments. To verify whether such was the case, another specimen was indented, removed, and reattached to the mounting disc before repeating the indentation measurements at the same location; the result was again an artificial shift in the values. It is inconclusive whether the earlier measurements (as-cast, 1-hour, and 2-hour anneal) were also negatively influenced by poor adhesion effects. Figure 7.4b and c show the statistical distributions of R_{pl} and progression of its average value with annealing time. The *P*-*h* curves collected after the final annealing was deemed incorrect and hence excluded from the analysis.

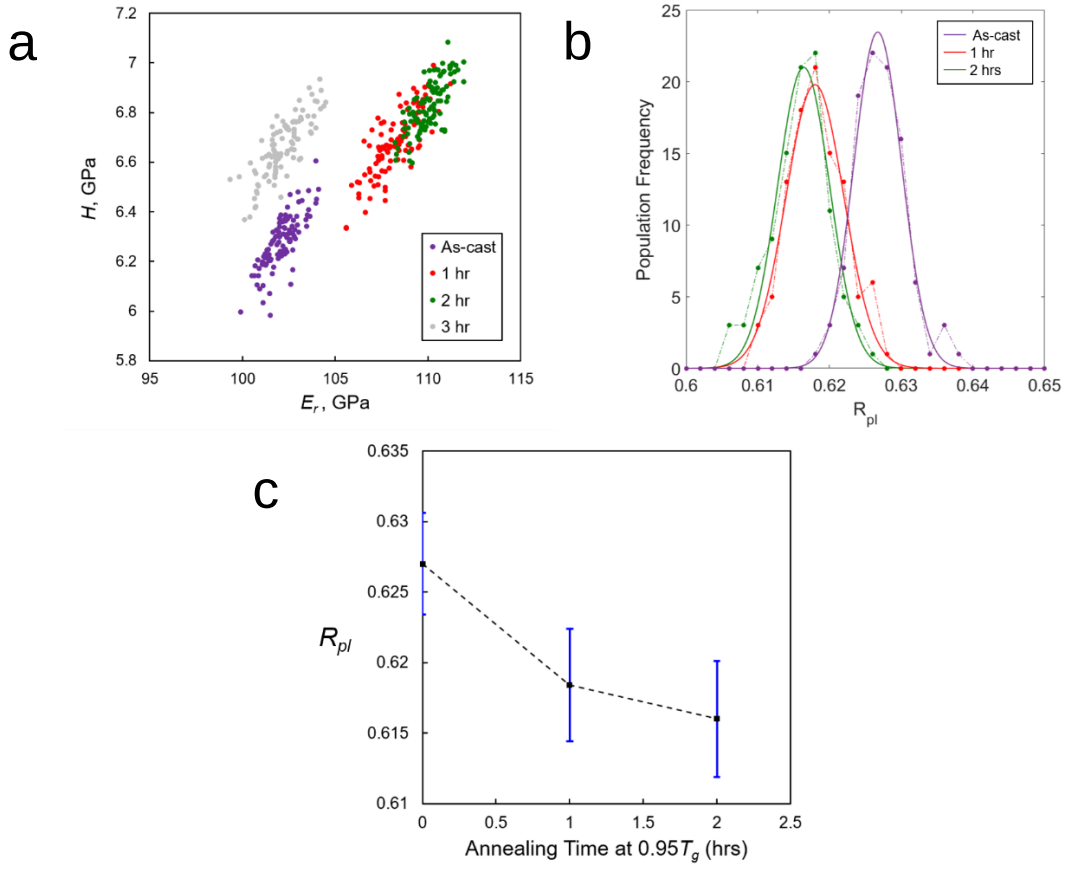

Figure 7.4 (a) H vs E_r for the Zr-based BMG sample that was incrementally annealed at $0.95T_g$ up to 3 hours. **(b)** Histograms of R_{pl} calculated from the indentation curves. **(c)** Average R_{pl} as a function of annealing time. Error bars are the standard deviations, $\pm\sigma$.

7.3.4 Revisitation of Cu-Zr-Ti Metallic Glass Data

Recall that in the high-throughput work described in Chapter 4, indents were performed on 92 distinct amorphous compositions in the Cu-Zr-Ti ternary system. Contour plots of H and E_r versus composition showed property-composition trends that offered insight into possible relationships between the observed trends and glass forming ability. We analyzed all curves generated from the study and constructed a contour plot of R_{pl}, shown in Figure 7.5 along with the H and E_r plots for comparison.

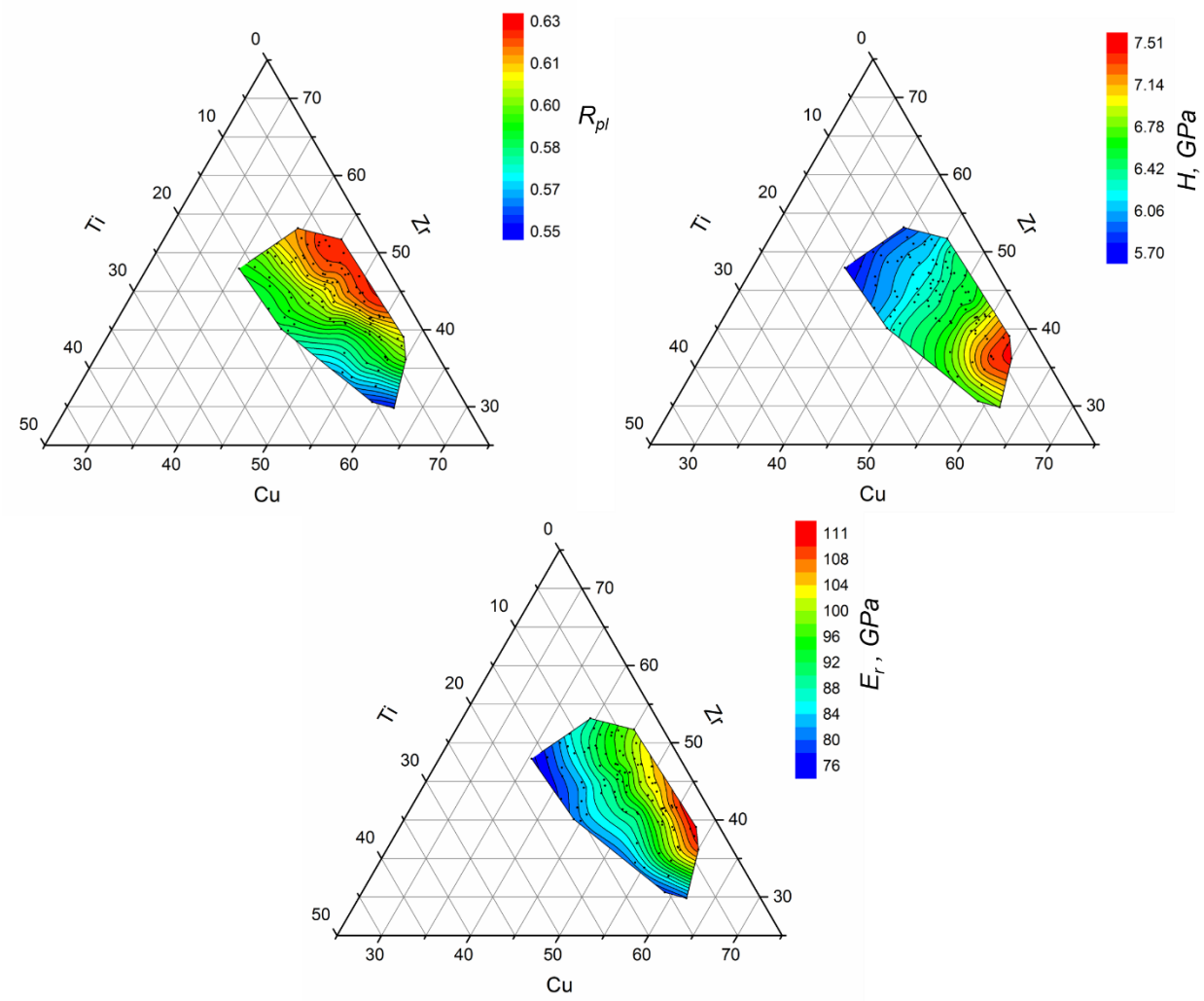

Figure 7.5 Property-composition contour plots of R_{pl}, H, and E_r for alloys belonging to the ternary Cu-Zr-Ti system.

7.4 Discussion

According to Griffith's energy balance equation in fracture mechanics theory, the fracture toughness of a brittle material is a direct consequence of the competition between the energy cost of creating new surfaces via crack advancement and the benefit of relaxing the stored elastic strain energy in the vicinity of a free surface. Irwin modified the theory by showing that plastic deformation occurring ahead of the crack tip diminishes the thermodynamic driving force for crack growth; in ductile materials such as steel, the ability to dissipate the stored elastic energy by plastic deformation leads to higher fracture toughness values. The same principles by way of analogy may apply during nanoindentation, where the sharp tip of the indenter, rather than a crack tip, acts as the stress concentrator. As the applied load increases, the work energy is either stored elastically or dissipated by plastic deformation processes. It is reasonable then to expect that the intrinsic plasticity of a material is reflected in the balance of the elastic and plastic contributions to the total work energy of indentation; the greater the latter contribution, quantified here as R_{pl}, the more "plastic" a material is. The ranking of R_{pl} in the comparison of aluminum, silicon, and fused silica is in excellent agreement with this proposed line of reasoning.

We note that a previous study also evaluated R_{pl} for a Zr-based BMG, both in the as-cast condition and after uniaxial compression to large plastic strains[4]. It was discovered that R_{pl} increased significantly after compression of the glass, indicating an enhancement of plasticity. Furthermore, indenting with higher applied loads also produced larger R_{pl} values. The authors suggested that deformation-induced phase separation or nanocrystallization to be responsible for the enhancement of plastic behavior, but we suspect structural rejuvenation to be the more plausible cause. Just as sub-T_g annealing can induce embrittlement by the annihilation of excess free volume in a metallic glass, recent studies have demonstrated that a glass can also be

"rejuvenated" to a state of greater intrinsic plasticity through various mechanical treatments, including cold-working[5–10].

The validity of R_{pl} as a figure of merit for evaluating the plasticity of BMGs is further revealed through analysis of the indentation curves from the experiments described in Chapter 5. It is particularly noteworthy that the respective distributions of R_{pl} in Figure 7.3 differ not only in average value but also in width, with the annealed distribution overlapping that of the as-cast sample but also extending to lower values. Similar to H and E_r, the statistical spread in R_{pl} indicates that plasticity is not spatially uniform on the micrometer length scale. That the BMG retained some regions of higher plasticity ($R_{pl} > 0.6$) after the two-hour anneal at $0.95T_g$ implies incomplete structural relaxation, the process in which loosely packed atomic configurations in the glass are converted to topologically relaxed arrangements.

The primary objective of the systematic annealing experiments carried out in the present study is to investigate whether the measured distributions of R_{pl} can capture the details of the process of embrittlement in metallic glasses. The extent of structural relaxation is most often quantified in terms of the relaxation enthalpy or excess volume[7,11,12]; however, these quantities are averaged properties of the glass as a whole, and do not inform how the spatial variations of structure is evolving during relaxation in the heterogeneous material. Evaluating R_{pl} for arrays of evenly spaced indents would allow assessment of both the global plasticity (average R_{pl}) as well as the local distribution of plasticity in the glass throughout the relaxation process. Unfortunately, while the trends in Figure 7.4 show reduced R_{pl} with increments of annealing time, there is the possibility that the results were negatively affected by lack of proper sample adhesion to the mount, as mentioned in the results section. For future experiments, thicker BMG specimens with larger

surface area will be used to avoid measuring undesired compliance from imperfect sample adhesion.

In the previous discussion concerning the H– and E_r –composition trends for the Cu-Zr-Ti ternary system, it was proposed based on comparison of the two plots that intrinsic plasticity of the alloys may be strongly sensitive to the copper content. Intriguingly, the R_{pl} contour plot suggests that plasticity, like E_r, is sensitive mainly to titanium content but favors lower Cu:Zr molar ratios, still consistent with results from computational studies on the binary Cu-Zr system[13]. As of now, it is ambiguous which interpretation is correct, prompting further experimental work for the future. A rational approach would be to measure the attainable plastic strain in compression for various compositions within the contour plots, and subsequently determine which property trend among the three is most consistent with the direct measurements of plasticity.

7.5 References

1. Schuh, C. A. & Nieh, T. G. A nanoindentation study of serrated flow in bulk metallic glasses. *Acta Mater.* **51,** 87–99 (2003).
2. Schuh, C. A. & Nieh, T. G. A survey of instrumented indentation studies on metallic glasses. *J. Mater. Res.* **19,** 46–57 (2011).
3. Li, W., Gao, Y. & Bei, H. On the correlation between microscopic structural heterogeneity and embrittlement behavior in metallic glasses. *Sci. Rep.* **5,** 14786 (2015).
4. Fornell, J., Suriñach, S., Baró, M. D. & Sort, J. Indentation plastic work and large compression plasticity in in situ nanocrystallized Zr62Cu18Ni10Al10 bulk metallic glass. *J. Alloys Compd.* **509S,** S87–S91 (2011).
5. Scudino, S., Jerliu, B., Surreddi, K. B., Kühn, U. & Eckert, J. Effect of cold rolling on compressive and tensile mechanical properties of Zr52.5Ti5Cu18Ni14.5Al10 bulk metallic glass. *J. Alloys Compd.* **509,** 5–8 (2011).
6. Song, K. K. *et al.* Significant tensile ductility induced by cold rolling in Cu 47.5Zr47.5Al5 bulk metallic glass. *Intermetallics* **19,** 1394–1398 (2011).
7. Ketov, S. V *et al.* Rejuvenation of metallic glasses by non-affine thermal strain. *Nature* **524,** 200–203 (2015).

8. Scudino, S. *et al.* Ductile bulk metallic glasses produced through designed heterogeneities. *Scr. Mater.* **65,** 815–818 (2011).

9. Li, B. S., Shakur Shahabi, H., Scudino, S., Eckert, J. & Kruzic, J. J. Designed heterogeneities improve the fracture reliability of a Zr-based bulk metallic glass. *Mater. Sci. Eng. A* **646,** 242–248 (2015).

10. Stolpe, M., Kruzic, J. J. & Busch, R. Evolution of shear bands, free volume and hardness during cold rolling of a Zr-based bulk metallic glass. *Acta Mater.* **64,** 231–240 (2014).

11. Wakeda, M., Saida, J., Li, J. & Ogata, S. Controlled rejuvenation of amorphous metals with thermal processing. *Sci. Rep.* **5,** 10545 (2015).

12. Gallino, I., Shah, M. B. & Busch, R. Enthalpy relaxation and its relation to the thermodynamics and crystallization of the Zr58.5Cu15.6Ni12.8Al10.3Nb2.8 bulk metallic glass-forming alloy. *Acta Mater.* **55,** 1367–1376 (2007).

13. Xu, J. & Ma, E. Damage-tolerant Zr–Cu–Al-based bulk metallic glasses with record-breaking fracture toughness. *J. Mater. Res.* **29,** 1489–1499 (2014).

Chapter 8
Conclusions

8.1 Summary

The research presented in this thesis are of two major sections. The first detailed the development of a high-throughput methodology involving laser deposition for the exploration of GFA, as well as property-composition relationships, in metallic glass forming systems. For proof of concept, compositionally graded specimens in the Cu-Zr binary system were fabricated. By processing the continuous range of compositions in the specimens with a different laser powers, and therefore different cooling rates, the two best known glass formers in the system, $Cu_{64}Zr_{36}$ and $Cu_{50}Zr_{50}$, were deduced. Following the success of the binary work, the methodology was extended to interrogate the glass forming landscape of a multicomponent alloy system. Ternary Cu-Zr-Ti composition libraries were fabricated using a three-layered deposition scheme to incorporate two independent composition gradients into a single library, one of continuously varying Cu:Zr molar ratio and the other of increasing titanium content. By fabricating a series of Cu-Zr-Ti composition libraries, each processed with sequentially higher laser heat input, continuous regions of glass formation associated with each processing condition were defined. Further analysis led to the discovery of a new glass former in the ternary system that exhibited superior GFA compared to previously reported BMGs in the Cu-Zr-Ti system. Recognizing that the mechanical properties of BMGs are also important in addition to GFA, an alternative fabrication scheme was developed to synthesize “discrete dot” composition libraries suitable for the rapid surveying of mechanical properties via nanoindentation. Noted differences in the resulting property-composition trends of

hardness and modulus shed light on the possible existence of structurally-distinct domains in composition space.

The second major section of this thesis involved studies to investigate the microstructural details of a Zr-based BMG alloy. The work was motivated by recent discoveries of nanoscale structural heterogeneities in monolithic BMGs and the significance of their existence to the macroscopic deformation behavior of the material. In the first set of experiments, instrumented nanoindentation and dynamic modulus mapping were employed to probe mechanical property variations within a cast cylindrical rod specimen. The nanoindentation results indicated significant micron-scale variations of both hardness and indentation modulus. Dynamic modulus mapping performed over smaller areas (3 μm x 3 μm) revealed an "elastic microstructure" composed of interconnected submicron features in the fully amorphous BMG. Furthermore, prominent circumferential alignment of the features to the edge of the circular cross sections was observed, the characteristics of which have never been reported before for metallic glasses. Sub-T_g annealing treatment slightly narrowed the statistical spread of the mapped data but the defining heterogeneous features were preserved in the process. Based on the results, it was argued that the salient features in the elastic microstructure may primarily be caused by spinodal decomposition in the supercooled liquid prior to the glass transition. In a separate study, DMM was performed on a series of laser melted spots created on the same alloy. Again, similar elastic microstructures were observed, but the amplitude of the fluctuations increased with increasing laser heat input (decreasing cooling rate) while the characteristic features size of the fluctuations remained approximately unchanged. These observations were consistent with the expected development of spinodal microstructure according to Cahn and Hilliard's theoretical formulation of the non-equilibrium phase separation mechanism.

The final segment of the dissertation involved retrospective analysis of the nanoindentation load-displacement curves collected throughout the thesis work. Specifically, the plastic work ratio R_{pl}, defined as the ratio of the plastic work of indentation to the total work, was computed from the respective area beneath the loading (elastic and plastic) and unloading (elastic) portions of the curves. Surveyed analysis of load-displacement data from a wide variety of materials (including the metallic glass alloys of nanoindentation experiments performed earlier) suggested R_{pl} as a robust figure of merit for quantifying intrinsic plasticity. Moreover, similar to the heterogeneous distribution of hardness and modulus observed for the Zr-based BMG, the distribution of R_{pl} was also found to be heterogeneous. Consequently, a systematic annealing study of the alloy was carried out in an attempt to determine whether the distribution of R_{pl} evolves with the expected loss of plasticity (embrittlement) that accompanies the gradual annihilation of free volume; the preliminary results were promising and provide a foundation for more thorough investigation in the future.

8.2 Future Outlook

In Chapter 4, it was briefly suggested in the concluding remarks that an alternative application of the high-throughput methodology is to optimize the GFA of existing BMG alloys by investigating glass formation in their compositional vicinity. While this can be easily accomplished for ternary alloys, fabricating composition libraries to identify GFA maxima within the composition space of higher order systems (i.e. quaternary, quinary, etc.) poses significant challenges. In order to produce libraries containing continuous regions of a given composition space, the number of independent variables within the alloy system cannot exceed the dimensionality of the library. For example, in the binary work, there was only one independent molar fraction X_i, either X_{Cu} or X_{Zr}, which enabled the exploration of a continuous composition

range across a single re-melted line in the graded specimens. In the ternary work, there were two independent constituents, matched by the 2-d libraries. Accordingly, a thorough survey of a quaternary system would require fabrication of a 3-d library. However, the current fabrication scheme for 2-d libraries is at best limited to exploring pseudo-ternary sections through 3-d quaternary space (Fig. 8.1).

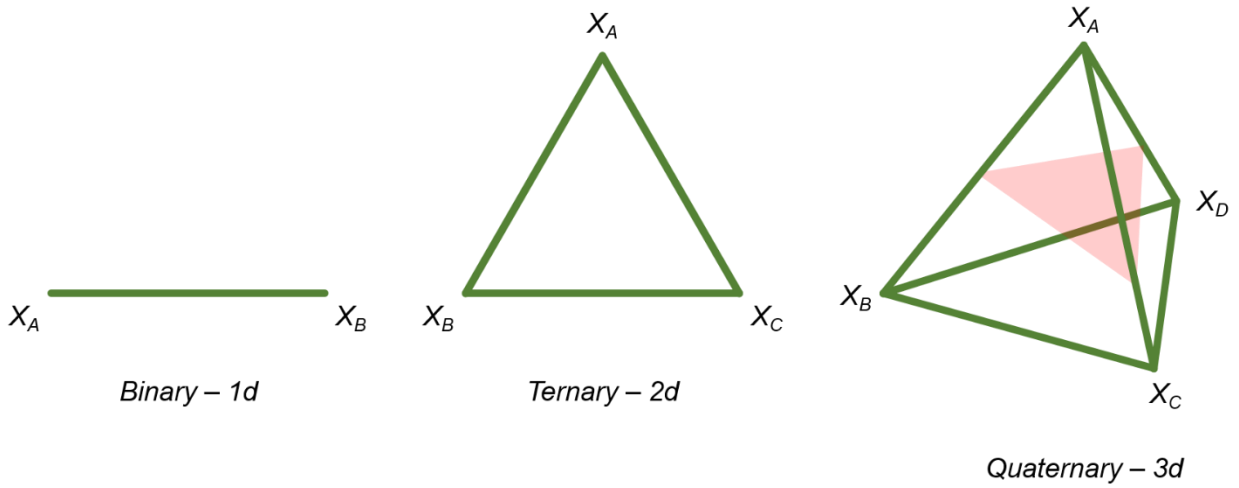

Figure 8.1 Representative diagrams of composition space for binary, ternary, and quaternary alloy systems. Beyond three elemental constituents, 2-d libraries are no longer suitable for thorough exploration of composition space.

Instead of fabricating "libraries", an alternate approach for optimizing GFA is to use laser deposition to implement an iterative search algorithm in the compositional neighborhood of an existing BMG. Each iteration in the algorithm would be informed by the results of the previous iteration. Figure 8.2 illustrates the thought process for an arbitrary ternary system but the concept is applicable for higher order systems as well. In the first iteration, a composition tie line is fabricated, varying in one of the components and passing through the composition of the known BMG; this can be accomplished by casting a substrate of the existing alloy that is slightly deficient in the component to be varied, followed by deposition of the varying component in a graded manner across the substrate. Applying the optimization sequence described in Chapter 3 yields

the optimum glass former in the tie line. In the second iteration, the procedure is repeated for a tie line varying in a different component and passing through the new composition identified in the first iteration; the search algorithm continues until the optimum glass former in the tie lines converges to a single composition of highest GFA in the system.

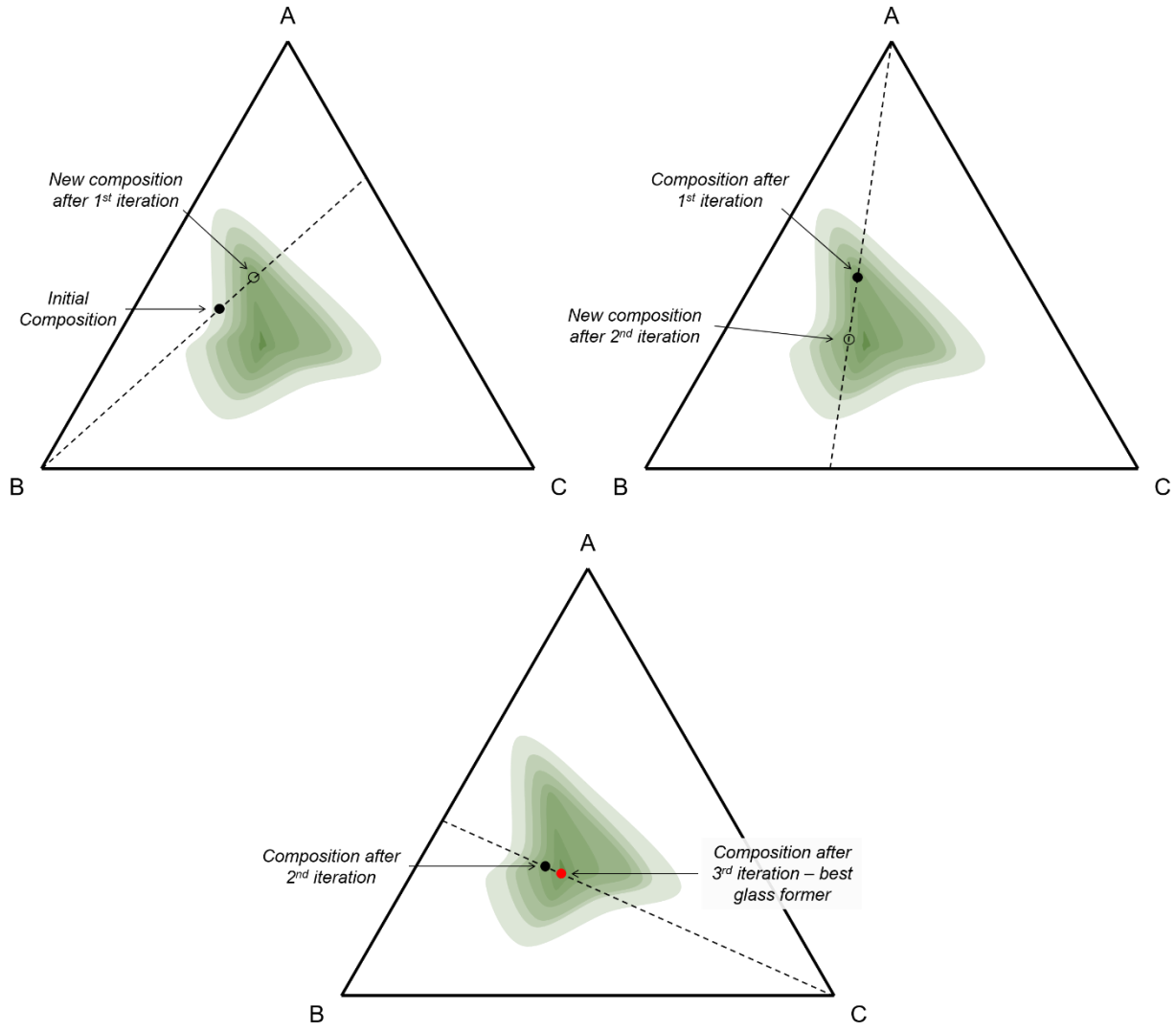

Figure 8.2 Schematic thought process of iterative search algorithm for locating the best glass former in multicomponent systems.

Although the high-throughput methodology was developed for the purpose of discovering new glass formers in multicomponent alloy systems, the experimental techniques in the methodology are not restricted to metallic glasses and may be adapted to explore other types of multicomponent alloys. For example, high entropy alloys (HEAs), an exciting new class of engineering materials that contain at least five principle elements[1–3], possibly occupy an even larger composition space than BMGs. Currently, phenomenological guidelines are available for designing single-phase microstructures of potential HEAs, but the qualitative rules lack quantitative specificity and are thus unable to guarantee a predicted outcome. In light of these challenges, the discovery process of HEAs can also benefit from a high-throughput experimental approach to alloy development and design.

8.3 References

1. Cantor, B. Multicomponent and High Entropy Alloys. *Entropy* **16,** 4749–4768 (2014).
2. Miracle, D. B. *et al.* Exploration and development of high entropy alloys for structural applications. *Entropy* **16,** 494–525 (2014).
3. Zhang, Y. *et al.* Microstructures and properties of high-entropy alloys. *Prog. Mater. Sci.* **61,** 1–93 (2014).

Appendix

The contents of this section are several functions and scripts written in Matlab® by the author of this dissertation that future students and researchers may find helpful, particularly with regards to the analysis and processing of raw experimental data.

`Cooling_Rate_Analysis(T_profile)` is a function that receives a 1-d temperature profile `T_profile` as input, and returns the average cooling rate between 1600 ˚C and 2200 ˚C.

```
function[avg_coolingrate] = Cooling_Rate_Analysis(T_profile)

T_gradient = zeros(101,1);

for i = 1:101
    if i == 1
        T_gradient(i) = (T_profile(i+1,2) - T_profile(i,2))/42.1;
    else if i == 101
            T_gradient(i) = (T_profile(i,2) - T_profile(i-1,2))/42.1;
        else
            T_gradient(i) = (T_profile(i+1,2) - T_profile(i-1,2))/84.2;
        end
    end
end

Cooling_Rate = T_gradient*16933.33;

min_pos = 1;
max_pos = 1;
i = 1;

while T_profile(i,2) < 1600
    min_pos = i;
    i = i+1;
end

i = 1;

while T_profile(i,2) < 2200
    max_pos = i;
    i = i+1;
end
```

`Cleanmap(map)` is a function that removes the artificial gradient introduced by undesirable drift effects from a modulus map. It receives a 256 x 256 data array as the input and returns the "cleaned up" modulus map, `new_map`.

```
function[new_map] = CleanMap(map)

avg_modulus = mean(Array_to_Vector(map));

avg_row = mean(map,2);

for i = 1:256
    for j = 1:256
        new_map(i,j) = (avg_modulus/avg_row(i))*map(i,j);
    end
end
end
```

Below is an example of a script that reads a collection of raw text files containing the *P*-*h* data of a nanoindentation experiment into a data cell array. Each cell contains a two-column matrix of the load and displacement values. The example below reads in 100 indentation text files.

```
Indentation_Cell = cell(1,100);

count = 1;

for i = 1:10
    filename = sprintf('Vit106a_3_0000%d LC.txt',i-1);
    Indentation_Cell_3{count} = dlmread(filename,'',6,0);
    count = count+1;
end

for i = 11:100
    filename = sprintf('Vit106a_3_000%d LC.txt',i-1);
    Indentation_Cell_3{count} = dlmread(filename,'',6,0);
    count = count+1;
end
```

`Work_Energy_Analysis(Data_Cell)` analyzes all the indentation data contained within a data cell array. It returns a 3-column matrix containing values for the total work of indentation (column 1), the stored elastic energy (column 2), and the ratio of the plastic work of indentation to the total work (column 3).

```
function[W_array] = Work_Energy_Analysis(Data_Cell)

W_array = zeros(length(Data_Cell),3);

for i = 1:length(Data_Cell)

    min_loc = 200;
    while Data_Cell{i}(min_loc,1) < 0
        min_loc = min_loc + 1;
    end

    cell_length = length(Data_Cell{i}(:,1));
    max_h = max(Data_Cell{i}(:,1));

    for j = 1:cell_length
        if Data_Cell{i}(j,1) == max_h
            max_loc = j;
        else
        end
    end

    W_array(i,1) =
trapz(Data_Cell{i}(min_loc:max_loc,1),Data_Cell{i}(min_loc:max_loc,2));
    W_array(i,2) =
abs(trapz(Data_Cell{i}(max_loc:cell_length,1),Data_Cell{i}(max_loc:cell_lengt
h,2)));
    W_array(i,3) = (W_array(i,1) - W_array(i,2))/W_array(i,1);

end
```